
Predictive Force Feedback in a Teleoperated Robotic Surgical System

*Using Force Modelling to Improve Teleoperation
Transparency and Stability*

TARAN BATTY

*A thesis presented for the degree of
Masters of Engineering Science (Research)*



Department of Mechanical and Aerospace Engineering

Monash University

November 2017

Copyright Notice

The author (2017).

I certify that I have made all reasonable efforts to secure copyright permissions for third-party content included in this thesis and have not knowingly added copyright content to my work without the owner's permission.

Declaration

This thesis contains no material which has been accepted for the award of any other degree or diploma at any university or equivalent institution and that, to the best of my knowledge and belief, this thesis contains no material previously published or written by another person, except where due reference is made in the text of the thesis.

Signature: _____

Print Name: _____

Date: _____

Acknowledgements

The research work presented in this thesis was conducted in the Robotics and Mechatronics Research Laboratory (RMRL), at the Department of Mechanical and Aerospace Engineering, Monash University.

First and foremost, I would like to express my sincere gratitude to my supervisor, Bijan Shirinzadeh, for facilitating this research in terms of equipment, expertise, advise, and direction. Also, particular thanks for going above and beyond in supporting me financially throughout this research program. Without your vast knowledge, experience, and support this research would never have been possible.

A special thank you to my friends and family for their support during this undertaking, with particular mention to my parents, for their unconditional support, and to my beautiful, intelligent, and above all else patient girlfriend Jamila, who has stayed with me for the entire meandering path that this research has taken.

I am also grateful for the hard-working individuals of the RMRL, who have offered guidance, and made this research an overall enjoyable experience.

Finally, I would like to thank the colleagues, support staff, and friends at Monash University.

Abstract

Teleoperated robotic systems for minimally invasive surgery offers significant improvements over traditional hand-held surgical techniques. Improved dexterity, active filtering of hand-tremors, retained hand-eye coordination, and motion scaling are all achievable with surgical robotics. However, current surgical robotic systems are yet to include an effective force feedback mechanism, which is often reported by surgeons and researchers as a major limitation of teleoperated robotic systems.

The difficulty in providing effective force feedback stems from the fact that teleoperator transparency and stability are conflicting qualities in traditional bilateral control architectures. Efforts to improve transparency inevitably lead to compromised stability. Similarly, increasing stability acts to dull system transparency. This is primarily due to the finite communication speed between the constituent slave and master subsystems.

In this research, the compromise between transparency and stability is alleviated by utilising an environment estimation - force prediction control methodology. Replacing the direct force feedback channel is an estimator – which recursively calculates estimations of the apparent environment parameters, and the force predictor – which uses the estimated parameters to create a virtual environment for the master to interact with.

Transparency was shown to significantly improve with the estimation - prediction controller. By utilising a virtual environment, the master feedback force is generated by the master's own kinematics, creating a much more natural feeling feedback response.

Further improvements were also made to the estimator with the inclusion of an estimation speed adaptor, which enables fast parameter convergence, while maintaining parameter stability against a changed environment.

Experimental results have demonstrated the potential improvements to teleoperator performance, with the estimation - prediction methodology presented simultaneously maintaining high levels of transparency and stability.

Contents

1	Introduction	1
1.1	Robotic Minimally Invasive Surgery	2
1.1.1	Advantages of RMIS	3
1.1.2	Current Surgical Robotic Systems	3
1.2	Haptic Feedback	5
1.2.1	Transparency and Stability	7
1.2.2	Predictive Control	8
1.3	Motivation	9
1.4	Thesis Scope and Overview	9
1.4.1	Environment Estimation and Predictive Force Feedback	10
1.4.2	Adaptive Environment Estimation	11
1.5	Contributions	12
1.6	Thesis Outline	14
2	Relevant Theory and Literature Review	15
2.1	Fundamental Research on Transparency and Stability	16
2.1.1	Transparency	16
2.1.2	Stability	18
2.1.3	Bilateral Teleoperator Controllers	20
2.2	Review of Current Bilateral Controller Performance	22
2.2.1	Transparency Optimised Controller Design	22
2.2.2	Stability Approaches	24
2.2.3	Adaptive Controllers	26
2.3	Summary	31
3	The Teleoperated Robotic Surgical System Research Platform	33
3.1	Surgical Slave Design	33
3.1.1	Parallelogram Design for a Remote Center of Motion	33
3.1.2	Force Sensing Surgical Tool	35
3.1.3	Sensors and Actuators	36
3.2	Haptic Master	38

3.3	Controller Design	39
3.3.1	Position Control	39
3.3.2	Force Feedback	42
3.4	Summary	43
4	Development of Predictive Force Feedback	45
4.1	The Estimation - Prediction Controller	45
4.1.1	Force Models	47
4.1.2	Estimating the Environment Parameters	49
4.1.3	Predicting Force Feedback	50
4.2	A Metric for Teleoperator Performance	51
4.2.1	Estimation Error	52
4.2.2	Prediction Error	52
4.2.3	Optimal Solution	54
4.3	Experimental Validation of the EWRLS Estimator	54
4.3.1	Experimental Set-up and Procedure	54
4.3.2	Experimental Results	57
4.4	Summary	63
5	Experimental Verification of Predictive Force Feedback	65
5.1	Human-in-the-Loop Teleoperation	65
5.1.1	Experimental Set-up and Procedure	66
5.1.2	Direct Force Feedback	67
5.1.3	Spring Based Adaptor	71
5.1.4	Kelvin-Voight Model	74
5.1.5	Hunt-Crossley Model	78
5.2	Summary	81
6	Estimator Adaptability	83
6.1	Development of an Adaptive Forgetting Factor	83
6.1.1	Parameter Estimation Behaviour with a Static Forgetting Factor	85
6.1.2	Development of an Adaptive Forgetting Factor	89
6.1.3	Environment Boundary Detection	93
6.2	Experimental Validation of the Adaptive Forgetting Factor	94
6.2.1	Experimental Set-up and Procedure	95
6.2.2	Experimental Results	97
6.3	Summary	110
7	Conclusions and Recommendations	112
7.1	Summary	112
7.1.1	Developed Estimation - Prediction Controller	112

7.1.2	Forgetting Factor Adaptor	113
7.2	Recommendations for Future Work	114
7.2.1	Experimental Platform	114
7.2.2	Future Research	116

List of Figures

1.1	Overview of a teleoperated master-slave network robot.	4
1.2	The da Vinci Robotic Surgical System	4
1.3	Phantom Omni haptic device	7
1.4	Developed bilateral controller	11
1.5	Developed bilateral controller, with the forgetting factor adaptor.	12
1.6	Expanded view of the forgetting factor adaptor.	12
2.1	Bilateral teleoperator circuit diagram	16
2.2	Bilateral teleoperator system block diagram with time delays.	20
2.3	Wave-variable controller	25
2.4	Slotine-Li adaptive controller	27
2.5	Smith predictor and Slotine-Li controller	28
2.6	Neural Network controller	28
2.7	Impact behaviour of the Kelvin-Voight force model	30
2.8	Impact behaviour of the Hunt-Crossley force model	30
2.9	2-stage estimation process for the Hunt-Crossley force model.	31
3.1	Surgical slave mechanism	34
3.2	Overcoat design of the surgical slave end-effector	36
3.3	Friction wheel assembly for the drive and measurement wheels on the linear stage.	37
3.4	Surgical slave mechanism position controller	40
3.5	System motion bandwidth, and 2 mm step response.	40
3.6	System motion bandwidth, and 2 mm step response.	42
3.7	Existing bilateral teleoperator controller	43
4.1	Environment estimation and force prediction control structure.	46
4.2	Impact behaviour of the Kelvin-Voight force model.	48
4.3	Developed estimation-prediction bilateral controller.	55
4.4	Surgical robot (slave) in contact with the polyurethane foam.	56
4.5	Frequency-dependant delay of a first-order Butterworth filter.	58

4.6	Estimated Kelvin-Voight environment parameters under velocity and force filtering.	59
4.7	Estimated Hunt-Crossley environment parameters under velocity and force filtering.	59
4.8	Estimated Kelvin-Voight environment parameters under position, velocity and force filtering.	60
4.9	Estimated Hunt-Crossley environment parameters under position, velocity and force filtering.	61
4.10	Comparison of estimated parameters to optimal parameters, across various filter combinations.	62
5.1	Full teleoperated system.	66
5.2	Direct force feedback force-indentation profile.	68
5.3	Direct force feedback position-time profiles.	69
5.4	Direct force feedback force-time profile.	71
5.5	Spring-based adaptor force-indentation profile.	72
5.6	Spring-based adaptor force-time profiles.	73
5.7	Spring-based adaptor position-time profiles.	74
5.8	Kelvin-Voight force model force-indentation profile.	75
5.9	Kelvin-Voight force model force-time profile.	76
5.10	Damping coefficient, master velocity, and damping term for the Kelvin-Voight force model.	77
5.11	Hunt-Crossley force model force-indentation profile.	79
5.12	Hunt-Crossley force model force-time profile.	81
5.13	Prediction RMSE for each of the force feedback methodologies tested	82
6.1	Estimated environment parameters across a range of forgetting factors.	86
6.2	Comparison of the estimation RMSE using various forgetting factors with the optimal solution RMSE.	89
6.3	Profile of the inverse tangent adaptor	91
6.4	The developed bilateral controller, including estimation-prediction controller and estimator adaptor.	92
6.5	The expanded forgetting factor adaptor.	93
6.6	Flowchart of the environment boundary detection process.	94
6.7	Side view of the simulated tissue sample.	95
6.8	Forgetting factor adaptor curve for $SF = 10$	96
6.9	Force-indentation profile of a polyurethane foam and simulated tissue environment, using the forgetting factor adaptor.	97
6.10	Propagation of estimation RMSE with the forgetting factor adaptor.	98

6.11	Moving window average of the environment estimation RMSE for the previous 1 s, using the forgetting factor adaptor.	99
6.12	Comparison between RMSE of optimal solution and estimated adaptive parameters.	100
6.13	Propagation of prediction RMSE with the forgetting factor adaptor. . . .	100
6.14	Estimated parameters for a polyurethane foam and simulated tissue environment, using the forgetting factor adaptor.	101
6.15	Evolution of the forgetting factor over the three experiments.	102
6.16	Force-indentation profile of a polyurethane foam and simulated tissue environment, using a static forgetting factor.	103
6.17	Propagation of estimation RMSE with a static forgetting factor.	104
6.18	Moving window average of the environment estimation RMSE for the previous 1 s, using a static forgetting factor.	104
6.19	Comparison between RMSE of optimal solution and estimated parameters.	105
6.20	Propagation of prediction RMSE with a static forgetting factor.	106
6.21	Estimated parameters for a polyurethane foam and simulated tissue environment, using a static forgetting factor.	107
6.22	Final 10 s of each estimated parameter for the adaptive and static forgetting factors.	109
7.1	Intuitive Surgical's <i>EndoWrist</i> [®] instruments [83].	115

List of Tables

2.1	Alternate forms of the Immittance matrices.	19
2.2	List of 2-channel bilateral teleoperator architectures, and their associated channels.	22
3.1	Joint space requirements and performance for the surgical slave mechanism	34
3.2	Cartesian space requirements and performance for the surgical slave mechanism.	35
3.3	Characteristics of the Nano25 force torque sensors. The Nano25 is the primary sensor used during experimentation.	37
3.4	Performance characteristics of the Phantom Omni haptic feedback device.	39
3.5	Position and velocity controller gains.	41
4.1	Linearized force models used in the EWRLS algorithm.	50
4.2	Initial values for the estimation algorithm.	56
4.3	Estimation RMSE of the EWRLS algorithm for various filter combinations.	62
4.4	RMSE the optimal solution to the measured data, for various filter combinations.	63
5.1	Initial values for the estimation algorithm.	67
5.2	RMSE and motion characteristics using direct force-feedback.	70
5.3	RMSE and motion characteristics using the spring-based adaptor.	73
5.4	Prediction, estimation, and optimal RMSE using the Kelvin-Voight force model.	77
5.5	Prediction, estimation, and optimal RMSE using the Hunt-Crossley force model.	80
6.1	Range of forgetting factors, and the relative speed of parameter estimation.	85
6.2	Initial and assigned values for the estimation algorithm.	96
6.3	Summary of the final estimation and prediction RMS errors for both the static and adaptive forgetting factor methodologies.	108

Chapter 1

Introduction

“To eliminate that which is superfluous, restore that which has been dislocated, separate that which has been united, join that which has been divided and repair the defects of nature.”

- Ambroise Paré, 16th century, on the role of surgery.

Surgery is a bloody affair. For much of antiquity, surgery was more akin to butchery than medicine. Trepanation, the earliest known surgical procedure [1], involved drilling or burring into the skull to expose the dura mater and relieve built-up pressure within. Seen as barbaric today, this procedure nevertheless marks the beginnings of the long and gory history of surgery.

Early civilizations revered sickness and subsequent medicine as supernatural. The Sumerian believed that sickness was caused by demons possessing rule-breakers [2], while the Egyptians deified Imhotep due to his medical prowess [3]. Centuries later, over the course of the middle-ages, science began to slowly replace superstition, as human knowledge grew with recorded information and the development of finer tools and equipment. Detailed dissections and cataloguing of the internal organs began in the 16th century [4], and with it came the rudimentary knowledge of how the internal organs behaved. Still, most medical procedures were extremely painful and ineffective.

It was not until the 18th century that empirical and experimental methodologies became widespread in the medical field. Scottish surgeon John Hunter, regarded as the

“father of modern surgery”, was said to have constructed surgical knowledge himself from scratch, foregoing past testimony and beliefs in an attempt to uncover truth [5].

With the 19th century came anaesthetic, the proverbial invention of the wheel for the surgical profession. The ability to sedate and relax patients meant that surgery could be longer, more complex, and more effective. Soon after came antiseptics and the practice of sterilising environments, which combated the significant risk of infection during surgery [3].

Diagnostic and imaging tools developed in the 20th century, such as X-Rays, CT scans, and ultrasound, meant that surgeries became more targeted and effective, as the physician was equipped with detailed information about an illness prior to operation. Today, modern surgery is revered as the pinnacle of scientific, medical, and engineering practices. We now explore the current advancements that are taking place within the surgical field; namely, robotic surgery.

The first section of this chapter delves into Minimally Invasive Surgery (MIS), and Robotic Minimally Invasive Surgery (RMIS). The next two sections cover the concept of haptic-feedback, its relation to RMIS, and the difficulties in obtaining effective (transparent and stable) haptic-feedback for surgical applications. From there, the motivation and aims for this research are presented. Finally, the remaining chapters of this thesis are described.

1.1 Robotic Minimally Invasive Surgery

Since the mid-1980’s Minimally Invasive Surgery (MIS), also known as Laparoscopic surgery, has slowly grown to become the “gold standard” technique utilised by medical professionals [6]. This branch of surgical procedures uses long, slender tools and millimetre-scaled incisions to operate on patients with minimal disturbance to the surrounding internal tissues. Compared to traditional surgery, where large and brutal incisions expose huge sections of the internal organs, MIS touts a reduction in unnecessary

trauma, lower blood loss, and shorter hospital stays [7, 8, 9]. Robotic Minimally Invasive Surgery (RMIS) uses the same methodology as traditional MIS, but replaces the hand-held instruments with robotic manipulators.

1.1.1 Advantages of RMIS

Robotic Minimally Invasive Surgery (RMIS) takes the above advantages of MIS and improves upon them, as well as overcoming some of the shortcomings [10]. With robotic surgical instruments, surgeons are equipped with greater levels of control, precision, and dexterity [11, 12]. Unwanted bumps or tremors in the surgeon's hands can be actively filtered out of the surgical tool's movements, motion scaling can achieve micrometre-scaled levels of precision, and high degree-of-freedom end-effectors are able to manipulate tissue dexterously [13, 14]. Additionally, hand-eye co-ordination can be realigned to a more natural state due to the relative hand and tool reference frames being defined within the system's control architecture. In traditional MIS the necessary use of an endoscope, and the fulcrum effect of the surgical tools, means that often the surgeons hand movements often do not correspond intuitively to the end-effector's movement [13]. With RMIS systems, this is no longer an issue.

For these reasons robot-assisted approaches have become the optimal technique for several procedures. For example, the majority of radical prostatectomies performed in the United States are done robotically [15].

1.1.2 Current Surgical Robotic Systems

RMIS systems are typically designed as master-slave systems, where the slave (robot) is controlled by a master (input) device. The overall structure of a master-slave-network is shown in Figure 1.1. The master can be a simple computer interface that takes basic position input commands to a full-fledged multi-degree-of-freedom interactive actuator. The surgeon (or operator) interacts with the master, which leads to corresponding movements at the slave robot. Known as teleoperation, or telerobotics, this type of system enables the operator to remotely manipulate harmful or displaced environments. The

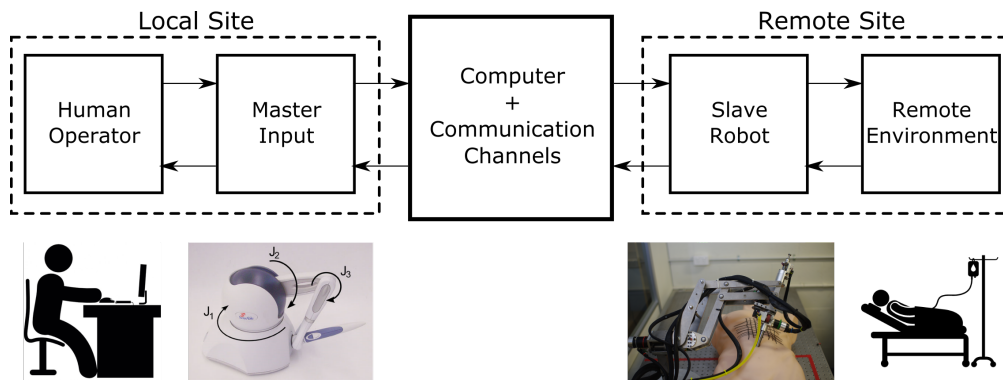


Figure 1.1: Overview of a teleoperated master-slave network robot.

master-slave system can also be expanded with autonomy, whereby the slave is able to act on its own accord to varying degrees.



Figure 1.2: The da Vinci Robotic Surgical System, showing surgeon console (master), and robotic (slave) mechanism [16].

Commercially, the dominant robotic surgical system is the da Vinci surgical system, shown in Figure 1.2. Developed by Intuitive Surgical, it was granted FDA approval in the year 2000 for general laparoscopic procedures, and has since been used in over 3 million MIS procedures worldwide [17]. The da Vinci is a teleoperated robot comprised of four robotic arms (holding two to three surgical tools and one endoscope) controlled by a surgeon sitting in an ergonomic console. The da Vinci system offers greatly increased control over the surgical equipment when compared to traditional hand-held MIS procedures.

For example, a study comparing spleen-preserving pancreatectomy – a procedure which requires extensive training, surgeon skill, and dexterity – found that the robot-assisted procedure was significantly superior to conventional laparoscopy at spleen-preservation fail/pass rates (1/19 vs 9/16, $p = 0.027$) [18].

The Senhance Surgical Robotic System is another, more recent, commercially available RMIS system. Developed by TransEnterix Surgical Inc, and granted FDA approval in the year 2017, the Senhance system is similar to the da Vinci system in that a surgeon, seated at an ergonomic cockpit, can control four independent robotic arms. Additional features include eye-tracking cameras that control endoscope view panning and zooming [19], as well as haptic feedback capabilities. Presently, the literature is light on the specific performance or technique used to generate this haptic feedback, possibly due to the relatively young age and minimal market share of the system. A small delay between surgeon action and feedback was explicitly mentioned in [20], which may indicate poor transparency.

A South Korean MFDS (equivalent to the FDA in the United States) approved system called the REVO-I Robotic Surgical System is also commercially available in South Korea for general endoscopic surgery. Like the Senhance system, the REVO-I incorporates haptic feedback, although clinical trials are yet to reach the stage where conclusions can be drawn about the features effectiveness [21].

1.2 Haptic Feedback

The very nature of RMIS means that the surgeon is separated from the patient's internal organs both visually and kinaesthetically. Visual feedback is provided via an endoscope, which re-establishes the surgeon's line of sight to the internal organs. There has been much commercial research in producing endoscopes with greater levels of manoeuvrability (e.g controllable distal tips, smart-memory-alloys, etc.) [22, 23, 24], visual acuity (e.g high-definition and 3D imagery) [25, 26], and functionality (e.g incorporating suction and ablation devices) [27]. Kinaesthetically, however, the surgeon is still removed from the internal organs, as the surgical tools are not mechanically connected to the

surgeon. This kinaesthetic separation is one of the main disadvantages of RMIS compared to conventional MIS [28, 29], as many surgical procedures are grounded in the sense of touch, and contributes to the technique's steep learning curve, and surgical complications.

Broadly speaking, teleoperation systems which provide force feedback are known as bilateral teleoperated systems. Bilateral refers to the exchange of position, velocity, and/or force information between a slave and master subsystem. For RMIS, the slave system is the robotic manipulator, and the master is the console controlled by the surgeon or operator.

The act of providing force feedback – also known as haptic feedback – can be separated into two main types: tactile and kinaesthetic. Tactile feedback includes information such as object shape and texture, and is likened to what is felt by your fingers. Kinaesthetic feedback includes point force information, described as what is felt in your muscles and tendons. Presently, tactile feedback requires large interfaces, are less robust, and more complex than kinaesthetic feedback. Due to the space limitations and nature of RMIS surgery, tactile sensing is rarely used, although it is well suited to providing the information necessary for procedures such as palpation and tumour location [30]. Kinaesthetic feedback yields only point force information such as the reactive force present when the robotic apparatus is pushed into a soft biological tissue. This type of force information is sufficient for knot tying, blunt dissection, and needle insertion procedures [31]. Like tactile feedback, it can also be used for palpation exercises, but does not give the same level of detail as tactile feedback. This research focuses on kinaesthetic force feedback. While not strictly accurate, the terms *haptic feedback* and *force feedback* henceforth refer to kinaesthetic feedback.

Providing haptic feedback can be achieved in several ways. The most common method is to use a haptic feedback device, or haptic pen. A haptic pen is typically a movable component or stylus linked to a base unit via actuated limbs, and directly controlled by the operator. Figure 1.3 shows a SensAble Phantom Omni haptic device (now branded as the Geomagic Touch), capable of exerting 3D force feedback. Forces are



Figure 1.3: The Phantom Omni haptic pen. The user experiences a feedback force via the motorised joints.

simulated by actuating the linkages to produce the necessary feedback forces at the stylus. In this way, the operator can feel and respond to the feedback force directly. Alternatively, force feedback information can be expressed visually, such as with a graphical display, or audibly, with a tone or noise indicating various force feedback conditions. Audible feedback is not ideal for surgical procedures, due to the already noisy environment of the operating theatre [31]. Research has shown that a combination of direct force feedback and visual feedback is most useful during RMIS [31]. Visual (or graphical) feedback tends to benefit novice surgeons more, with diminishing benefits among experienced surgeons [32].

1.2.1 Transparency and Stability

The effectiveness of a bilateral teleoperator in providing haptic feedback is measured by the system's transparency and stability. Transparency is defined as the level to which the master (haptic) device faithfully recreates the forces experienced at the slave (robot), and in the case of RMIS, is required to be maximised. Stability is concerned with the bounded behaviour of the master-slave system given the expected inputs. Again, stability is required to be maximised for RMIS applications.

Traditional bilateral controller designs are restricted by an emergent property of the connected master-slave system, where it has been shown that transparency and stability

are inherently conflicting qualities. The issue arises from the communication time-delays present between the two systems [33]. Efforts to improve stability ultimately mute the transparency, while transparency-maximised bilateral controllers suffer from a narrow stability range. The conflicting relationship between transparency and stability is explored in-depth in Chapter 2.

In a typical bilateral controller, force and position are exchanged *directly* or *quasi-directly* between slave and master systems. That is, the measured environment force is fed directly back from the slave to the master, and the haptic position is fed directly forward from the master to the slave, with no (direct) or minimal (quasi-direct) alteration to the signal values (excluding position and force scaling). The unavoidable communication time-delays between the two systems mean that feedback force and feed-forward position reach their destination system *a priori*, or after the fact. This delay is the root cause of the transparency/stability trade-off. As each system is reacting slightly too late, instabilities can grow within the feedback/feed-forward system. Moderating these instabilities results in compromised transparency, while leaving them can lead to unstable behaviour.

1.2.2 Predictive Control

The mutually exclusive relationship between transparency and stability in a typical bilateral controller necessitates an alternative approach to the controller's design. A promising alternative is to instead build an estimate of how the environment will react, given a set of kinematics (position, velocity, and acceleration). This estimated behaviour can then be used locally by the master to drive the force feedback dynamics. This estimation-prediction mechanism severs the direct force link between slave and master, meaning that communication delays are no longer of considerable effect; the master is now reacting to *its own kinematics*. Provided the behaviour of the local estimated environment closely matches the behaviour of the actual environment, then both transparency and stability can be simultaneously improved.

1.3 Motivation

Current commercial surgical robotic systems are yet to provide any haptic feedback to the operator. Presently, force information is derived visually through the observation of tissue deformation during manipulation, which requires proper training and lengthy experience to be an effective method. It has been shown that providing force feedback can improve completion time [34] and the number of errors [35] in simulation exercises. Additionally, force feedback can be used to implement a “virtual fixture”, where a specified path can be generated to guide a surgeon to the desired location with minimal disturbances on sensitive internal tissues [36].

Implementing haptic feedback in a surgical robotic system must meet very stringent performance criteria. To be a useful addition to the surgeon’s toolbox, transparency must be maximised to ensure the surgeon receives any and all relevant force information. Similarly, system stability needs to be guaranteed. The conflicting nature of these two qualities in general bilateral teleoperators means that *traditional* bilateral controllers are ill-suited to this task. Instead, an alternative avenue for force feedback is required.

1.4 Thesis Scope and Overview

This thesis concentrates on the development, implementation, and experimental validation of an environment estimation and predictive force feedback methodology into an existing RMIS research system. The experimental facility is first outlined, where key design and performance characteristics of the slave mechanism are identified. An *estimation-prediction* methodology is then proposed, where the slave-environment force is first estimated, then used to predict the haptic-operator force. This methodology creates a virtual environment with which the haptic master interacts. Experimental results give evidence that using a virtual environment can improve transparency significantly when compared to traditional force feedback methodologies. Further improvements on the estimation-prediction methodology are then presented, with particular emphasis on estimator adaptability.

1.4.1 Environment Estimation and Predictive Force Feedback

The developed environment estimation process uses an Exponentially Weighted Recursive Least Squares (EWRLS) algorithm to continuously estimate on-line the environment parameters of a given force model, based on the slave position, velocity, and force.

The force models utilised are the Kelvin-Voight and Hunt-Crossley force models, defined by (1.1) and (1.2), respectively. Both force models are often used to model contact with soft environments. The Hunt-Crossley model in particular was developed to model biological soft tissues, as it is able to capture the non-linear effects of biological tissues.

$$F = K_{KV}x_s + B_{KV}\dot{x}_s \quad (1.1)$$

$$F = K_{HC}x_s^n + B_{HC}x_s^n\dot{x}_s. \quad (1.2)$$

With the estimated parameters, a simulated virtual environment can be created and interacted with by the haptic master. By severing the direct force channel between the measured slave and the haptic feedback force, issues regarding time-delay can be minimised. Interacting with a virtual environment means that the haptic master is receiving force feedback appropriate to its own kinematics. Provided that the virtual environment represents the measured environment well, then both teleoperation transparency and stability can potentially be maximised. The developed estimation-prediction controller is presented in Figure 1.4.

The detailed development of the EWRLS estimator and force prediction methodology is presented in Chapter 4, along with the experimental verification of the slave-side estimation process. Chapter 5 extends the experimental verification to the combined master-slave teleoperated system with human-in-the-loop palpation experiments.

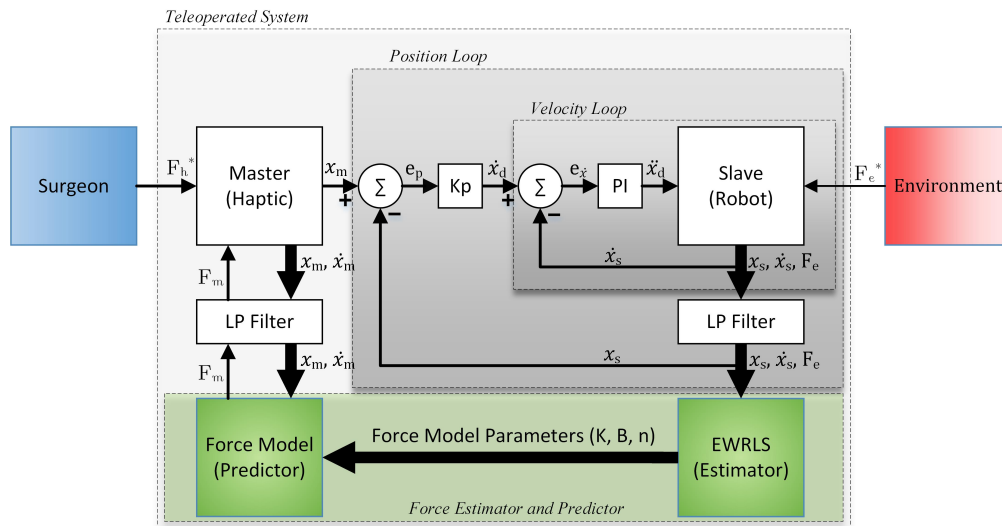


Figure 1.4: Developed bilateral controller, utilising the estimation - prediction force feedback methodology, highlighted in green.

1.4.2 Adaptive Environment Estimation

Further developments to the estimation-prediction controller are conducted in Chapter 6, where estimator adaptability is investigated. Included in the EWRLS algorithm is the *forgetting factor*, labelled as λ ; a parameter that dictates the sensitivity of the estimator to new information. The forgetting factor influences the estimator speed by assigning more relative weight to newer measurements, enabling the estimator to adapt quickly when exposed to sudden changes in the inflow of information. A value of $\lambda = 1$ results in the standard Recursive Least Squares algorithm, where all prior information is weighted equally. Setting $\lambda < 1$ results in faster estimation, as newer information is weighted higher during parameter estimation, but can lead to parameter instability.

Ideally, the estimator would increase the speed of estimation by decreasing λ when the estimated parameters are inaccurate, then increase λ to ensure parameter stability once the estimated parameters become more accurate. The accuracy of the estimated parameters is defined via the *estimation error*, the error between the *measured* environment force and the *estimated* force derived from the estimated parameters and the slave kinematics.

Chapter 6 details the development of an adaptor into the EWRLS algorithm, where λ is varied based on the estimation error. The *arctangent* function is used to provide

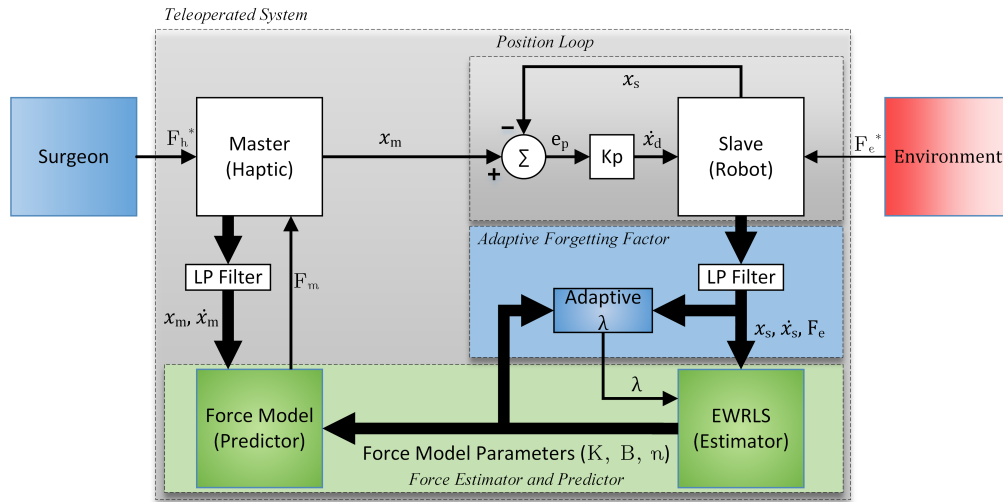


Figure 1.5: Developed bilateral controller, with the forgetting factor adaptor highlighted in blue.

a smooth transition between an upper (slower) and lower (faster) values of λ . The developed controller, including the adaptor, is presented in Figure 1.5. The expanded adaptor block is presented in Figure 1.6.

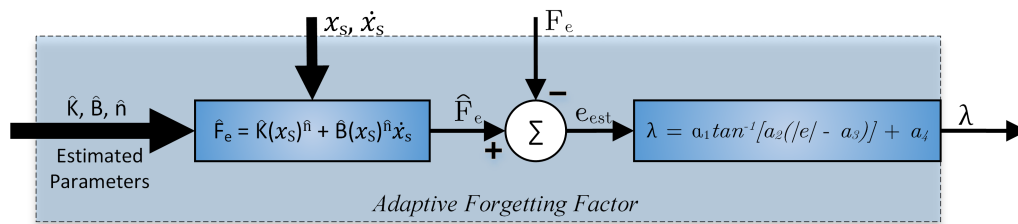


Figure 1.6: Expanded view of the forgetting factor adaptor.

Experimental validation is presented for the forgetting factor adaptor, which demonstrates the swift-then-stabilising behaviour of the estimator.

1.5 Contributions

This thesis aims to provide a method with which to counteract the intrinsic time-delays present in bilateral teleoperator controllers. Specifically, this thesis investigates the use of environment estimation and force prediction as a means to provide improved teleoperator transparency while maintaining stability in a robotic surgical system. The ability

to simultaneously provide high levels of transparency and stability is an important step in the implementation of realistic and robust haptic feedback into teleoperated robotics.

Prior research on this problem has used the Hunt-Crossley force equation as a basis in the modelling of soft-contact environments, due to the non-linear model mimicking the typical non-linear force behaviour observed in biological soft-tissues. With the log-linearisation process described in [37], the Hunt-Crossley force parameters can be estimated on-line using robust linear estimation techniques, such as the recursive least squares algorithms. In [38], an exponentially weighted recursive least squares (EWRLS) algorithm, using the linearised Hunt-Crossley model, was able to estimate and converge the parameters while in contact with a variety of soft environments, with the robot being driven by a sinusoidal trajectory.

This thesis primarily adds to the previous study of [38] by investigating transparency and force-prediction during human-in-the-loop teleoperation. The main contributions are:

- The development and implementation of an environment estimation - force prediction controller into a specifically designed haptic-enabled robotic surgical system. The controller achieves haptic feedback by using the estimated environment parameters as a virtual environment, with which the haptic device interacts.
- The identification of the sensitivity of the EWRLS algorithm to inconsistent phase distortions between each of the signal inputs, caused by filtering certain signals (e.g. force and velocity) and not others (e.g. position). This sensitivity can manifest as unacceptable or unrealistic estimated parameters (e.g. a negative damping coefficient).
- Demonstrating through experimental validation that transparent human-in-the-loop teleoperation can be achieved with the environment estimation - force predictive controller.
- The extension of the EWRLS estimator to include adaptive estimation, where the speed of estimation is varied based on the accuracy of the estimated parameters.

The adaptive estimator was shown to facilitate both fast adjustment to a new environment, as well as the stabilisation of the converged parameters.

1.6 Thesis Outline

In Chapter 2, a literature review of current bilateral teleoperator controllers is presented. Additionally, background theory relating to teleoperation transparency and stability is presented, where the performance gap between transparency and stability in traditional bilateral controllers is identified.

Chapter 3 presents the specific teleoperated robotic surgical system platform used during this research. Design features unique to the robotic surgical system are presented, along with the teleoperated system's performance characteristics.

In Chapter 4 the developed estimation-prediction force feedback controller is presented. Parameter estimation is experimentally verified with the surgical slave palpating a polyurethane foam, driven by a sinusoid motion input.

Chapter 5 expands the experimental validation to include both the environment estimation and force prediction processes. Teleoperator performance is evaluated with human-in-the-loop teleoperation tasks.

In Chapter 6, the estimator is improved with the inclusion of a forgetting factor adaptor; where the estimation speed is varied based on the accuracy of the estimated parameters. Experimental validation is conducted for the teleoperator performance when transitioning between two environments; a polyurethane foam to a simulated tissue sample.

Finally, Chapter 7 summarizes the presented work, and includes recommendations for future work.

Chapter 2

Relevant Theory and Literature

Review

Haptic feedback is not a new concept. There has been considerable research effort invested in the development of haptic feedback systems, including for robotic surgical systems. Recently, however, research has faulted, as typical controller designs inevitably run into a systemic limitation of teleoperator performance; the seemingly intrinsic trade-off between system transparency and stability.

Inherent communication time-delays between the slave and master systems means that high transparency results in poor stability. Conversely, efforts to stabilise the system are met with dulled transparency. This is the tragedy of developing force feedback – non-ideal performance in the individual systems result in significant issues when the systems are connected via the feedback/feedforward paths. Similar to a microphone placed directly in front of a speaker, small disturbances can grow into shrieking feedback.

2.1 Fundamental Research on Transparency and Stability

In his 1993 article [33], D.A. Lawrence formalised the relationship between teleoperator stability and transparency. This formalisation revealed that, due to system time-delays, stability and transparency are conflicting qualities. “*Passivity-based architectures and transparency-based approaches ... lie at opposite ends of this optimal stability/performance spectrum.*”

Since then, much research has been done on modifying and refining the controller architectures to achieve specific transparency or stability performance goals.

2.1.1 Transparency

Figure 2.1 represents a bilateral teleoperated system as a linear time invariant (LTI) master-slave two-port network (MSN). This representation relates the flow variables (velocity and current) to effort variables (force and voltage) [39].

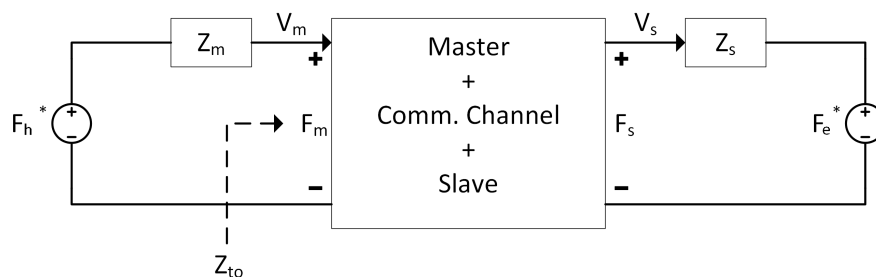


Figure 2.1: Circuit diagram representation of a bilateral teleoperation system.

In Figure 2.1, F_h^* and F_e^* are, respectively, the operator’s and environment’s exogenous input force. F_m and F_s are the master feedback and the measured slave force, respectively. Z_m and Z_s are impedances representing the dynamics of the operator’s hand and remote environment, respectively. V_m is the master velocity, and V_s is the slave velocity. Z_{to} is the impedance perceived by the operator. Impedance, Z , encompasses physical mass, damping, and stiffness properties, and each quantity is the Laplace transform of their respective variable. It is generally assumed that the operator

and environment are passive (and thus stable), as they do not act in such a way as to produce or inject additional energy into the system [40]. Thus, $F_h^* = 0$ and $F_e^* = 0$.

The LTI dynamics of the above system are:

$$F_m = F_h^* - Z_h V_h \quad (2.1a)$$

$$F_s = F_e^* + Z_e V_e. \quad (2.1b)$$

The impedance experienced by the operator is defined as:

$$Z_{to} = \left. \frac{F_m}{V_m} \right|_{F_e^*=0}. \quad (2.2)$$

Lawrence [33] defines the transparency condition as:

$$Z_{to} = Z_s. \quad (2.3)$$

Equation (2.3) translates to the operator (Z_{to}) experiencing the same environmental behaviour as the slave (Z_s).

This approach is known as *impedance matching*, and is a consequence of the sought after *kinematic correspondence* (2.4a) and *force reflection* (2.4b) between the master and the slave:

$$V_s = V_m \quad (2.4a)$$

$$F_m = F_s. \quad (2.4b)$$

With these definitions, a *hybrid* matrix can be developed as shown below:

$$\begin{bmatrix} F_m \\ -V_s \end{bmatrix} = \begin{bmatrix} h_{11} & h_{12} \\ h_{21} & h_{22} \end{bmatrix} \begin{bmatrix} V_m \\ F_s \end{bmatrix} \quad (2.5)$$

Using the kinematic and force correspondence conditions in (2.4a) and (2.4b), and the hybrid matrix of (2.5), *ideal* transparency is defined as (with no force or position

scaling):

$$H_{ideal} = \begin{bmatrix} 0 & 1 \\ -1 & 0 \end{bmatrix} \quad (2.6)$$

Performance is evaluated through examination of Z_{to} (2.3). For ease of calculation, the minimum impedance (i.e during free motion, $Z_s = 0$) and impedance width (i.e when the slave is clamped, $Z_s \rightarrow \infty$) are considered:

$$Z_{to,min} := Z_{to}|_{Z_s=0} = h_{11} \quad (2.7a)$$

$$Z_{to,width} := Z_{to}|_{Z_s \rightarrow \infty} - Z_{to,min} = \frac{-h_{12}h_{21}}{h_{22}} \quad (2.7b)$$

Ideal performance is considered as when $|Z_{to,min}| \rightarrow 0$ and $|Z_{to,width}| \rightarrow \infty$.

2.1.2 Stability

Stability for a bilateral teleoperator is usually presented in terms of passivity. Llewellyn's absolute stability criteria [41] is invoked in terms of a two-port network [42, 43], as a necessary and sufficient condition for absolute stability.

Llewellyn's absolute stability condition is expressed in terms of a master-slave network (MSN) *immittance* matrices $Y = \mathbf{P}u$ where Y is the output, u is the input, and \mathbf{P} is the immittance matrix. The hybrid matrix (2.5) is considered to be an immittance matrix. Similarly, the impedance matrix \mathbf{Z} , admittance matrix \mathbf{Y} , and inverse hybrid matrix \mathbf{G} are also classed as immittance matrices. These alternative matrices are defined in Table 2.1. The stability criteria detailed below is true for any immittance matrix, and it is useful to convert between the four immittance matrix forms to ease the stability analysis.

Table 2.1: Alternate forms of the Immittance matrices.

		Output (Y)	Immittance Matrix (P)	Input (u)
Hybrid	(H)	$\begin{bmatrix} F_m \\ -V_s \end{bmatrix}$	$\begin{bmatrix} h_{11} & h_{12} \\ h_{21} & h_{22} \end{bmatrix}$	$\begin{bmatrix} V_m \\ F_s \end{bmatrix}$
Impedance	(Z)	$\begin{bmatrix} F_m \\ F_s \end{bmatrix}$	$\begin{bmatrix} z_{11} & z_{12} \\ z_{21} & z_{22} \end{bmatrix}$	$\begin{bmatrix} V_m \\ -V_s \end{bmatrix}$
Admittance	(Y)	$\begin{bmatrix} V_m \\ -V_s \end{bmatrix}$	$\begin{bmatrix} y_{11} & y_{12} \\ y_{21} & y_{22} \end{bmatrix}$	$\begin{bmatrix} F_m \\ F_s \end{bmatrix}$
Inverse Hybrid	(G)	$\begin{bmatrix} V_m \\ F_s \end{bmatrix}$	$\begin{bmatrix} g_{11} & g_{12} \\ g_{21} & g_{22} \end{bmatrix}$	$\begin{bmatrix} F_m \\ -V_s \end{bmatrix}$

Llewellyn's criteria states that an LTI two-port network is absolutely stable if and only if [42]:

$$\Re\{p_{11}\} \geq 0 \quad (2.8a)$$

$$\Re\{p_{22}\} \geq 0 \quad (2.8b)$$

$$\eta(\omega) = \cos(\angle p_{12}p_{21}) + 2 \frac{\Re\{p_{11}\}\Re\{p_{22}\}}{|p_{12}p_{21}|} \geq 1 \quad (2.8c)$$

where p_{ij} , ($i, j = 1, 2$) are the elements of any of the immittance matrices. The first two conditions, that p_{11} and p_{22} are positive real, covers the passivity of the master and the slave when they are either free or clamped. The last condition (2.8c) incorporates coupling between the master and slave.

Although the passivity theorem has been used to analyse the stability of MSNs [44], the passivity condition for an MSN can be conservative. Alternatively, a structured singular value condition can guarantee stability [45, 46, 47]. This method was performed to a maximum singular value problem in [48].

2.1.3 Bilateral Teleoperator Controllers

With the transparency and stability tools above, controller design can be carried out and performance issues identified. Figure 2.2 shows the block diagram of a typical, 4-channel bilateral controller with modelled communication time delays. Here, 4-channel indicates that both velocity and force are feed-forward/backward signals, that is to say both velocity and force are exchanged between the slave and the master. 2-channel and 3-channel architectures are resolved by setting various feedback/forward paths to zero (C_1, C_2, C_3, C_4).

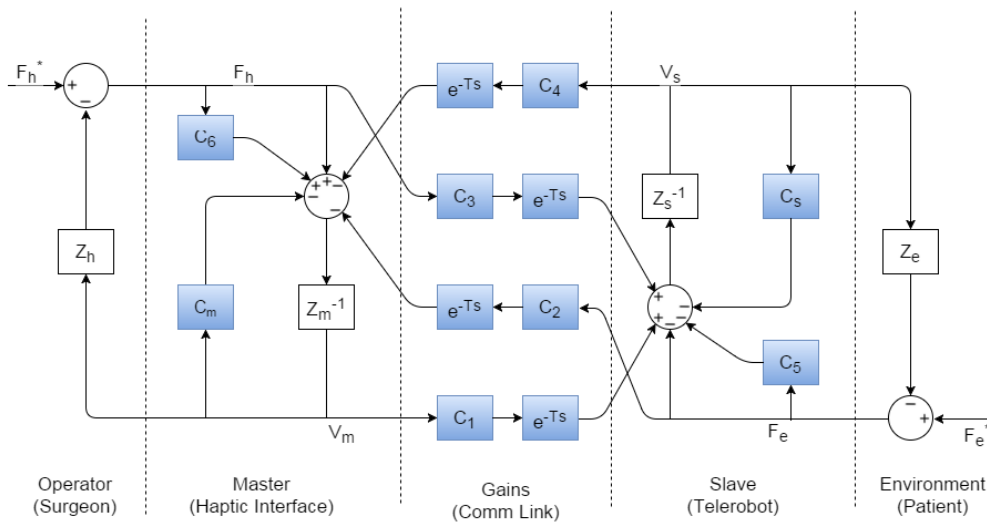


Figure 2.2: Bilateral teleoperator system block diagram with time delays.

The block diagram in Figure 2.2 was developed by Hashtrudi-Zaad and Salcudean in [44], extending the work done by Lawrence in [33] by including communications time delays (T) between slave and master, as well as adding local force feedback via C_5 and C_6 [49].

For this system (an Impedance-Impedance system), the closed loop dynamic equations are [44]:

$$Z_{cm}V_m + C_4e^{-Ts}V_s = (1 + C_6)F_m - C_2e^{-Ts}F_s \quad (2.9a)$$

$$C_1e^{-Ts}V_m - Z_{cs}V_s = C_3e^{-Ts}F_m + (1 + C_5)F_s \quad (2.9b)$$

where $Z_{cm} = Z_m + C_m$ and $Z_{cs} = Z_s + C_s$.

From here (2.9a), (2.9b), and (2.5) are used to obtain expressions for the h_{ij} parameters [44]:

$$h_{11} = \frac{Z_{cm}Z_{cs} + C_1C_4e^{-2Ts}}{(1 + C_6)Z_{cs} - C_3C_4e^{2Ts}} \quad (2.10a)$$

$$h_{12} = \frac{C_2Z_{cs}e^{-Ts} - C_4(1 + C_5)e^{-Ts}}{(1 + C_6)Z_{cs} - C_3C_4e^{2Ts}} \quad (2.10b)$$

$$h_{21} = \frac{C_3Z_{cm}e^{-Ts} + C_1(1 + C_6)e^{-Ts}}{(1 + C_6)Z_{cs} - C_3C_4e^{2Ts}} \quad (2.10c)$$

$$h_{22} = \frac{(1 + C_5)(1 + C_6) - C_2C_3e^{-2Ts}}{(1 + C_6)Z_{cs} - C_3C_4e^{2Ts}}. \quad (2.10d)$$

For a time-delay of T , the revised *ideal* hybrid matrix becomes (for $F_e^* = 0$ [50]):

$$H_{ideal,delayered} = \begin{bmatrix} 0 & e^{Ts} \\ -e^{-Ts} & 0 \end{bmatrix} \quad (2.11)$$

What we are left with is an expression for the ideal hybrid matrix when time-delays are included into the system analysis. If there are no time-delays (i.e $T = 0$) then the ideal matrix in (2.6) is resolved. As time delays grow, H_{12} and H_{21} respectively grow and shrink exponentially, resulting in a force and motion scaling between slave and master. Additionally, it should be noted that the above control architecture relies heavily on the precise knowledge of the master and slave dynamics (e.g Z_m and Z_s), which can, in practice, be difficult to obtain.

These expressions can be extended to evaluate the various alternate controller configurations (2-, 3-, 4-channel) for transparency and stability performance. 2-channel architectures are presented in Table 2.2.

“P” represents position (or velocity), and “F” represents force, with the nomenclature following a “feedforward-feedback” convention, as viewed by the master. A “P-F” architecture has force feedback (from the slave to the master) and position feedforward

(from master to slave). Also note that position and velocity can be used interchangeably without loss of generality.

Table 2.2: List of 2-channel bilateral teleoperator architectures, and their associated channels.

Control Structure	Removed Channels	No. Channels	Alternative Names
P-P	$C_2 = C_3 = 0$	2	Position Error Based
P-F	$C_3 = C_4 = 0$	2	Direct Force Feedback
F-F	$C_1 = C_4 = 0$	2	Shared Compliance
F-P	$C_1 = C_2 = 0$	2	N/A

2.2 Review of Current Bilateral Controller

Performance

The methodologies used to analyse the performance of a bilateral teleoperator was presented in the previous section, which drew from select but significant past research. A lot of the subsequent research and development of bilateral controller design has stemmed from the above methodologies.

2-channel architectures use a single feedforward and a single feedback channel connected between slave and master systems. They include position-position (P-P), position-force (P-F), force-position (F-P) and force-force (F-F) architectures. They are traditionally the most feasible teleoperators to design and implement, as they generally require fewer sensors. This is advantageous when size, cost, and ease of sterilisation are constraints, as is the case with robotic surgical systems. This literature review is centred on 2-channel architectures, as the pre-developed teleoperated system used in this study is a 2-channel architecture.

2.2.1 Transparency Optimised Controller Design

Transparency-optimised controllers are primarily aimed at providing ideal or near ideal transparency performance. Most transparency-optimised designs aim for *impedance*

matching between operator and environment impedances. Historically, it was thought that only *4-channel* architectures could achieve ideal transparency [33, 51]. With [50] came *3-channel* transparency optimised control laws, which made use of local feedback loops to compensate for operator and environment dynamics. These local feedback paths can be seen in Figure 2.2 and are labelled C_5 and C_6 for the operator and environment feedback paths respectively.

Transparency of 2-channel architectures has been explored extensively, with various techniques used to improve transparency and/or stability. A loop-shaping compensator and local feedback loops were employed in [52] to increase transparency and stability robustness in a position-force system. These improvements rely on accurate modelling of the slave and master dynamics, as well as consistent time-delays, which can be difficult in real world applications. Sliding-mode controllers were investigated in [53] for a pneumatic teleoperated system, and [54] with an FPGA. Restrictions in practical systems, where modelling errors, low-pass filters and hardware properties act to deteriorate transparency and stability robustness, are addressed in [55], although time-delay effects are not considered.

2-channel transparency optimised architectures were developed in [56] for a P-F and F-P architectures. The authors noted that transparency-optimised control laws could not be found for P-P or F-F types. The hybrid parameters for the P-F and F-P types were found to be:

$$H_{F-P,delayered} = \begin{bmatrix} 0 & e^{Ts} \\ -e^{-Ts} & 0 \end{bmatrix} \quad (2.12)$$

and

$$H_{P-F,delayered} = \begin{bmatrix} 0 & e^{-Ts} \\ -e^{-Ts} & 0 \end{bmatrix}. \quad (2.13)$$

The time-delayed transparency-optimized 2-channel architectures were found to offer greater transparency when compared to transparency-optimized 3- and 4-channel types. The authors of [56] noted that additional channels introduce “*impeding elements to transparency*”, such that increasing the number of channels adds non-zero terms to the

resolved hybrid matrix, which subsequently diminish transparency. However, their stability analysis revealed that the “*impeding elements*” contained within the additional channels were also responsible for improving stability, and that subsequently the 2-channel types exhibited poor stability.

2.2.2 Stability Approaches

Passivity-based stability approaches are the main mechanism employed in controller design to combat stability issues present in teleoperated systems. Their use extends from the fact that passivity is considered a sufficient condition for system stability [33, 39, 57]. Passivity relates system stability to input, output, and stored energy within the system. A system is said to be passive if (2.14) is true, which ensures that the input power (\mathbf{P}) is either dissipated (\mathbf{P}_{diss}) or stored $\left(\frac{dE}{dt}\right)$.

$$\mathbf{P} = \frac{dE}{dt} + \mathbf{P}_{\text{diss}} \quad (2.14)$$

This implies that the total energy supplied by the system up to time t is limited to the initial stored energy [58]:

$$E(t) - E(0) + \int_0^t P_{\text{diss}} d\tau \leq -E(0) = \text{constant}. \quad (2.15)$$

Power in this instance does not necessarily represent the physical quality but rather, for a teleoperator, represents flow and effort variables [58].

Passivity is applied to a time-delayed system by the scattering operator (2.16), which is derived from the hybrid matrix, and contains information on whether the passivity condition is met.

$$S(s) = \begin{bmatrix} 1 & 0 \\ 0 & -1 \end{bmatrix} (H(s) - I)(H(s) + I)^{-1} \quad (2.16)$$

The necessary and sufficient condition for passivity in a teleoperated system is that the norm of the scattering matrix $S(s)$ does not exceed unity [39]:

$$\|S(s)\| \leq 1. \quad (2.17)$$

From the passivity condition and the scattering operator, wave-variable control was developed in [58] to alleviate the negative effects of time-delay in a control system. Wave-variables are derived from pairs of standard power variables (\dot{x}, f) and represent right and left moving waves $(u_{l,r}, v_{l,r})$ through the master-slave systems, as per Figure 2.3. By using appropriate pairs of left and right moving waves (2.18), a non-passive time-delayed communication channel can be made passive [59].

$$u_l = \frac{1}{\sqrt{2b}}(F_l + b\dot{x}_l) \quad (2.18a)$$

$$u_r = \frac{1}{\sqrt{2b}}(F_r - b\dot{x}_r) \quad (2.18b)$$

$$v_l = \frac{1}{\sqrt{2b}}(F_l - b\dot{x}_l) \quad (2.18c)$$

$$v_r = \frac{1}{\sqrt{2b}}(F_r + b\dot{x}_r) \quad (2.18d)$$

The wave variables in (2.18) are tuned using the b parameter, which represents a characteristic impedance [58]. The basic structure of the wave-variable architecture is shown in Figure 2.3.

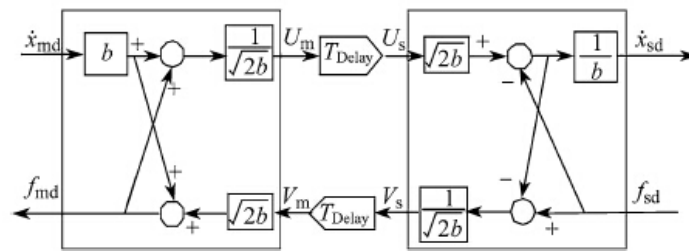


Figure 2.3: Flow of signals in a wave-variable teleoperation architecture [60].

Unknown but constant time-delays were investigated in [61], with a *virtual tool* used to account for implicit limitations imposed by the time-delay, resulting in predictable and reliable system operation.

Position drift in wave-variable controllers was addressed by *wave-integrals* in [62], where position and *integrated* force variables are used, as opposed to velocity and force. A similar approach was used in [63], but with only velocity integrated (to position).

While wave-variable based controllers do ensure stability, force-feedback is limited to only a few hertz for typical communication delays. An extension was presented in [64], which improved user perception with *wave-filtering*, where distracting oscillations were removed from useful reaction information.

2.2.3 Adaptive Controllers

The transparency-stability spectrum innate to bilateral teleoperation presents clear problems when applied to fields such as surgery, where any teleoperated system must provide a high level of transparency (to be a useful addition to the surgeon's tool-kit) and guarantee stability at all times. The fact that traditional bilateral controllers are fundamentally unable to provide high transparency *and* stability simultaneously is a clear roadblock to the pursuit of haptic feedback enabled robotic surgical systems.

As detailed in Section 2.2.1, the underlying reason for the transparency/stability trade-off is the time-delay between communicating information from the slave to the master, and vice-versa. By the time the slave-environment force reaches the master, it's essentially outdated information. Likewise, master-operator position is received by the slave after-the-fact, and any reaction that occurs at the master due to a perceived force (i.e contact with a stiff environment) is delayed. With traditional force-velocity signals running between the slave and the master, coherent kinaesthetic and dynamic operation is not possible.

It is for these reasons that *adaptive controllers*, *virtual environments*, or *environment estimation* have become a promising avenue of research in bilateral controllers. A survey of these methods can be found in [65].

per (2.19)), and *static* plant model (i.e slave and environment). Similarly, slave-master position tracking must be near-perfect.

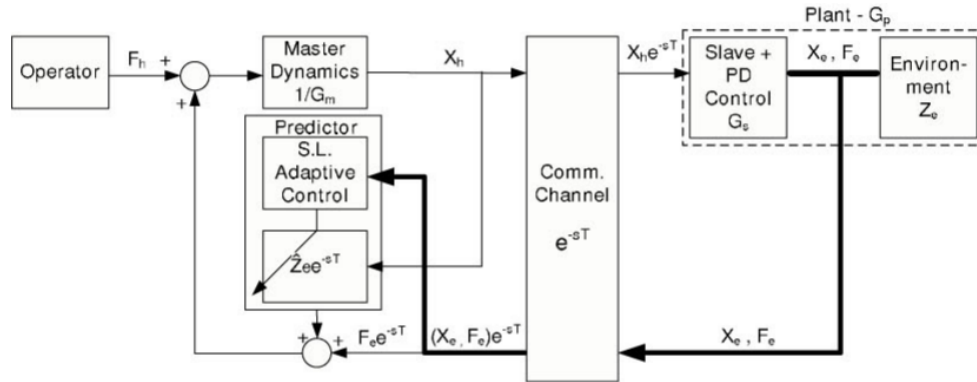


Figure 2.5: Block diagram of a Smith predictor and Slotine-Li adaptive controller developed in [71] for a force-position system. Block diagram was fully drafted in [72], based on work done in [71].

$$F_s = \begin{cases} K_e x_s(t) + B_e \dot{x}_s(t), & x_s(t) \geq 0 \\ 0 & x_s(t) < 0 \end{cases} \quad (2.19)$$

Non-linear dynamics were addressed in [73] and [74], where non-linear slave dynamics were accounted for via a neural network, shown in Figure 2.6. Similar incorporation of neural networks within the plant can also be seen in [72] and [75]. Neural network approaches are advantageous in that they do not require a predefined model. However, the increased flexibility means that convergence to realistic environment parameters can be slow, and performance is poor with time-variant environment dynamics.

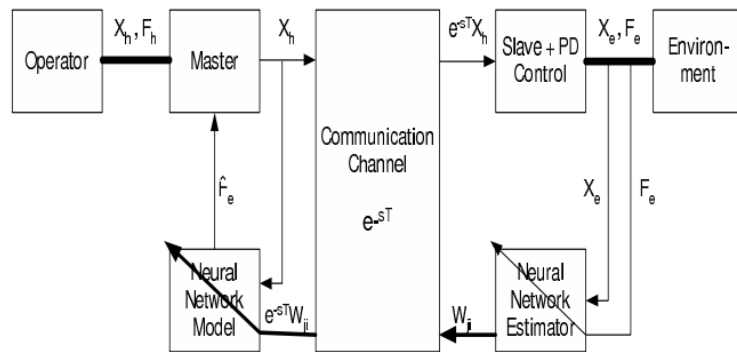


Figure 2.6: Block diagram of a Neural Network estimator and predictor in a 2-channel teleoperation control system

Virtual Environments

Purely *virtual environments*, while less applicable to teleoperated robotics, offer valuable insights into controller stability conditions and open a pathway to simulated training exercises, an area which is of great benefit to surgical robotics. Stability analysis for haptic feedback with a virtual environment can be found in [43], where stability of a developed virtual coupling between haptic device and virtual environment was guaranteed provided operator and (virtual) environment are passive. Time-delay between haptic and virtual systems was considered in [70].

Environment Estimation Controllers

Linear and static to near-static environment dynamics are the basis of many of the above approaches, primarily because linear and static dynamics are computationally simple. However, soft environments, particularly biological tissue, can be notoriously non-linear and non-static [76, 77], and the above approaches cannot be applied confidently to surgical telerobotics. The classic mass-damper-spring or damper-spring models do not accurately describe the class of environments that would be expected during surgery – i.e. non-linear soft tissue, with considerable energy exchange between tool and environment [78].

Figure 2.7 shows the inconsistencies of the linear Kelvin-Voight model when modelling soft-body impact. Figure 2.7 (a) outlines the hysteresis, and “shock” force at initial impact (point A) and the “sticking” feeling at load removal (point B). The power exchange is plotted in Figure 2.7 (b), where energy exchange between tool and body is inconsistent with physical intuition.

In 1975, K. Hunt and F. Crossley [79] developed a non-linear force model that more accurately describes soft-body impact when compared to previous models, such as the Kelvin-Voight model. The model, described in (2.20) and presented for environment modelling applications, has a non-linear position (x^n) dependence within the damping and stiffness terms. The behaviour of the damping term ($B_e \dot{x}(t)x^n(t)$) is of particular interest, as the position-dependence causes the term to drop to zero at the contact

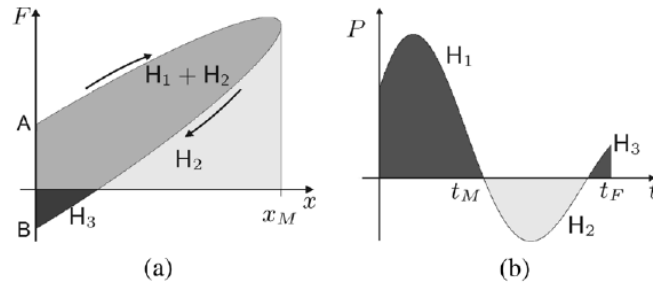


Figure 2.7: Typical behaviour of the Kelvin-Voigt model during soft-body impact. a) hysteresis loop during insertion and retraction, b) power exchange [77].

boundary, eliminating the "sticking" feeling present when retracting the tool from the contact environment. Figure 2.8 (a) shows the zero force at contact boundary ($x = 0$), and (b) shows consistent energy exchange between tool and environment.

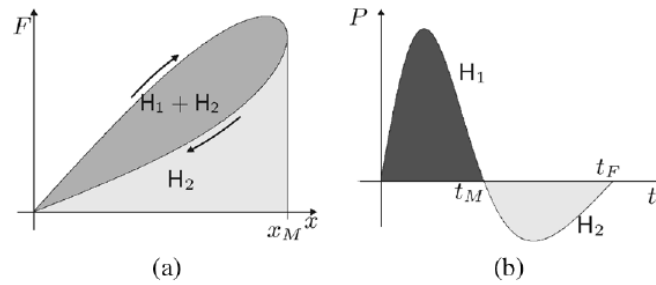


Figure 2.8: Behaviour of the Hunt-Crossley model during soft-body contact. a) Hysteresis loop during insertion and retraction, b) power exchange [77].

$$F_s = \begin{cases} K_e x_s^n(t) + B_e \dot{x}_s(t) x_s^n(t), & x(t) \geq 0 \\ 0 & x(t) < 0 \end{cases} \quad (2.20)$$

Being a non-linear equation, the Hunt-Crossley parameters (K_e , B_e , and n) are computationally difficult to estimate. A 2-stage online identification process was developed in [77], where estimation of the stiffness and damping parameters (K_e and B_e) is separated from the estimation of the non-linear term (n). The process is shown in Figure 2.9. The recurrent process Γ_1 uses an estimated \hat{n} to determine new estimations for \hat{K}_e and \hat{B}_e . Similarly Γ_2 uses estimated \hat{K}_e and \hat{B}_e to find an updated \hat{n} .

The 2-stage parameter identification method is sensitive to initial conditions [37] and demonstrates slow convergence. In [37] and [38], an alternative parameter identification

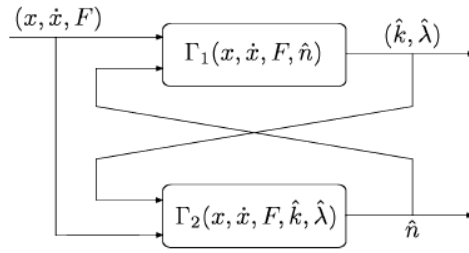


Figure 2.9: 2-stage estimation process for the Hunt-Crossley force model.

method was developed which uses a log-linearised approximation to the Hunt-Crossley equation:

$$\ln[F(t)] \cong \ln(K_e) + \frac{B_e}{K_e} \dot{x}(t) + n \ln[x(t)] + \frac{\epsilon}{K_e x^n(t)}. \quad (2.21)$$

In (2.21) the term ϵ is a measure of sensor and modelling error. The logarithm approximations confidently hold provided:

$$\left| \frac{B_e \dot{x}(t)}{K_e} \right| \ll 1 \quad (2.22a)$$

$$\left| \frac{\epsilon}{K_e x^n(t)} \right| \ll 1. \quad (2.22b)$$

The authors of [38] propose an approximate threshold of $\|\dot{x}\| < \frac{0.1K_e}{B_e}$ to satisfy (2.22a). Equation (2.22b) is assumed to be negligible, provided penetration $x(t)$ is large enough to satisfy the inequality. For times when the above inequality does not hold, it is suggested an alternative force feedback mechanism is required.

2.3 Summary

Current commercial RMIS systems do not provide force-feedback to the surgeon. The impeding element of haptic feedback in teleoperated robotic systems is the transparency-stability trade-off that plagues traditional bilateral controllers. The fact that these controllers cannot provide high levels of transparency *and* stability means that their application to robotic surgery is limited. The time-delay between the slave and master

systems means that direct position/force exchange is fundamentally flawed. Adaptive controllers, and more specifically environment estimation and prediction, have been suggested as a way to overcome this limit on performance. By decoupling the dynamics of the slave and master, communication time-delays are no longer the issue they were previously.

Modelling and predicting the dynamics of biological tissue is not without its challenges. Being non-linear in nature, biological soft tissues are difficult to estimate. The Hunt-Crossley force model, developed specifically to model contact with soft bodies, presents a promising avenue in environment estimation for surgical applications. The log-linearisation of the model means that computationally simple parameter estimation techniques (i.e the family of recursive least squares methods) can be used in environment parameter estimation.

Chapter 3

The Teleoperated Robotic Surgical System Research Platform

This chapter provides a brief overview of the design and performance characteristics of the robotic minimally invasive surgical system previously developed in [80]. The robotic surgical system serves as the research platform used during this research, and its capabilities and design characteristics have significant influence on the subsequent research undertaken. Firstly, a brief overview of the design is given, including the expected requirements for a robotic surgical system. This chapter then describes the initial bilateral controller implemented in the teleoperated robot, and its subsequent kinematic performance. This chapter is presented as a brief description of the capabilities of the robotic surgical system. A significantly more detailed overview of the robotic surgical system can be found in [80].

3.1 Surgical Slave Design

3.1.1 Parallelogram Design for a Remote Center of Motion

Robotic Minimally Invasive Surgery (RMIS) procedures rely on a constrained stationary point within the robot workspace to ensure that undue trauma to the patient is minimised. This stationary point, positioned coincident with the point of incision into the patient,

constricts the end-effector's motion to 4-DOF; three rotations (roll, pitch, and yaw) about the incision point, and one translation (along the tool axis) through the incision point. This stationary point can be achieved either within software or mechanically. A mechanical stationary point provides the simplest and most robust approach.

To this end, the surgical slave has a Parallelogram design (Figure 3.1), due to it being relatively planar and compact, having a natural extension over the patient, exhibiting high stiffness, and the relative simplicity of the inverse kinematics.

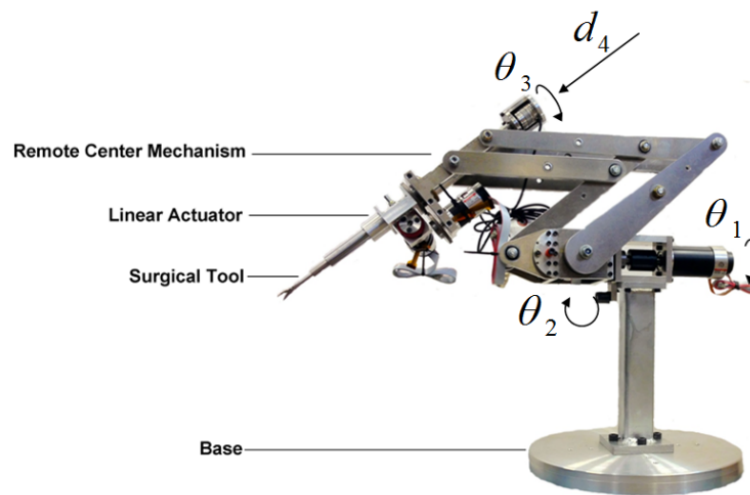


Figure 3.1: Assembled surgical slave mechanism, showing the parallelogram design.

The surgical slave was designed with both kinematic and dynamic requirements in mind. Table 3.1 specifies the various required and achieved capabilities of the individual joints of the developed system.

Table 3.1: Joint requirements and performance for the surgical slave mechanism. Numerals in italics indicate that performance is constrained in software.

Joint	Angle ($^{\circ}$)		Velocity (rad s^{-1})	
	Requirement	System Performance	Requirement	System Performance
Roll (θ_1)	± 35	± 45	0.5	<i>0.66</i>
Pitch (θ_2)	± 35	± 45	0.5	<i>0.66</i>
Yaw (θ_3)	± 180	± 180	1 – 4	2
Extension (d_4)	0.25 m		60 mm s^{-1}	92 mm s^{-1}

Table 3.2 specifies the various required and achieved capabilities in Cartesian space (x, y, z) . Again, it can be seen that the surgical slave mechanism meets all requirements.

Table 3.2: Cartesian space requirements and performance for the surgical slave mechanism.

Axis	Position Resolution (mm)		Force (N)		Natural Frequency
	Requirement	System Performance	Requirement	System Performance	
x	0.1	0.0024	8.9	14.6	14 Hz
y	0.1	0.0012	8.9	9.3	19 Hz
z	0.1	0.0230	8.9 – 20	42	110 Hz

3.1.2 Force Sensing Surgical Tool

There are numerous factors that must be considered when implementing a force sensor into a surgical tool. Questions of sterilisation and biocompatibility need to be addressed, as well as the type and location of the sensor. Sensors located at the distal tip (i.e. inside the patient) need to be extremely small and unobtrusive. Sensors located at the proximal tip (i.e. outside the patient) need to be able to distinguish between environment interaction and gravitational forces (as the surgical tool essentially hangs off the sensor), as well as be isolated from the trocar forces.

The slave design features a force/torque sensor securely fixed to the proximal tip of an inner tube on a linear stage. This inner tube passes through an outer tube, or overcoat, which is then passed through the incision point of the patient. The assembly of the linear stage is shown in Figure 3.2. The overcoat acts as a barrier between the friction and torques encountered at the incision point and the force/torque sensor, essentially isolating the sensor from external forces. Additionally, an accelerometer is placed locally to the force/torque sensor to account for the gravity forces present in the force sensor measurements.

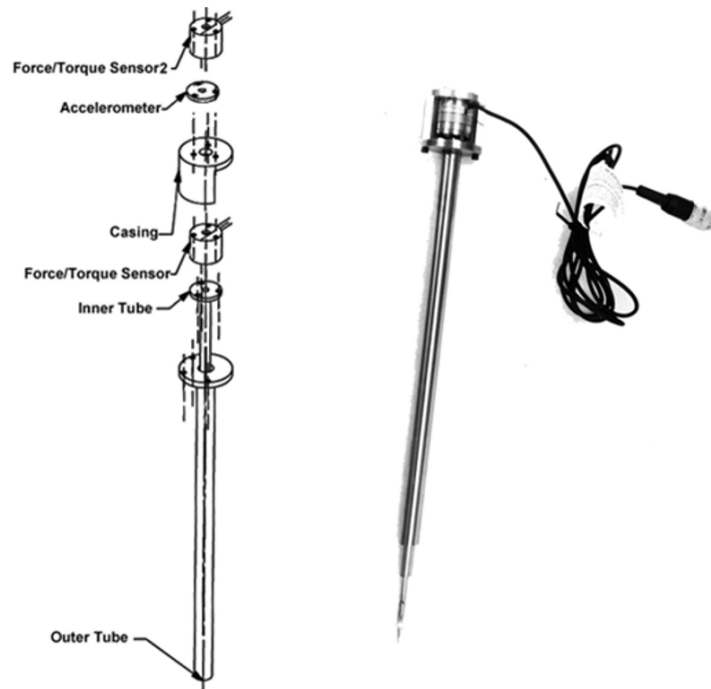


Figure 3.2: Surgical tool assembly, demonstrating the overcoat design and the position of the force/torque sensor and accelerometer on the proximal end of the end-effector.

3.1.3 Sensors and Actuators

Actuation is provided via four Maxon motors, encoders, and gearbox assemblies, located at each DOF. The three rotational axis are controlled via Maxon EPOS2 controllers, which in turn receives commands from the control computer. The linear stage, which houses the surgical tool, is actuated by a Maxon motor via a rubber friction wheel (*drive*). An additional friction wheel is positioned on the opposing side of the linear shaft, and is connected to an encoder (*measurement*). This set-up is shown in Figure 3.3. By separating the motor and encoder via the friction wheels, the linear stage is protected from potential *slip* between the drive wheel and linear stage. Similar to the others, this motor is controlled via the Maxon EPOS2, however the encoder is interfaced with the control computer via a LabJack.

There are two force/torque sensors located along the linear stage: a 6-DOF ATI Nano25 (SI-125-3), with a resolution of ${}_1F \approx 0.06$ N; and a 6-DOF ATI Nano17 (SI-50-0.5), with a resolution of $F \approx 0.01$ N. The Nano17 sensor is used with an admittance control scheme to enable the surgeon to easily position and move the surgical slave

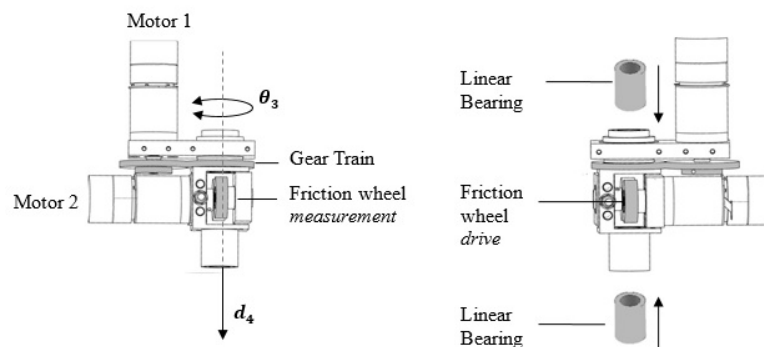


Figure 3.3: Friction wheel assembly for the drive and measurement wheels on the linear stage.

directly. The Nano25 sensor is used to detect the slave-environmental interaction forces, and is the main force/torque sensor used during this research. Full sensor range and resolution are listed in Table 3.3. The sample rate of the sensors is 10 kHz, with blocks of 50 samples averaged for communication with the controller at 200 Hz.

Table 3.3: Characteristics of the Nano25 force torque sensors. The Nano25 is the primary sensor used during experimentation.

	Nano25	Nano17	Unit
<i>Sensor Range</i>			
$F_{x,y}$	± 125	± 50	N
F_z	± 500	± 70	N
$T_{x,y,z}$	± 3	± 0.5	N m
<i>Sensor Resolution</i>			
$F_{x,y}$	0.0208	0.0125	N
F_z	0.0625	0.0125	N
$T_{x,y}$	0.7575	0.0625	N mm
T_z	0.3787	0.0625	N mm

An accelerometer (Digital-ADXL345) is positioned locally to the Nano25 force/torque sensor and provides gravity compensation for the force/torque readings. This compensation process is summarised below in (3.1).

$${}_1F = {}_1F_{gravity} + {}_1F_{inertia} + {}_1F_{interaction} \quad (3.1a)$$

$${}_1F_{gravity} = m_1^2 R_2 A \quad (3.1b)$$

$${}_1F_{inertia} \approx 0. \quad (3.1c)$$

Which yields

$${}_1F_{interaction} = {}_1F - m_1^2 R_2 A. \quad (3.1d)$$

${}_1F$ denotes the forces at the force/torque sensor in the force/torque sensor frame, m is the mass of the end-effector, ${}_2A$ is the accelerations in the accelerometer frame, and ${}_1^2R$ is the rotational matrix which aligns the accelerometer frame to the force/torque sensor frame. It should be noted that both ${}_1F$ and ${}_2A$ include a bias and scaling factor to convert the raw measurements to S.I units (N and m s^{-2}). The calibration of the scaling and bias values, as well as the calculation of the rotational alignment matrix, is covered more completely in [80].

3.2 Haptic Master

The haptic feedback device used during this research is a Sensable Phantom Omni (now known as a Geomagic Touch). A mid-range professional haptic device, it is capable of providing 3 DOF force feedback (x, y, z) via three actuated joints, and 6 DOF position sensing. Digital encoders provide position information in the (x, y, z) axes, while potentiometers provide position information at the rotational gimbal (roll, pitch, yaw). The performance characteristics are detailed below in Table 3.4.

In this research, the role of the Phantom Omni stylus is to provide an interface between the operator and the surgical slave. Motion inputs issued by the operator via the stylus are taken as the feedforward position commands and sent to the surgical slave.

Table 3.4: Performance characteristics of the Phantom Omni haptic feedback device.

	x	y	z
Workspace	160 mm	70 mm	120 mm
Maximum Stiffness	1.26 N mm ⁻¹	2.31 N mm ⁻¹	1.02 N mm ⁻¹
Position Resolution (nominal)	0.055 mm		
Maximum Force (nominal position)	3.3 N		

Similarly, the feedback force, whether direct, quasi-direct, or virtual, are exerted onto the operator via the actuated joints of the Phantom Omni.

The Phantom Omni has an internal control loop, which actions the desired force specified by the PC. However, it does not have the facility to measure the actual asserted force. In the same vein, it does not have force-sensing capabilities to measure the force exerted on it by the operator. This places a limit on the type of bilateral controller which can be used with the Phantom Omni; either 2-channel (P-P, P-F), or 3-channel (P-PF), or any kind of controller that does not require a force *feedforward* channel.

3.3 Controller Design

3.3.1 Position Control

The position controller originally implemented in [80] is a cascaded position-velocity-current loop. The controller consists of three nested control loops; An outer P position loop (200 Hz); a middle PI velocity loop (200 Hz); and an internal PID current loop (10 kHz). The block diagram is shown in Figure 3.4.

The desired input position ($x_d = [x_m; y_m; z_m]$) is received either from a trajectory generator or the master device. The position error (e_x) is used to calculate a desired Cartesian velocity (\dot{x}_d). The inverse Jacobian (J^{-1}) transforms the velocity error from Cartesian (e_x) to joint coordinates ($e_{\dot{q}}$). Gear reductions are applied (G_r), and the desired joint velocities are sent to the Maxon EPOS2 velocity PI loop, which sends a current to each motor (\ddot{q}_d) via an internal PID current control loop. The high gear ratios ensure that the robot mechanism is extremely stiff, with minimal joint compliance.

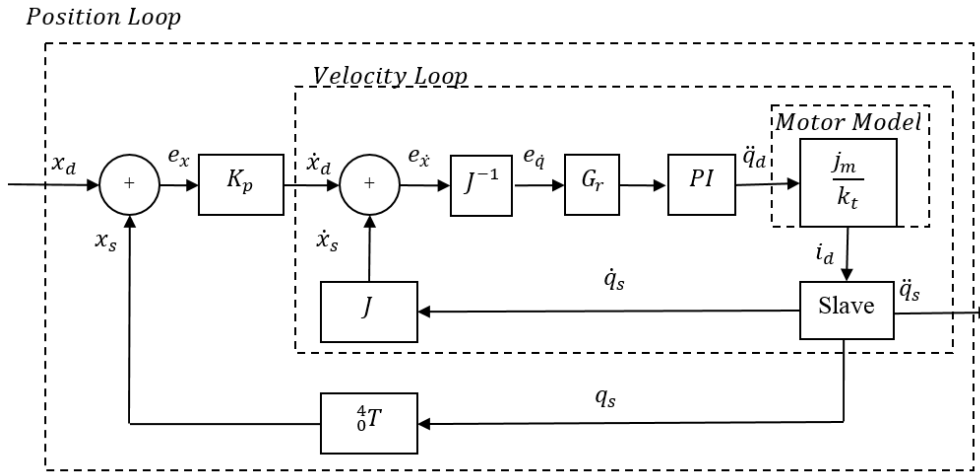
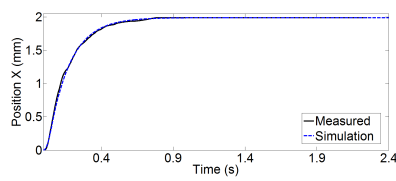
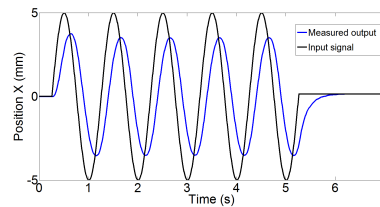


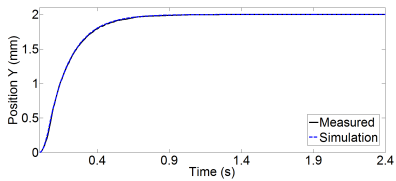
Figure 3.4: Surgical slave mechanism position controller



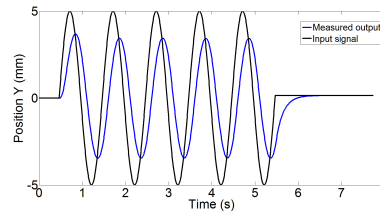
(a) 2mm step input for x-axis



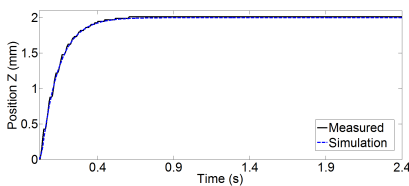
(b) 1 Hz sinusoid input for x-axis



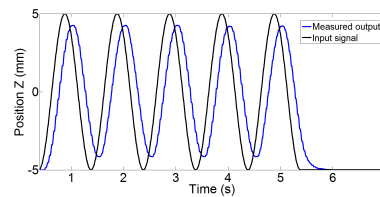
(c) 2mm step input for y-axis



(d) 1 Hz sinusoid input for y-axis



(e) 2mm step input for z-axis



(f) 1 Hz sinusoid input for z-axis

Figure 3.5: System motion bandwidth, and 2 mm step response.

The position P loop gain (K_p) and velocity PI loop gains have been set to achieve minimal overshoot in the slave position, and a motion bandwidth of 1 Hz. The 1 Hz limit is a consequence of the lowest natural frequency being recorded as 14 Hz. To ensure smooth operation of the surgical slave, the motion bandwidth should be 10 times lower than the lowest natural frequency [80]. Thus, a maximum motion bandwidth of

1.4 Hz would be acceptable. As most hand motions fall within the 1 – 2 Hz range, and a surgical procedure would require slow, careful hand motions, a bandwidth of 1 Hz is considered acceptable. The full list of the position- and velocity- loop gains are given below in Table 3.5.

Table 3.5: Position and velocity controller gains.

Gain	Value
<i>Position loop</i>	
K_{pp}	6
<i>Velocity loop</i>	
K_{vp}	280
K_{vi}	1400

The system response to a 2 mm step input, and a 1 Hz sinusoid input are shown in Figure 3.5. The 1 Hz sinusoid represents the motion bandwidth of the system, as the steady-state magnitude is reduced to $\sqrt{\frac{1}{2}}$ (0.707, or 3 dB) of the input magnitude.

The rise time (time from 10 % to 90 % of the command value) was approximately 0.35 s for each of the axis with a 2 mm step input. Although this could be improved by increasing the position-loop K_{pp} value, doing so would increase the bandwidth too close to the lowest natural frequency of 14 Hz, and cause unwanted vibrations.

As it is, the delay time between command position and robot response can be considered as an induced network delay, at least on the position-forward path. An exact value for this delay cannot be given, however it is estimated that the time delay between the slave and master subsystems is between 200 – 400 ms.

Robot Precision

The precision of the robot, and validation of the robots' forward kinematics, is demonstrated in Figure 3.6. Each axis is commanded to follow a 1 Hz sinusoid trajectory. An API (Automated Precision Inc.) laser tracker was utilised to provide a highly calibrated

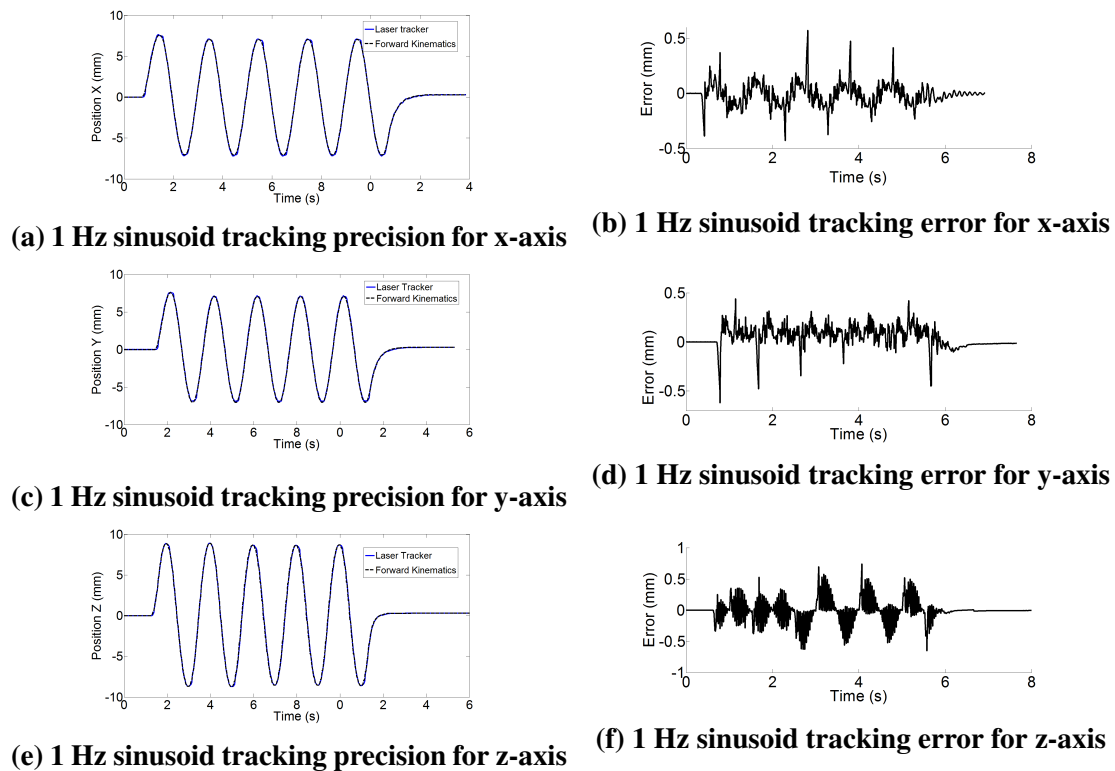


Figure 3.6: System motion bandwidth, and 2 mm step response.

external position reference of the end-effectors motion. By comparing the position calculated internally via the forward kinematics with the externally referenced laser tracked position, a measure of precision can be established.

Tracking errors remain, for the most part, under 0.5 mm, with slight peaks in tracking error occurring as each axis changes direction. This effect is likely caused by backlash within the gears, as the teeth engage on the opposing edge. Joint compliance, system vibrations, and manufacturing tolerances also contribute to the tracking error. However, Figure 3.6 indicates that the tracking error are minimal and acceptable.

3.3.2 Force Feedback

For bilateral teleoperation control, a force feedback path was included to provide a kinaesthetic link between the operator and environment. The complete block diagram for the teleoperated system is shown in Figure 3.7. As with the position controller, the force-feedback controller operates at 200 Hz.

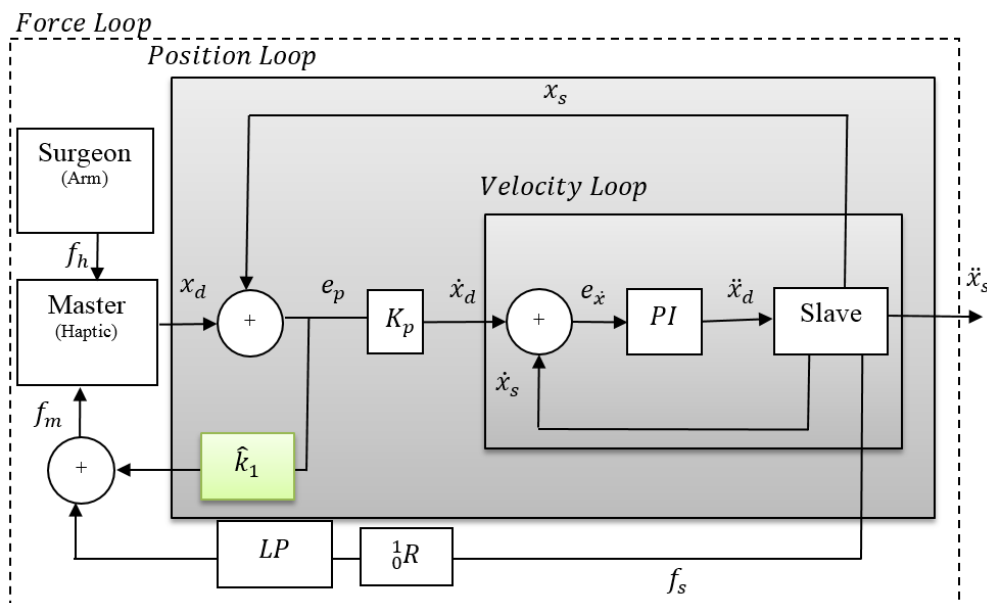


Figure 3.7: Bilateral teleoperator controller. Includes the slave position controller, as well as the operator and master systems. A force feedback channel completes the bilateral controller

Of note is the addition of the force feedback path from the slave (f_s), through an alignment matrix (1_0R) and low-pass filter (LP), to the master. Complementing this path is an adaptor, (\hat{k}_1), which acts to introduce a virtual stiffness between the slave and the master, which greatly improves teleoperation stability and transparency.

The adaptor is calculated as the average stiffness across the contact environment at time-step k :

$$\hat{k}_1[k] = \left| \frac{f_s[k] - f_{contact}}{x_s[k] - x_{contact}} \right| \quad (3.2)$$

By coupling the feedback force with an adaptive stiffness, a quasi-virtual environment (or quasi-direct feedback) methodology is established.

3.4 Summary

This chapter provided a brief summary the design and performance of the teleoperated surgical system that was utilised during this research. The design was performed in [80], where a more in-depth analysis can be found. The design features are summarised as follows:

- A double parallelogram design, which has a mechanically constrained remote centre-of-motion and a compact design.
- A proximally located force sensing surgical tool which is able to isolate the tool-patient interaction forces from the trocar and gravitational forces via an overcoat and accelerometer, respectively

Additionally, a bilateral controller is included that provides:

- A cascaded position-velocity controller with system gains set such that motion bandwidth is 1 Hz, and a system response which has no overshoot
- A force-feedback path that utilises an adaptive stiffness between slave and master.

Recommended design improvements are:

- Increase the lowest natural frequency from 14 Hz to at least 20 Hz. This would enable the PI gains to confidently be increased to achieve a motion bandwidth of 2 Hz, resulting in a stronger coupling between master and slave position. However, an increase in the slave mechanisms stiffness would be required.

Chapter 4

Development of Predictive Force Feedback

This chapter focuses on the development and implementation of an *estimation-prediction* force feedback methodology into a bilateral teleoperated RMIS system. Firstly, at the slave a mathematical force model is specified to describe the behaviour of the environment force. While the slave is in contact with the environment, the model parameters are *estimated* via an exponentially weighted recursive least squares (EWRLS) function. With the estimated parameters, a virtual environment is created which the master interacts with, *predicting* the environment response appropriate to the master's own kinematics. The performance and behaviour of the EWRLS parameter estimator is experimentally validated by palpating the slave end-effector against a polyurethane foam, via a sinusoid motion input. Experimental results reveal the importance of maintaining consistent input signals to the EWRLS algorithm, with inconsistent signal delays causing improper parameter estimations.

4.1 The Estimation - Prediction Controller

For bilateral teleoperators, the time delay between the slave and the master has a detrimental effect on system transparency and stability. Forces measured at the slave are

only received by the master after experiencing a communication delay intrinsic to all physical systems. Likewise, position commands sent from the master to the slave undergo similar delays. For direct or semi-direct position-force teleoperators, the slave and the master subsystems are only able to respond to information after-the-fact, and the cause-effect relationship between action and reaction is compromised. This is compounded when the system gains are relatively low, as is the case with the developed RMIS system detailed in Chapter 3.

To counter this, an *estimation* and *prediction* methodology can be used to replace the feedforward and/or feedback paths within the control system. *Estimating* the environment involves building a mathematical representation of how the environment will respond. The *predictive* step then uses this representation to predict the subsystem response.

Estimating and predicting position is difficult, as in a position-force bilateral teleoperator, position is governed by the operator(s). However, estimating and predicting the environment force can be readily performed, as the environment typically a predictable response.

The proposed control structure for an estimation-prediction based force feedback path is presented in Figure 4.1. The environment estimation process is based on an exponentially weighted recursive least squares (EWRLS) algorithm, used in conjunction with a pre-selected force model. The resolved environment parameters are sent to the master, and the force model used in conjunction with the master kinematics to produce a predicted force feedback.

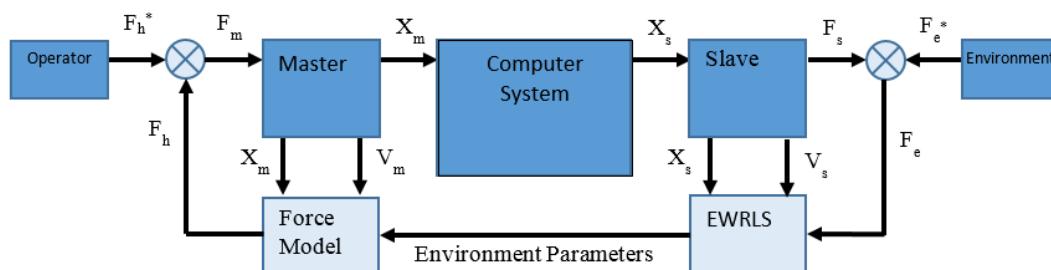


Figure 4.1: Environment estimation and force prediction control structure.

4.1.1 Force Models

The proposed control scheme relies heavily upon the appropriate choice of the underlying force model. If the model does not accurately represent the surgical environment, then both transparency and stability can be dramatically compromised.

Kelvin-Voight Force Model

The Kelvin-Voight (KV) force model (4.1), also known as a parallel spring-damper model, has been used extensively in environment contact modelling due to its innate linearity and computational simplicity. The equation used in modelling soft-body contact may be written as

$$\mathbf{F}_e(t) = \begin{cases} K_{KV}\mathbf{x}(t) + B_{KV}\dot{\mathbf{x}}(t), & \mathbf{x}(t) \geq 0 \\ 0 & \mathbf{x}(t) < 0 \end{cases} \quad (4.1)$$

where \mathbf{F}_e is the environment force, $\mathbf{x}(t)$ denotes the penetration into the soft-body, $\dot{\mathbf{x}}(t)$ is the velocity inside the contact environment, and K_{KV} and B_{KV} are the Kelvin-Voight stiffness and damping parameters, respectively.

The KV model has several physical inconsistencies that makes it non-ideal in modelling soft-contact environments. A non-zero velocity at the boundary (i.e. $\mathbf{F}_e \neq 0$ when $|x| = 0$ and $|\dot{x}| > 0$) results in a non-zero contact force. This translates to a “shock” force during insertion, and a “sticking” feeling during retraction, labelled as point A and B, respectively, in Figure 4.2 (a). More specifically, power exchange between tool and environment is inconsistent with physical reality, indicated by the non-zero final power value in Figure 4.2 (b). Additionally, the majority of biological soft tissues are non-linear, and a linear model such as the Kelvin-Voight model is ill suited to predict the behaviour of such contact environments.

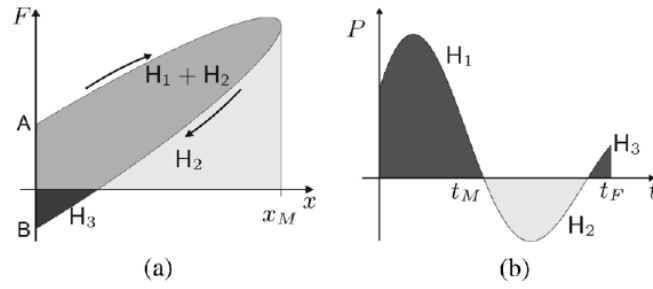


Figure 4.2: Impact behaviour of the Kelvin-Voigt force model.

Hunt-Crossley Force Model

The Hunt-Crossley force model (4.2) attempts to address the above issues by including a position dependence into the damping term. Similarly, the exponent on the position term provides the non-linearity necessary to model biological soft tissues.

$$\mathbf{F}_e(t) = \begin{cases} K_{HC}\mathbf{x}^n(t) + B_{HC}\mathbf{x}^n(t)\dot{\mathbf{x}}(t), & \mathbf{x}(t) \geq 0 \\ 0 & \mathbf{x}(t) < 0. \end{cases} \quad (4.2)$$

In (4.2), the parameters are labelled as K_{HC} , B_{HC} and n , to denote the Hunt-Crossley specific stiffness, damping, and non-linearity parameters, respectively.

The non-linearity of (4.2) means that traditional methods to resolve the parameters K_{HC} , B_{HC} and n are not applicable, as most on-line parameter estimation techniques are only valid for linear systems. To overcome this, a linearised form of the Hunt-Crossley force model is used during the estimation process:

$$\ln[F_e] \cong \ln(K_{HC}) + \frac{B_{HC}}{K_{HC}}\dot{x}_s(t) + n \ln[x_s(t)] + \frac{\epsilon}{K_{HC}x_s^n(t)}. \quad (4.3)$$

The derivation of (4.3) can be found in [38]. The error term, ϵ , includes the modelling error that arises from the log-linearised form, as well as sensor noise. For this research, ϵ is assumed to be negligible to the estimation process.

4.1.2 Estimating the Environment Parameters

The estimation process uses either the Kelvin Voight or Hunt Crossley force model as the basis, and by taking the slave system dynamics ($x_s(t)$, $\dot{x}_s(t)$ and $F_e(t)$), resolves the respective environment parameters. It is these parameters, and not the interaction force, that is then used by the master to determine the master force feedback. Ideally, the estimation process would:

- quickly converge the estimated environment parameters to the actual environment parameters
- be resolvable on-line
- be able to adapt to a changing environment
- have good noise rejection.

Exponentially Weighted Recursive Least Squares Estimation

The recursive least squares (RLS) algorithms are adaptive filters which recursively find the coefficients that minimise a least squares cost function for a linear system. They are useful for on-line estimation tasks as they exhibit extremely fast and robust convergence. The exponentially weighted recursive least squares (EWRLS) algorithm is particularly suited to estimating models with dynamic properties, as the relative speed of convergence can be pre-defined. The EWRLS algorithm takes a linear equation of the form

$$y_k = \phi_k^T \theta_k \quad (4.4)$$

and recursively calculates an estimate for θ_k at each time-step. In (4.4), ϕ_k are the input samples at time-step k , and y_k is the measured response. An estimation for θ_k , labelled as $\hat{\theta}_k$, is given via the update equations, as defined below.

$$\mathbf{L}_k = \frac{\mathbf{P}_{k-1}\phi_k}{\lambda + \phi_k^T \mathbf{P}_{k-1} \phi_k} \quad (4.5a)$$

$$\mathbf{P}_k = \frac{1}{\lambda} [\mathbf{P}_{k-1} - \mathbf{L}_k \phi_k^T \mathbf{P}_{k-1}] \quad (4.5b)$$

$$\hat{\boldsymbol{\theta}}_k = \hat{\boldsymbol{\theta}}_{k-1} + \mathbf{L}_k [y_k - \phi_k^T \hat{\boldsymbol{\theta}}_{k-1}]. \quad (4.5c)$$

In (4.5), \mathbf{P} is the covariance matrix of the dynamic parameters ($\boldsymbol{\theta}_{k-1}$), λ is the forgetting factor, and $\hat{\boldsymbol{\theta}}_k$ is the updated *estimated* parameters.

The forgetting factor, λ , defines the relative weight previous measurements have when generating the current parameter estimate. When $\lambda = 1$, (4.5) becomes the RLS algorithm, where all input values have equal weight in the determination of the system parameters. A value of $\lambda < 1$ assigns greater weight to more recent input values, and thus enables a faster response to dynamic environments, at the cost of decreased stability. Typically $0.98 \leq \lambda \leq 1$ is an acceptable range for the forgetting factor.

Table 4.1: Linearized force models used in the EWRLS algorithm.

	Kelvin-Voigt	Hunt-Crossley
\mathbf{y}_k	$[\mathbf{F}_k]$	$[\ln(\mathbf{F}_k)]$
ϕ_k^T	$[\mathbf{x}_k, \dot{\mathbf{x}}_k]$	$[1, \dot{\mathbf{x}}_k, \ln(\mathbf{x}_k)]$
$\boldsymbol{\theta}_k$	$[K_{KV}, B_{KV}]^T$	$[\ln(K_{HC}), \frac{B_{HC}}{K_{HC}}, n]^T$

Table 4.1 provides the linearly parametrised environment dynamics used in the EWRLS algorithm.

4.1.3 Predicting Force Feedback

At each time-step, the EWRLS algorithm uses the slave dynamics to resolve an estimate for the environment parameters of the given force model. These parameters are then used to create a virtual environment with which the haptic device will interact. Provided the model is valid for the material, and the estimated parameters converge to the true

environment parameters, then the virtual environment can confidently be used to provide transparent haptic feedback. For example, using the Hunt-Crossley force model, the haptic feedback force would be given by

$$\mathbf{F}_m(t) = \begin{cases} K_{HC}\mathbf{x}_m^n(t) + B_{HC}\mathbf{x}_m^n(t)\dot{\mathbf{x}}_m(t), & \mathbf{x}_m(t) \geq 0 \\ 0 & \mathbf{x}_m(t) < 0 \end{cases} \quad (4.6)$$

Equation (4.6) uses the haptic stylus kinematics ($\mathbf{x}_m(t)$ and $\dot{\mathbf{x}}_m(t)$) and environment parameters (K_{HC} , B_{HC} and n) to resolve the feedback force, $\mathbf{F}_m(t)$. The same process is used for the Kelvin-Voight force model, albeit with the Kelvin-Voight force equation used as the basis.

4.2 A Metric for Teleoperator Performance

The proposed bilateral controller has two definitions of error that are of interest: *estimation error*, and *prediction error*, with each definition describing the accuracy of different processes. Additionally, there is the optimal solution, which is the set of parameters which yields the lowest RMSE for the given data. If the environment parameters are immutable, then the optimal solution will provide the lowest error.

The estimation error is localised to the slave-environment interaction, and indicates the accuracy of the estimator in reference to the measured environment. The estimation error is localised to the dynamics of the slave.

The prediction error relates the interaction between the master and virtual environment to the interaction of the slave with the measured environment. The prediction error encompasses the master's dynamics, which typically extends beyond the range of the slave-environment dynamics. As such, the prediction error provides an indication of *system* transparency, whereas estimator error indicates *estimator* transparency.

Off-line verification of the estimated parameters, and the general ability of the force models to describe the environment, is conducted via the optimal solution.

4.2.1 Estimation Error

Estimator error is the error between the measured slave-environment force and the estimated force provided by the EWRLS estimator. It demonstrates how well the estimated parameters represent the measured environment at each time-step. The family of RLS algorithms utilises this error internally as a means to constantly update its progressive estimations. The term

$$y_k - \phi_k^T \hat{\boldsymbol{\theta}}_{k-1} \quad (4.7)$$

in (4.5c) calculates the estimation error based on the previously estimated parameters. In the context of this research, the estimation error is defined as:

$$e_{est}[k] = F_s[k] - \phi_s[k]^T \hat{\boldsymbol{\theta}}[k]. \quad (4.8)$$

This error is confined to the slave-environment interaction, and is a good indicator of how well the EWRLS algorithm is replicating the true environment, in the context of the slave kinematics.

4.2.2 Prediction Error

Evaluating the prediction error is more involved, but subsequently more useful in determining teleoperation performance. Here, prediction error is the error between the predicted master force and the measured slave forces at a given position. It is used as a de-facto metric for transparency, given that it evaluates how well the predictive force feedback mechanism is operating in terms of the teleoperation system as a whole.

Calculating the prediction error involves the comparison between the current measured force, and the predicted master force an unknown amount of time previously. This is because, at each time-step, the slave and the master are typically at different positions within the real or virtual environment, and thus are expected to experience different forces. The measured force of the slave, and predicted forces of the master cannot simply be compared to each other directly at each time-step. Instead, the forces are compared when the slave and the master kinematics are as similar as possible.

This is accomplished by:

- Taking the slave position (x_s) and force (F_s) at each time-step (k_s), and using these as the slave reference;
- Searching through the dataset of the master positions, backwards from the slave reference time-step, for the first closest master position (x_m) to x_s .
- Comparing the direction of motion of the slave and master to ensure the two systems were travelling in the same direction. If the directions differ, then the next closest slave and master positions are used.
- The time-step when the positions are closest, and direction of travel is consistent, is k_m , and is used as the master reference;
- Finding the error between the slave force ($F_s[k_s]$) and the master force ($F_m[k_m]$) at their respective reference time-steps.

More rigorously, the prediction error, $e_{pred}[k_s]$, at time-step k_s is presented as

$$e_{pred}[k_s] = F_m[k_m] - F_s[k_s] \quad (4.9)$$

for

$$k_m < k_s \quad (4.10a)$$

$$x_m[k_m] \approx x_s[k_s] \quad (4.10b)$$

$$\text{sgn}(\dot{x}_m[k_m]) = \text{sgn}(\dot{x}_s[k_s]). \quad (4.10c)$$

The above method attempts to determine how accurate the predicted force *was*, once the slave has passed through the previous master position; the error analysis is *a posteriori*, as opposed to current.

4.2.3 Optimal Solution

The optimal solution is the set of environment parameters which best adhere to the measured data. These parameters are calculated off-line, once each experiment has taken place.

The optimal solution offers insight into whether the selected force model adequately describe the given environment, via the R^2 and RMSE values.

Comparing the estimation error to the error of the optimal parameters indicates how well the estimated parameters have converged to the optimal values for the experimental data. A noticeable difference in parameters would indicate that the EWRLS estimator is not performing adequately, not excited sufficiently, or stopped too quickly.

4.3 Experimental Validation of the EWRLS Estimator

4.3.1 Experimental Set-up and Procedure

Implementing the control methodology described above is relatively straightforward. Minimal changes have been made to the previous control structure presented in Chapter 3 (Figure 3.4). Feedback has been limited to 1 DOF (along the linear Z-extension stage) to simplify the experimental validation process.

The developed estimation-prediction controller is shown in Figure 4.3. In grey are the velocity and position loops, which were previously seen in Figure 3.4. The EWRLS estimator and force predictor are highlighted in green, and connects the slave-side estimator to the master-side predictor via the estimated environment parameters K , B , and n .

Each time-step, the estimator receives the slave position, velocity, and force and recursively estimates values for the environment parameters. The predictor then uses these parameters to create a virtual environment and, by referencing the master position and velocity, predicts the appropriate level of force feedback to the operator.

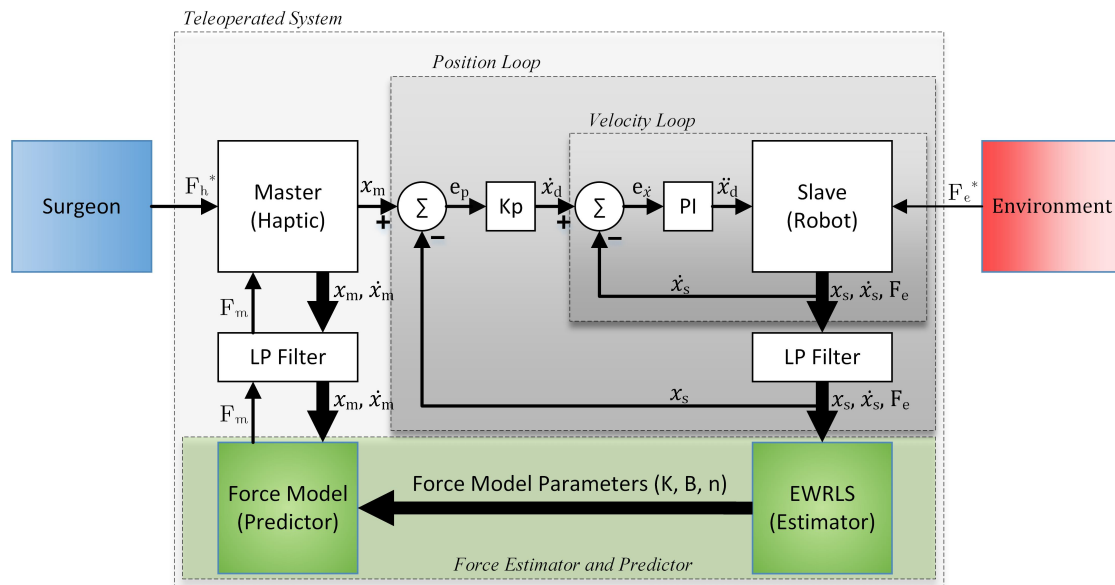


Figure 4.3: Developed bilateral controller, utilising the *estimation - prediction* force feedback methodology, highlighted in green.

A first-order Butterworth filter act as a low-pass filter for all the control variables involved in force-feedback. Within the EWRLS algorithm both the underlying force-model and forgetting factor can be set by the user, although remain constant throughout the initial experimental phase.

All experiments performed use the teleoperated system described in Chapter 3. The user was a 27-year-old male, familiar with the operation of the teleoperated system. The controller shown in Figure 4.3 was used, albeit with small changes necessary for individual experiments.

The experimental set-up of the slave in contact with the polyurethane foam is shown in Figure 4.4. For these experiments, the robot motion was driven by a sinusoidal trajectory in the z -axis (vertical in Figure 4.4). A polyurethane foam was chosen as the soft contact environment as it exhibits non-linear compression, has a low stiffness, and non-permanent deformation.

Initial values for the EWRLS estimator were kept constant across all experiments, and are given in Table 4.2. *A priori* knowledge about the behaviour of the material was kept to a minimum, with the goal of making minimal assumptions about the expected values for the environment parameters. For the EWRLS algorithm, the initial covariant

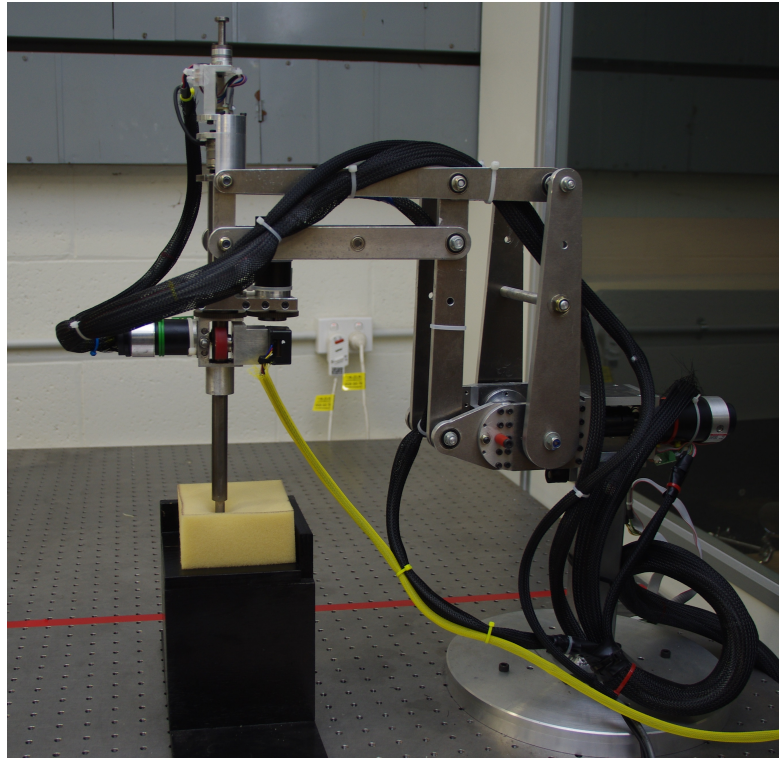


Figure 4.4: Surgical robot (slave) in contact with the polyurethane foam.

Table 4.2: Initial values for estimation algorithm. Values are reset at the beginning of each experiment. It must be noted that the Kelvin-Voight model does not use parameter n .

Parameter	Initial Value
<i>Environment Parameters</i>	
K	0.5 N mm^{-1}
B	0.01 N s mm^{-1}
n	2.00
<i>EWRLS Algorithm</i>	
\mathbf{P}_0	\mathbf{I}
λ	0.999

matrix (\mathbf{P}_0) was set to the identity matrix (\mathbf{I}). Higher values in the diagonal of (\mathbf{P}_k) correspond to more uncertainty within the estimated dynamic parameters, and thus more variation. It is not desirable to have large variations in dynamic parameters initially, as this can lead to unstable behaviour at initial contact. As such, the variance of each parameters was initially set to 1.

Experiments were conducted over two phases, addressing two key areas:

- The ability of the EWRLS estimator to confidently resolve the environment parameters;
- The performance of the predictive force feedback methodology with a human operator.

The first key area is addressed in the remainder of this chapter, where only the estimation process is investigated. The second key area is presented in Chapter 5, where the full teleoperation system is evaluated via human-in-the-loop palpation experiments.

4.3.2 Experimental Results

In this experiment, the master position input signal was replaced by a computer generated trajectory. To ensure that the EWRLS estimator receives sufficient persistency of excitation, a sinusoidal trajectory with three distinct frequencies was used, given by

$$x(t) = x_0 + 1.2\sin(2\pi 0.6t) + 2.3\sin(2\pi 1.5t) + 1.6\sin(2\pi 2.4t). \quad (4.11)$$

Force feedback was disabled during this experiment, as the position input was driven purely from the computer system, and a human operator was not included in the control loop. Slave position, velocity, and force were all used by to the EWRLS algorithm simultaneously for both the Kelvin-Voight and Hunt-Crossley force models, with the environment parameters estimated for both models. This experiment was designed to address two questions:

- Do the estimated environment parameters converge to acceptable values?
- What effect does filtering have on the estimated parameters?

Filter Induced Delay

Initially only the slave velocity and force was filtered by a first-order Butterworth filter. Position was excluded from filtering due to the 1 Hz motion bandwidth of the slave, and the position signal having minimal noise when compared to the force and velocity signals. A cut-off frequency of 2 Hz for both velocity and force was initially used, as most

purposeful hand motions fall within the 0 – 2 Hz range. However, as will become apparent, the delay induced by the filter can severely compromise the EWRLS algorithms' ability to estimate accurately the environment parameters *if there is inconsistent delay between individual input signals*.

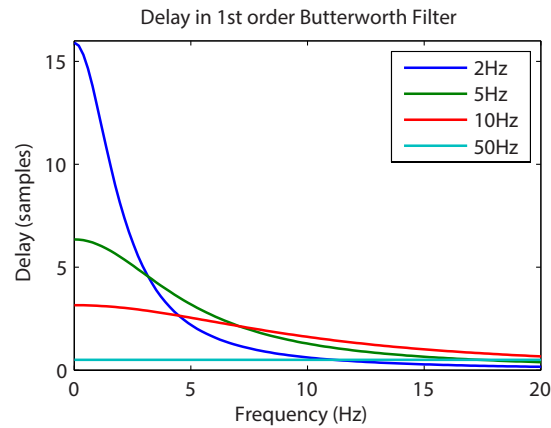


Figure 4.5: Frequency-dependant delay of a first-order Butterworth filter with a sample rate of 200Hz.

Filtering a noisy signal inevitably adds a delay to the smoothed output. The filter used in this investigation was a first-order low-pass Butterworth filter, which is classed as an Infinite Impulse Response (IIR) filter. IIR filters add a *frequency dependant* delay to the filtered signal, and any process that is sensitive to signal *phase* is not suited to IIR filters. This delay is shown in Figure 4.5.

Velocity-Force Filtering

Figure 4.6 and Figure 4.7 show the estimated environment parameters when only slave *velocity* and *force* are filtered. It is apparent that the phase distortion introduced by the IIR filter predominantly results in a decrease in the damping coefficient. When the velocity and force are filtered with a cut-off frequency of 2 Hz, the estimated damping coefficients converges to approximately $B_{KV} \approx -5.9 \times 10^{-3} \text{ N s mm}^{-1}$ for the Kelvin-Voight model, and $B_{HC} \approx -6.8 \times 10^{-5} \text{ N s mm}^{-1}$ for the Hunt-Crossley model. These negative values result in a highly unstable system, and will inject energy into the tele-operated system, violating the passivity condition on the (virtual) environment. A 5 Hz

cut-off frequency shows similar behaviour, with the damping coefficients converging between $B_{KV} \approx -5.2 \times 10^{-4}$ to 8.5×10^{-4} N s mm⁻¹ and $B_{HC} \approx -1.2 \times 10^{-5}$ N s mm⁻¹ for the Kelvin-Voight and Hunt-Crossley models, respectively.

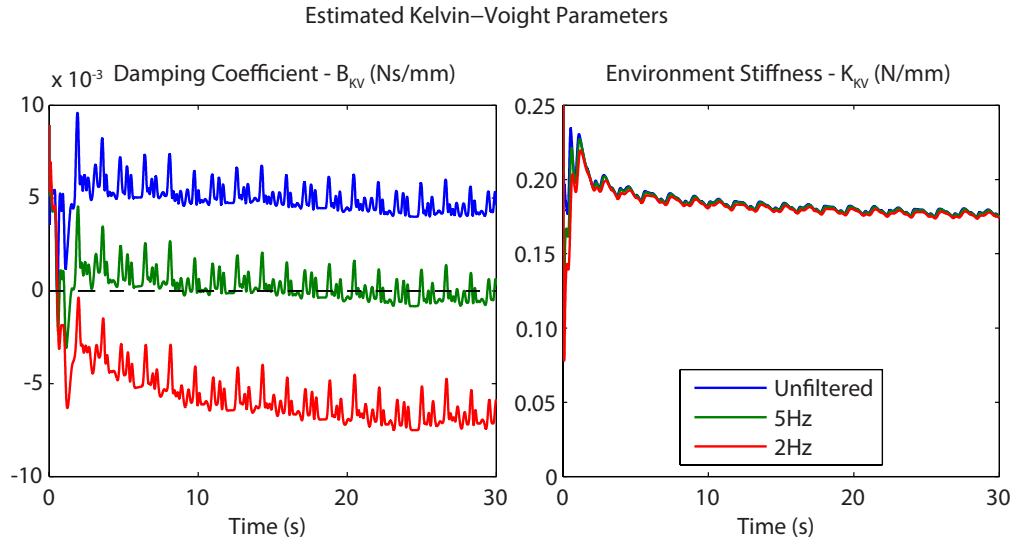


Figure 4.6: Estimated Kelvin-Voight environment parameters of a polyurethane foam, when the low-pass filter cut-off frequency is varied for the slave *velocity* and *force* signals.

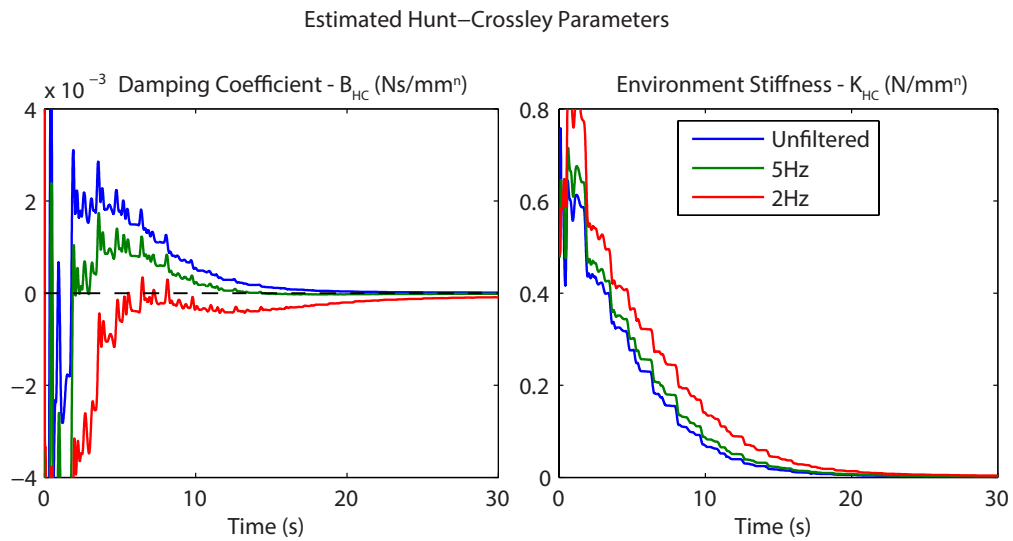


Figure 4.7: Estimated Hunt-Crossley environment parameters of a polyurethane foam, when the low-pass filter cut-off frequency is varied for the slave *velocity* and *force* signals.

Unfiltered, the damping coefficients converge to $B_{KV} \approx 4.7 \times 10^{-3}$ N s mm⁻¹ and $B_{HC} \approx 9.0 \times 10^{-6}$ N s mm⁻¹. The environment stiffness experienced little change between convergent values across each of the velocity-force filtered data-sets.

The delay between the unfiltered slave position and filtered slave velocity and force results in the estimation algorithm misattributing changes in force to a change in the environment parameters, namely the damping coefficient. As position is not filtered, a change in position arrives at the estimator prior to the (filtered and delayed) changes in velocity and force. The estimator interprets this change in position as a *change in parameter*, due to the lack of corresponding change in the velocity and force inputs. As seen in Figure 4.6 and Figure 4.7, the damping coefficient absorbs the majority of this change, and converges below the expected value.

Position-Velocity-Force Filtering

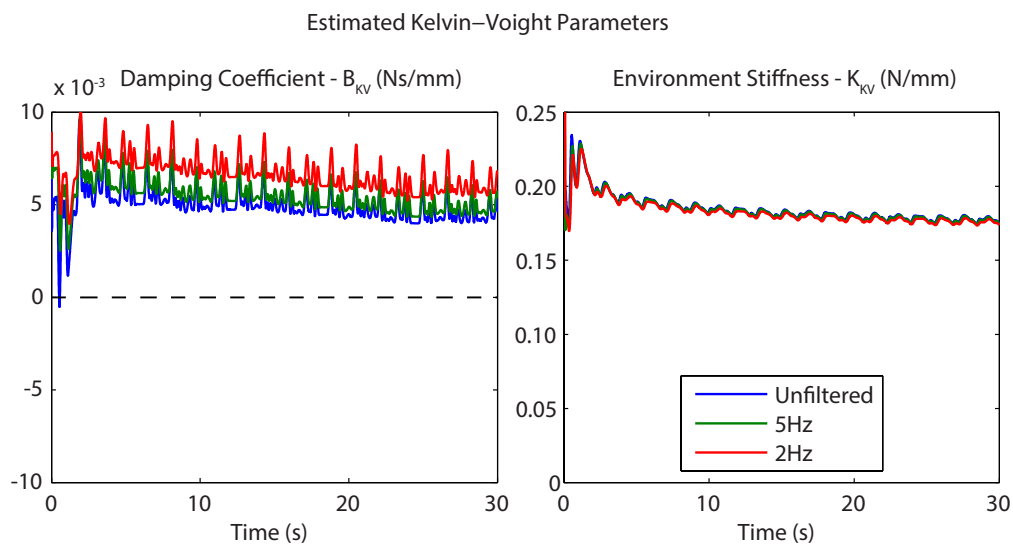


Figure 4.8: Estimated Kelvin-Voight environment parameters of a polyurethane foam, when the low-pass filter cut-off frequency is varied for the slave *position, velocity and force* signals.

Figure 4.8 and Figure 4.9 demonstrate how filtering *all* of the slave signals affect the estimation algorithm. Including the slave position signal into the filter induces the same delay as the velocity and force. In Figure 4.8, the Kelvin-Voight damping coefficient converges higher with a more aggressive filter; the opposite of what was seen when the filter was only applied to the velocity and force. However, the coefficients no longer converge to a negative value, and thus stability is not compromised. A similar effect can be seen in Figure 4.9, with the Hunt-Crossley model.

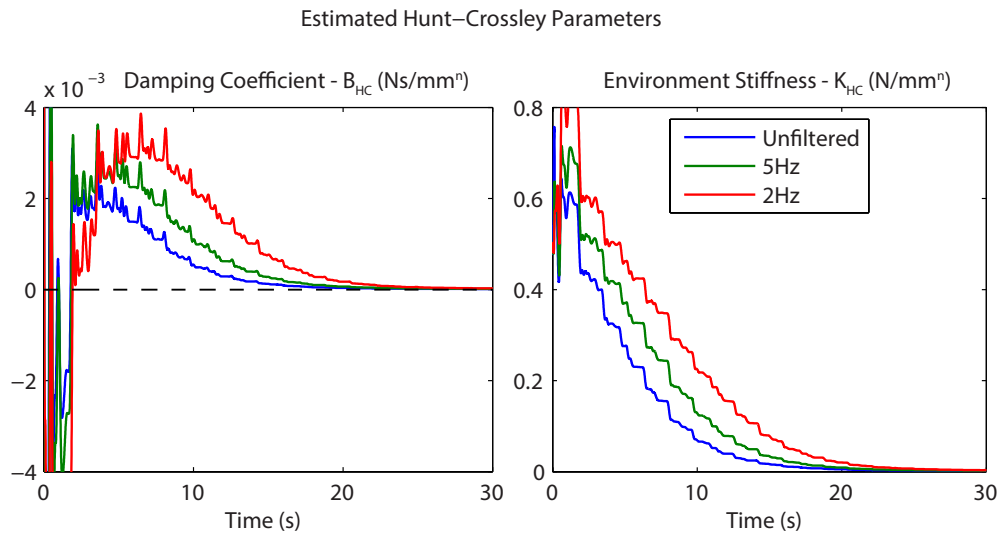


Figure 4.9: Estimated Hunt-Crossley environment parameters of a polyurethane foam, when the low-pass filter cut-off frequency is varied for the slave *position*, *velocity* and *force* signals.

Discussion

The above results indicate that filtering the input variables too vigorously or inconsistently has an adverse effect on parameter estimation. The EWRLS algorithm is sensitive to the phase cohesion of the respective input variables, and as such only minimal signal filtering should be used by the estimator. While comparatively noisy, the unfiltered velocity and force signals are not unusable, as the EWRLS algorithm has good noise rejection and, as the data-set grows, offers little issue in dealing with noisy data.

Interestingly, it was observed that the estimation error varies little across the above experiments, indicating that in the context of the slave-environment interaction, the EWRLS algorithm is not significantly affected by the various signal filtering and delays. However, extending these values to the operator-master interaction can lead to significant stability issues. The estimation root-mean-squared errors (RMSE) for the estimator are given below in Table 4.3.

From the above, the lowest estimation error occurs when the velocity-force signals are filtered to 2 Hz. However, this is primarily due to the force signal being smoothed considerably by the filter. Unfiltered, the force signal is noisy, which contributes to the estimator error.

Table 4.3: Estimation RMSE of the EWRLS algorithm across various filter combinations. VF indicates only velocity and force are filtered. PVF indicates position, velocity, and force were all filtered.

	Unfiltered	5 Hz PVF	2 Hz PVF	5 Hz VF	2 Hz VF
Hunt-Crossley (N)	0.214	0.217	0.202	0.201	0.188
Kelvin-Voigt (N)	0.344	0.325	0.278	0.321	0.272

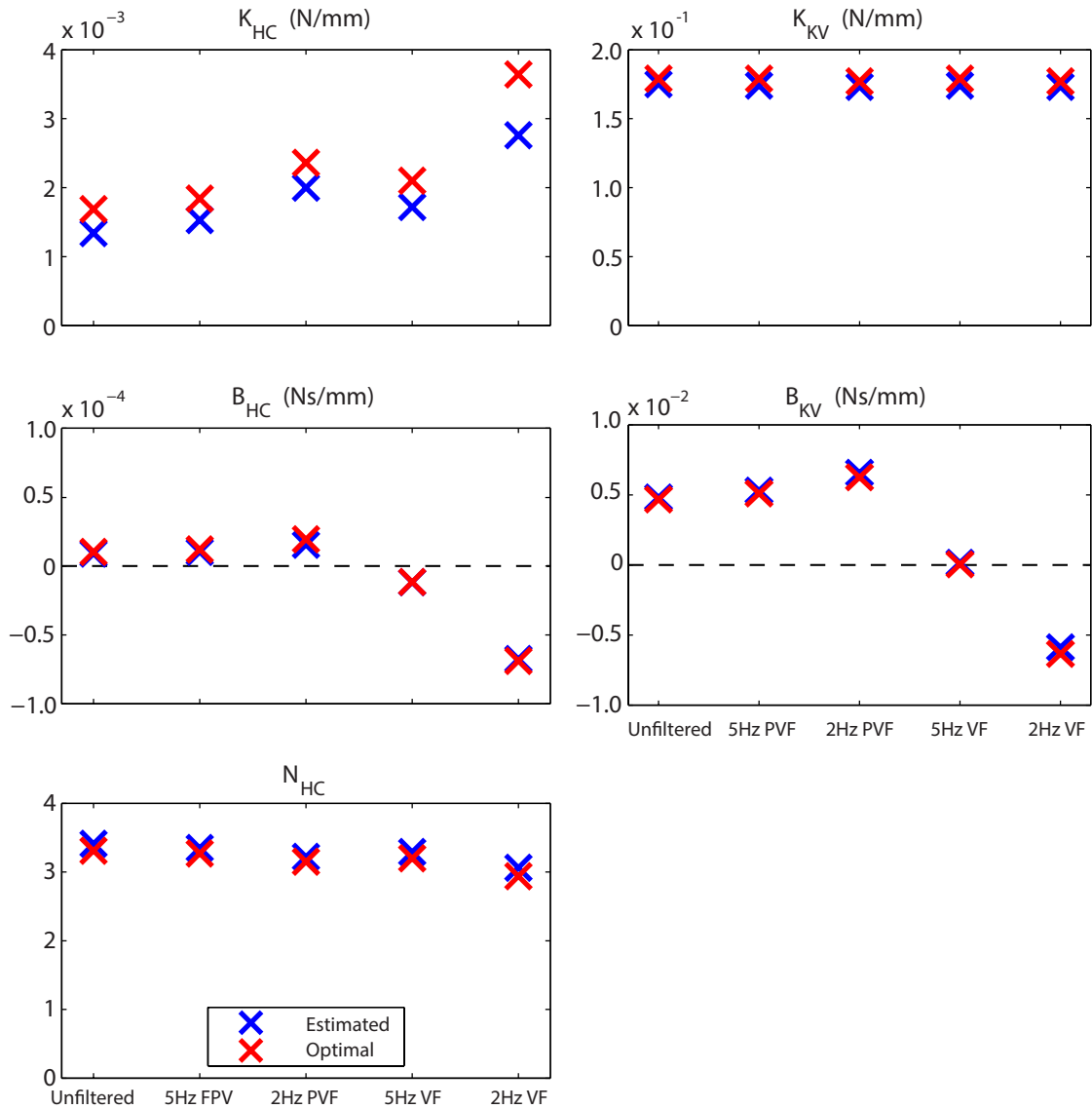


Figure 4.10: Comparison of final estimated parameters to optimal parameters, across various filter combinations, for both the Hunt-Crossley (left) and Kelvin-Voigt (right) force models. VF indicated only velocity and force are filtered. PVF indicates position, velocity, and force are filtered.

The estimated parameters, averaged over the final 5 s of palpation, is compared to the optimal parameters below in Figure 4.10. The damping coefficient dropping into negative values can clearly be seen for the velocity-force (VF) filtered data in both the Hunt-Crossley (left) and Kelvin-Voigt (right) force models. There is also a clear difference between estimated and optimal stiffness coefficients for the Hunt-Crossley model, where the estimated value is consistently lower than the optimal value. This is likely due to the forgetting factor being set to $\lambda = 0.999$ (which yields a relatively slow convergence), coupled with the additional parameter in the force model (n).

Finally, the RMSE of the optimal parameters to measured force is shown in Table 4.4. As can be seen, the RMSE for the optimal Hunt-Crossley solution is low, demonstrating that the model is a good representation of the environment. The optimal Kelvin-Voigt solution has significantly higher error, indicating that the linear model does not represent the non-linear environment.

Table 4.4: RMSE the optimal solution of the Hunt-Crossley and Kelvin-Voigt force models to the measured data, for various filter combinations.

	Unfiltered	5 Hz PVF	2 Hz PVF	5 Hz VF	2 Hz VF
Hunt-Crossley (N)	0.096	0.080	0.082	0.075	0.082
Kelvin-Voigt (N)	0.346	0.327	0.281	0.324	0.276

For the following experiments, a cut-off frequency of 5 Hz for the slave signals can be considered as a good compromise between noise minimisation and estimation robustness, provided *all* input parameters are filtered consistently. Alternatively, the unfiltered data can be used, although this makes it harder to ascertain conditions such as environment contact, as the signal-to-noise ratio may be too low for meaningful contact detection.

4.4 Summary

In this chapter, a proposed *estimation-prediction* bilateral controller was presented, where the direct force feedback channel was replaced with an environment estimation

- force prediction methodology. The estimator, an EWRLS algorithm, recursively estimates the environment parameters of a given force model from the slave position, velocity, and force. The predictor then used the estimated environment parameters along with the master kinematics to deliver a level of force feedback appropriate to the operator.

A metric for teleoperator transparency was established as the *prediction error*; defined as the error between the measured environment force and predicted master force for a given position. Due to the master and the slave rarely occupying the space space inside the environment simultaneously, a search algorithm is included that finds the closest prior master position to the current slave position. Prediction error is then listed as the difference in force at these two points.

Additionally, *estimation error* was defined as a metric for the estimator performance. Estimation error is the difference between the measured slave force, and the estimated force found via the estimated parameters and the slave kinematics.

Experiments were conducted to determine the effectiveness of the EWRLS algorithm in estimating the environment parameters. A computer-generated sinusoidal trajectory was used to drive the movement of the slave end-effector inside a polyurethane foam. The estimation process was found to be particularly sensitive to the choice and level of filtering present on the slave position, velocity, and force signals. Inconsistent delay induced by filtering each of these signals resulted in unrealistic and potentially unstable parameter estimation, including the damping coefficient converging to a negative value.

Chapter 5

Experimental Verification of Predictive Force Feedback

In this chapter, experimental validation of the *estimation - prediction* force feedback methodology is presented for the full teleoperated system. Human-in-the-loop palpation tasks with a polyurethane foam are conducted and evaluated for teleoperation transparency. A variety of force feedback methodologies are investigated for comparison; direct force feedback, a spring-based adaptor, as well as two virtual environments based on the Kelvin-Voight and Hunt-Crossley force models. The experimental results presented support the use of a virtual environment for transparent teleoperation, in particular for the Hunt-Crossley force model.

5.1 Human-in-the-Loop Teleoperation

Human-in-the-Loop teleoperation refers to the inclusion of a human operator into the control structure, with position information originating from, and force feedback being sent to, the human operator. It effectively completes the feedback loop of the bilateral controller, and issues of transparency and stability become important. The following experiments provide an indication of how effective the estimation-prediction controller is at providing teleoperation transparency.

5.1.1 Experimental Set-up and Procedure

Experimental procedure was consistent throughout all the tests performed in this section. Firstly, the surgical slave (controlled via the user-operated master) was gradually pressed perpendicularly into the foam until an environment force of approximately 2.9N was observed. From there, the slave was oscillated up and down while in contact with the foam for several tens of seconds, until fully retracted from the material. In addition to being rendered physically on the Phantom Omni stylus, the haptic feedback force was monitored graphically in the GUI for any anomalies, and to ensure that both the master and the slave remained in contact with the respective real and virtual environments. This procedure was repeated for three trials of varying length and teleoperation motion styles. A picture of the full teleoperated system is shown in Figure 5.1.



Figure 5.1: Full teleoperated system, featuring surgical robot (slave), haptic pen (master), and control computer.

Initial values were kept constant for each experiment, and are the same as those used in Section 4.3, except for λ , which has been lowered to quicken the estimation process. These values are listed again in Table 5.1.

Table 5.1: Initial values for the estimation algorithm. Values are reset at the beginning of each experiment. It must be noted that the Kelvin-Voight model does not use parameter n .

Parameter	Initial Value
<i>Environment Parameters</i>	
K	0.5 N mm^{-1}
B	0.01 N s mm^{-1}
n	2.00
<i>EWRLS Algorithm</i>	
\mathbf{P}_0	\mathbf{I}
λ	0.995

Experiments were conducted using:

- Direct force feedback from the slave to the master;
- A spring-based adaptor acting between the slave and master;
- Virtual environments from the EWRLS estimation-prediction methodology, with both the Kelvin-Voight and Hunt-Crossley force models.

5.1.2 Direct Force Feedback

To begin, the force-indentation results for the direct force feedback methodology is presented. In this experiment, the controller is altered such that at time-step k ,

$$F_m[k] = F_s[k]. \quad (5.1)$$

The Butterworth filter cut-off frequency was set to 3 Hz on the F_e signal to reduce unwanted noise in the force-feedback signal, $F_m[k]$. No other signals were filtered. Although the cut-off frequency used here is lower than that used in subsequent experiments (5 Hz), the additional induced delay is not expected to cause any significant adverse effects. Referencing Figure 4.5, with a 3 Hz cut-off frequency, the filter will delay a 1 Hz signal by approximately 9.6 samples, or 48 ms, whereas a 5 Hz cut-off frequency will add a delay of 6.1 samples, or 30 ms. In comparison, the position-forward delay time,

caused by the relatively slow response time of the robot, is estimated to be between 200 – 400 ms, and contributes significantly more delay between the master and slave subsystems.

Issues relating to filter delay detailed in Section 4.3.2 are not applicable to this experiment, as the EWRLS estimation algorithm is not utilised.

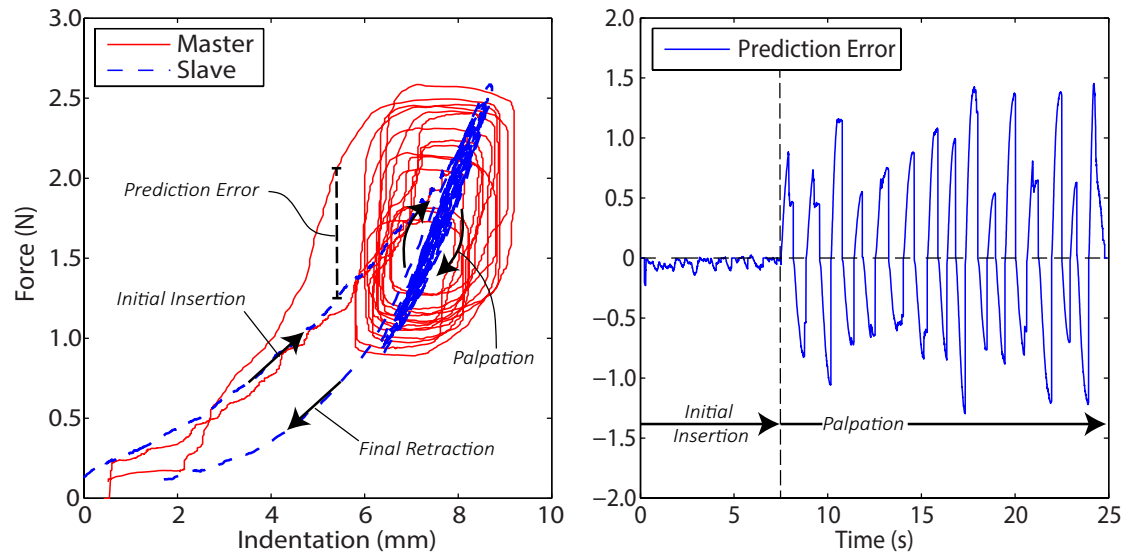


Figure 5.2: (Left) Force profiles for both the slave and master as the slave interacts with a polyurethane foam. (Right) Error between the master and slave forces for a given slave position. The time index refers to the slave time-step. Annotations have been added to highlight specific aspects of the force-indentation profile.

Figure 5.2 (left) compares the slave-environment force with the master-feedback force as the slave interacts with the polyurethane foam. Figure 5.2 (right) shows the prediction error between the slave and master. Here, time is in reference to the slave time-step, and error is the error between slave and master forces for the slave position at the given time. While in this case, it is not strictly a “prediction error”, as no prediction has occurred, it is labelled as such due to it being calculated in the manner detailed above in Section 4.2.2.

Annotations have been included to highlight various areas of interest in the force-indentation profile. Distinct components are the *initial insertion*, *palpation*, and *retraction* phases. Additionally, the *prediction error* is graphically defined as the error between the master and slave for a given position.

Of note is the force profile observed during the initial insertion. It was found that the environment force was larger and more linear during the initial insertion than the subsequent palpation and retraction phases. Once palpation starts, the environment force drops off sharply, and non-linearity increases.

It is theorized that this is caused by the air contained within the foam being expelled during the initial compression. Once palpation begins, and the compressive force is relieved, air has to be drawn back into the foam for restitution to occur. This action is driven by the relatively weak internal stresses of the foam, and takes a comparably longer time. What results is a larger environment force during the initial compression, and a lower, non-linear force-profile during palpation and retraction.

The prediction error, Figure 5.2 (right), demonstrates how poor direct force feedback can be at providing transparent teleoperation. During the initial insertion (0 – 7.5 s), the prediction error is minimal and acceptable. However, as soon as palpation begins, the prediction error becomes substantial and ranges between ± 1.5 N.

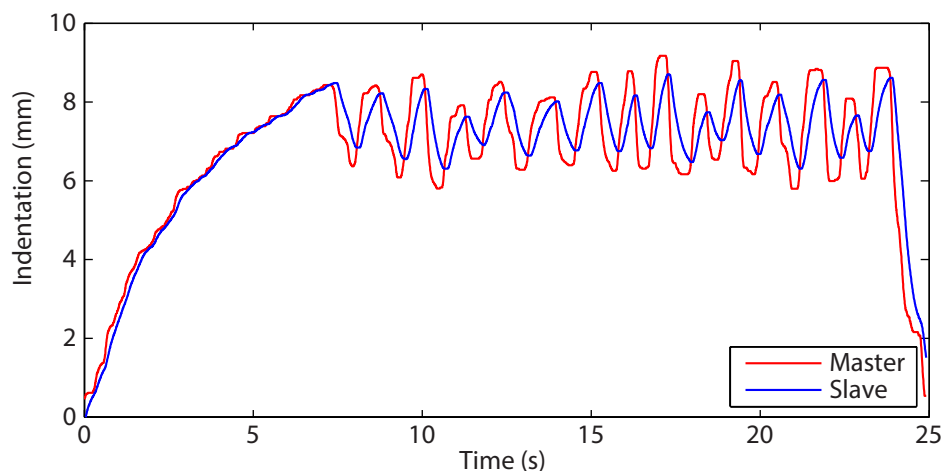


Figure 5.3: Position profiles for both the slave and master, as the slave interacts with the polyurathane foam.

Figure 5.3 offers an explanation as to where this error originates. During palpation (from approximately 7.5 s onwards), the slave loses position tracking cohesion with the master. The master can be seen to lead the slave considerably as the system is manipulated against the environment. Force feedback, originating in this experiment *directly* from the measured slave force, is intrinsically tied to the slave position. When

there is substantial offset between the slave and master positions, poor transparency follows.

During teleoperation, a distinct feeling of delay could be felt as the environment was manipulated. In Figure 5.2 (left), this perceived delay is seen in the vertical paths of the master force-indentation profile. To illustrate, say that the slave is in steady contact with the foam and, via the direct feedback channel, the master is experiencing the same feedback force. Now, the master is quickly moved upwards so its position is outside the environment boundary (i.e. $x_m < 0$). The master position has decreased, but the slave has not yet reacted to the new position command. Feedback force remains relatively constant, and the user will experience a force even though the master is no longer in contact with the virtual environment. Only once the slave responds with a similar movement is the feedback force decreased. For palpation or oscillatory-like motion, this is seen as a circulatory force-indentation profile.

The root-mean-squared error (RMSE) and motion characteristics during palpation for the three trials is given in Table 5.2. Prediction error during the initial insertion has been excluded from the calculations because (a) the error is small during this phase, (b) the error during this phase does not give an indication of teleoperation performance, and (c) the length of time taken to reach full insertion differs considerably across each trial.

Table 5.2: RMSE and motion characteristics during palpation using a direct force feedback methodology. Asterisk (*) indicates presented experimental results.

	Trial 1(*)	Trial 2	Trial 3
Prediction RMSE	0.694 N	0.571 N	0.560 N
RMS Speed of Motion	3.9 mm s ⁻¹	4.2 mm s ⁻¹	4.0 mm s ⁻¹
Max. Environmental Force	2.58 N	3.12 N	2.91 N

The variation in RMSE seen across each trial is due to different styles of hand motions used while controlling the system. For example, in trial 1 the palpation strokes were generally shorter and of higher frequency than trials 2 and 3, resulting in more sudden changes in direction and larger error.

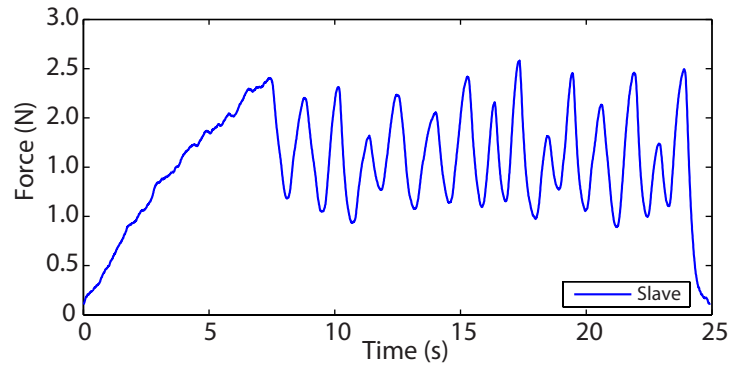


Figure 5.4: Force profile for the slave during insertion into a polyurethane foam. The force profile for the master is identical to that of the slave.

Finally, the force profile for the environment force is shown in Figure 5.4. As the environment force and feedback force are the same for each time-step, only the slave-environment force is shown.

5.1.3 Spring Based Adaptor

The spring-based adaptor implemented into this teleoperated system in [80] places a spring *between* the master and the slave to adapt the feedback force. This is what has previously been referred to as a *semi-* or *quasi-direct* feedback methodology, as the underlying force-feedback mechanism is still the environment force, with the spring estimator adapting the final feedback force. Force feedback in this case is given by

$$F_m[k] = F_s[k] + \hat{K}_1[k](x_m[k] - x_s[k]) \quad (5.2)$$

where the spring-adaptor, $\hat{K}_1[k]$ is calculated at each time-step by

$$\hat{K}_1[k] = \left| \frac{F_s[k] - F_{contact}}{x_s[k] - x_{contact}} \right|. \quad (5.3)$$

Equation (5.3) calculates the average stiffness given the slave's current penetration into the environment ($x_s - x_{contact}$) and the difference in force ($F_s[k] - F_{contact}$).

During this experiment, a low-pass filter was used in the calculation of \hat{K} to smooth the noise within the slave force and position signals. Similarly, a cut-off frequency of 3 Hz was applied to the slave force signal F_s . A maximum value of 0.5 N m^{-1} for \hat{K}

was also specified, due to the inaccuracy of the adaptor (5.3) when indentation is small ($|x_s - x_{contact}| \ll 1$).

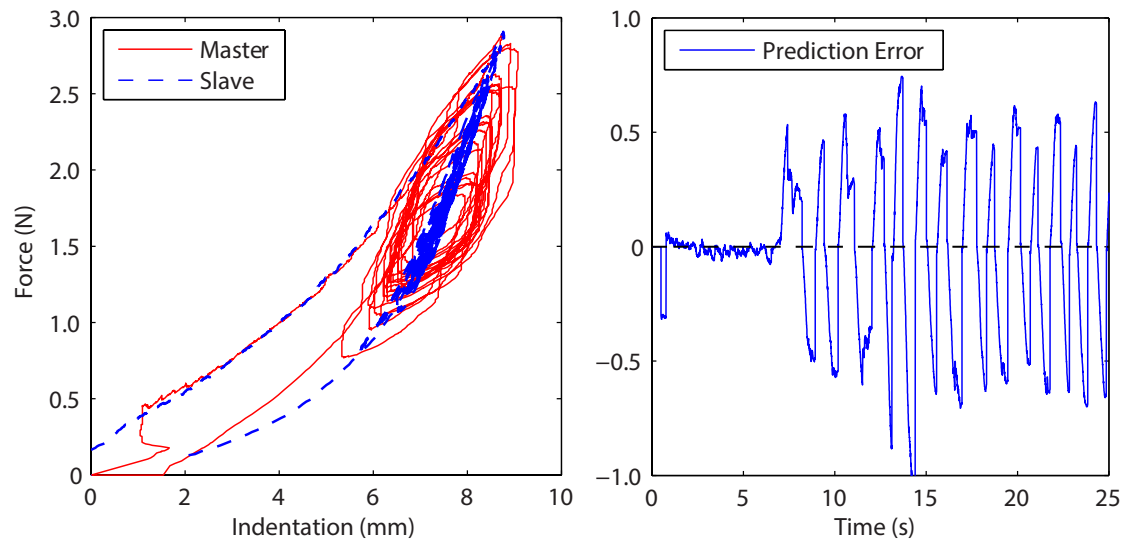


Figure 5.5: (Left) Force-indentation profile using the original spring-based adaptor to moderate the feedback force to the master. (Right) Prediction error during palpation.

Figure 5.5 (left) shows the force-indentation profile for the slave and the master, where the spring-based adaptor is used to moderate the feedback force. The adaptor introduces a restoring force to the master, which acts to pull the master feedback force towards the slave-environment force. As the adaptor takes into account the master position, feedback force is no longer directly tied to the slave dynamics. Instead, the feedback force is adapted to the environment properties and the master's own kinematics.

Figure 5.5 (right) shows the prediction error between the master feedback force and the measured slave-environment force. Similar to Figure 5.2 (right), error is minimal during the initial insertion (0 – 7 s), but grows once palpation begins.

Prediction RMSE for each trial of this experiment is given below in Table 5.3, along with the RMS speed of the robot and maximum environmental force. Again, the error during the initial insertion is excluded from both the RMSE and motion characteristics for consistent comparison between trials. These values are a noticeable improvement over the direct-force feedback methodology.

Table 5.3: RMSE and motion characteristics during palpation using the spring-based adaptor. Asterisks (*) denotes presented data.

	Trial 1(*)	Trial 2	Trial 3
Prediction RMSE	0.427 N	0.452 N	0.392 N
RMS Speed of Motion	3.1 mm s ⁻¹	4.2 mm s ⁻¹	3.1 mm s ⁻¹
Max. Environmental Force	2.9 N	2.8 N	2.7 N

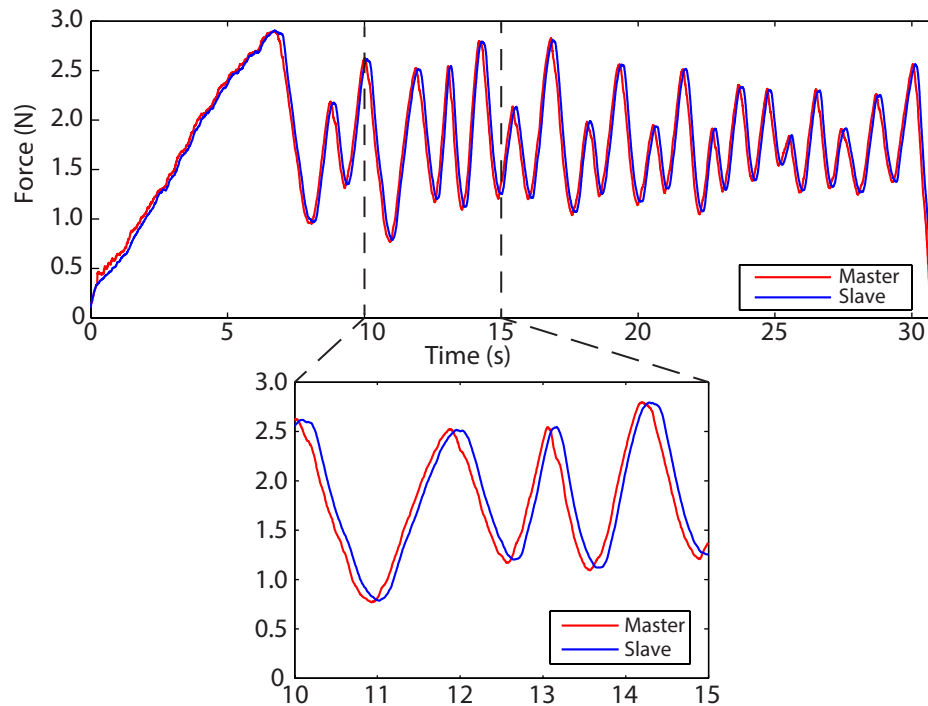
**Figure 5.6: Force-time profiles of the slave and master, using the original spring-based adaptor, with a section highlighting the adaptor acting on the master feedback force.**

Figure 5.6 demonstrates the restoring force acting on the master, effectively preempting the changes in force feedback required by the master's own kinematics. The highlighted section in Figure 5.6 shows clearly that the force feedback now leads (and predicts) the slave-environment force.

Considering that during teleoperation the master similarly leads the slave in position (Figure 5.7), this effect is greatly desired and improves both the stability and telepresence of the surgical system.

By connecting the master to the slave via a virtual spring, a restoring force is introduced which is dependent on the master's kinematics, as well as the contact environment properties. This restoring force noticeably improves teleoperator transparency.

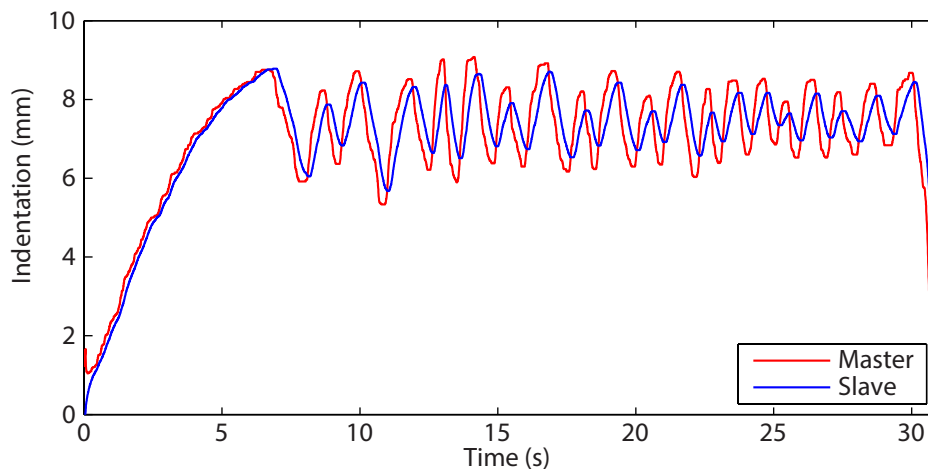


Figure 5.7: Position-time profiles for the slave and the master, using the original spring-based adaptor, as the system interacts with a polyurethane foam.

5.1.4 Kelvin-Voight Model

Moving to an entirely *virtual* feedback mechanism involves the use of a more robust estimator, in this case the EWRLS algorithm detailed above in Section 4.1.2. With this estimator, more complex linear models can be used as the basis for the virtual environment. Here, we present a spring-damper based virtual environment; the Kelvin-Voight force model.

With the Kelvin-Voight model, force feedback is driven according to the following relationship.

$$\mathbf{F}_m[k] = \begin{cases} \hat{K}_{KV}\mathbf{x}_m[k] + \hat{B}_{KV}\dot{\mathbf{x}}_m[k], & \mathbf{x}_m[k] \geq 0 \\ 0 & \mathbf{x}_m[k] < 0. \end{cases} \quad (5.4)$$

The environment parameters \hat{K}_{KV} and \hat{B}_{KV} in (5.4) represent, respectively, the estimated environment stiffness and damping coefficients, calculated via the EWRLS algorithm. During this experiment all dynamic signals (position, velocity, and force) were filtered for both the slave and master, at a cut-off frequency of 5 Hz. Initial testing of

the EWRLS algorithm had a static forgetting factor of $\lambda = 0.995$, which was found to have a good compromise between parameter stability and parameter convergence time.

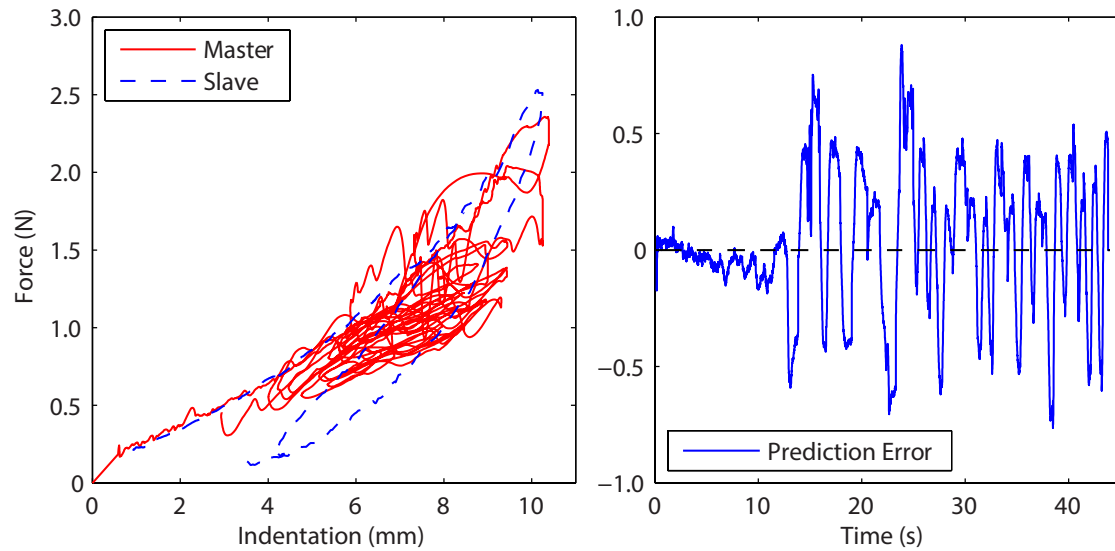


Figure 5.8: (Left) Force-indentation profile using the Kelvin-Voigt force model as the virtual environment. Note that only the slave force outer envelope is presented for clarity. (Right) The master prediction error.

Figure 5.8 (left) shows the position-force profile for the measured slave-environment force and the predicted master feedback force. For the purpose of clarity, only the outer envelope of the slave force profile is shown. The full form of the slave position-force profile is similar to that in Figure 5.5.

Figure 5.8 (left) demonstrates graphically that the Kelvin-Voigt model performs poorly when estimating a non-linear environment such as the polyurethane foam. The Kelvin-Voigt model, being a linear model, is unable to capture the non-linear behaviour of the foam. This is indicated by the overall linear profile of the master feedback force. During teleoperation, the estimated parameters K_{KV} and B_{KV} were unable to converge and settle to a satisfactory constant value. Instead, the parameters would vary with each movement of the slave mechanism. This variation is a direct result of the linear Kelvin-Voigt model attempting to capture the materials restitution, hysteresis, and non-linear effects. The culmination of this is a non-constant, potentially unstable, virtual environment.

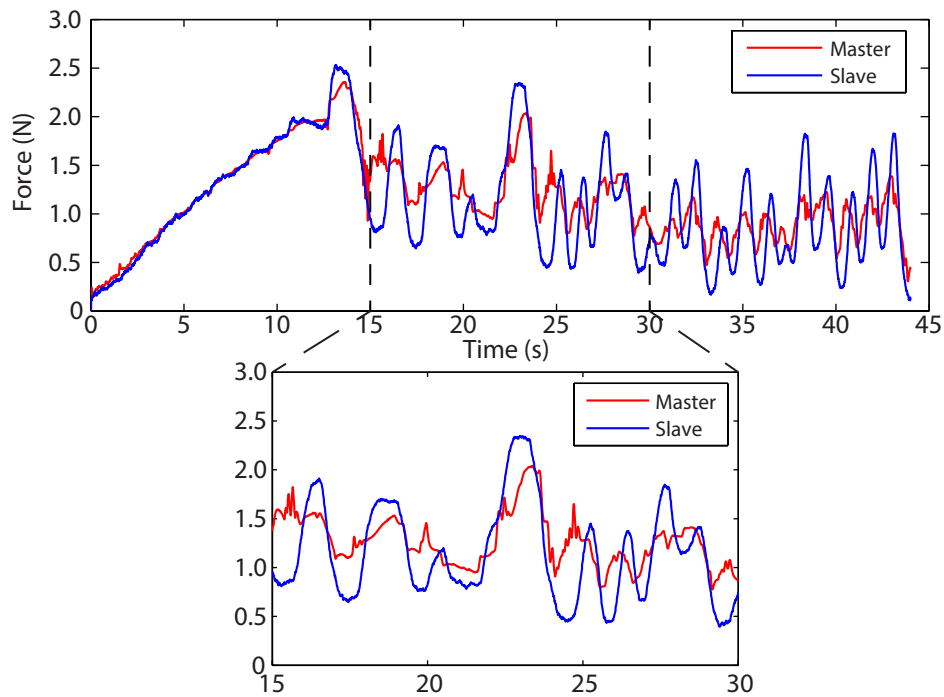


Figure 5.9: Force-time profile using the Kelvin-Voight force model as the virtual environment. The highlighted section demonstrates the how the master feedback force inconsistently follows the slave environment force.

Prediction error seen in Figure 5.8 (right) demonstrates similarly inconsistent performance. When compared to prediction errors for the direct and spring-based methodologies, the virtual Kelvin-Voight model is more unpredictable and has greater localised variations, with several instances of high frequency error (≈ 5 Hz). Further, Figure 5.9 shows that the predicted feedback force no longer faithfully pre-empt the slave-environment force.

While the above performance issues can be attributed to the non-constant and unstable virtual environment, there are also additional contributing forces that degrade teleoperation performance. The damping coefficient, B_{KV} , was observed to vary noticeably, even becoming negative for portions of the experiment. A negative damping coefficient leads to potentially severely unstable behaviour. This large variation of the damping coefficient, combined with the jagged nature of the PHANToM Omni velocity signal, creates a particularly non-smooth damping force, as per Figure 5.10.

Prediction, estimation, and optimal RMSE for each of the three trials is presented in Table 5.4. Again, all values calculated are for the palpation phase of the teleoperation.

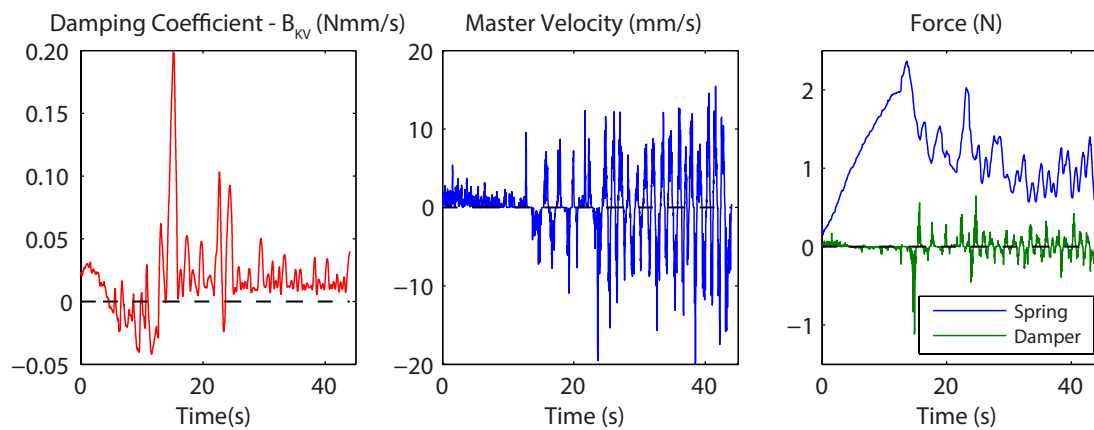


Figure 5.10: Damping coefficient and master velocity when using the Kelvin-Voigt environment model. Note how in the force profile the damping force has several sharp peaks and troughs.

In addition, information regarding the movement speed and range is given, with the aim of providing insight to the varied teleoperation performance.

Table 5.4: RMSE and mean prediction error during palpation using the Kelvin-Voigt virtual environment. Asterisks denote presented experimental data.

	Trial 1(*)	Trial 2	Trial 3
<i>Estimated Parameters</i>			
Prediction RMSE	0.356 N	0.628 N	0.606 N
Estimation RMSE	0.262 N	0.448 N	0.399 N
RMS Speed of Motion	3.9 mm s ⁻¹	5.6 mm s ⁻¹	3.9 mm s ⁻¹
Max. Environmental Force	2.5 N	3.3 N	3.4 N
<i>Optimal Solution</i>			
Optimal RMSE	0.349 N	0.480 N	0.458 N
R²	0.603	0.618	0.568

The variation seen in the RMSE values above can be attributed to the different speed and range of motions used during each trial, a consequence of human-controlled teleoperation. Trial 2 had the highest average speed of motion (5.6 mm s⁻¹) and subsequently the greatest RMSE (and poorest teleoperation transparency). For comparison, the average speed of both trial 1 and 3 was 3.9 mm s⁻¹.

Trial 1, which has the lowest RMSE of the three trials, had a more restricted motion range compared to the subsequent trials. The maximum environment force recorded

for this trial was 2.51 N. Trial 2 and 3, on the other hand, had maximums of 3.31 N and 3.40 N, respectively. The Kelvin-Voight estimator, being a non-linear model, is less effective over larger ranges of motion, as the polyurethane foam's non-linearity becomes more pronounced. As such, the Kelvin-Voight model is more accurate during trial 1, as evident by the considerably lower RMSE.

The optimal solution follows a similar trend in RMSE, with trial 1 yielding the lowest overall error. Interestingly, the RMSE of the optimal solution is greater than the estimation RMSE. The optimal parameters are single values applied to the entire data-set, calculated off-line. On the other hand, the estimated parameters are dynamic, varying as new data is received. They are able to follow, to a certain extent, the environments non-linearity and dynamic properties such as hysteresis, restitution, and, for the polyurethane foam particularly, fluid dynamics of the encapsulated air. With the forgetting factor set to $\lambda = 0.995$, enough variability is given to the estimated parameters so that these dynamic properties are partially captured.

Overall, the virtual Kelvin-Voight model demonstrates worse transparency for the polyurethane foam than the spring-based adaptor. However, when the motion range is more constricted and slower, as seen in trial 1, transparency is slightly improved.

5.1.5 Hunt-Crossley Model

Unlike the Kelvin-Voight force model, the Hunt-Crossley force model is non-linear, and was developed specifically as a means of modelling contact forces of soft environments. Physical inconsistencies found in linear models, such as energy exchange between tool and environment, and non-zero forces at the boundary, are more intuitively handled with the Hunt-Crossley model. Using the model as a basis, the force feedback at each time-step $[k]$ is calculated according to

$$\mathbf{F}_m[k] = \begin{cases} \hat{K}_{HC}\mathbf{x}_m^{\hat{n}}[k] + \hat{B}_{HC}\mathbf{x}_m^{\hat{n}}[k]\dot{\mathbf{x}}_m[k], & \mathbf{x}_m[k] \geq 0 \\ 0 & \mathbf{x}_m[k] < 0. \end{cases} \quad (5.5)$$

In (5.5), the environment parameters \hat{K}_{HC} and \hat{B}_{HC} represent the spring- and damping-like coefficients, respectively, while \hat{n} is the non-linearity power. As with the previous virtual environment experiment each position, velocity, and force signal was filtered to 5Hz with a first order Butterworth filter. The forgetting factor was again left at a constant $\lambda = 0.995$.

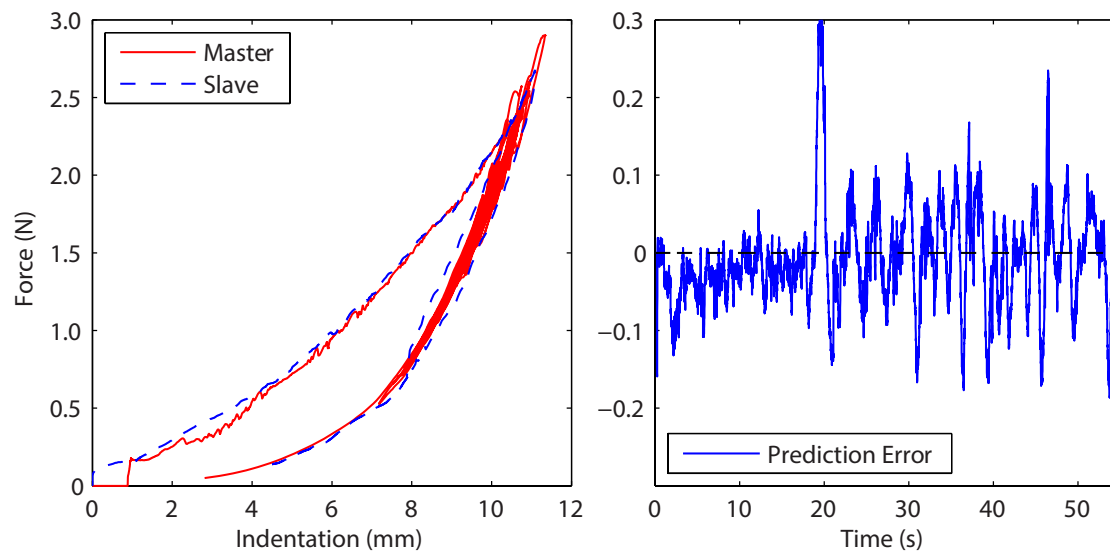


Figure 5.11: (Left) Force-indentation profile using the Hunt-Crossley force model as the virtual environment. Note that only the slave force outer envelope is presented for clarity. (Right) The force-feedback prediction error.

Figure 5.11 (left) demonstrates how powerful the Hunt-Crossley model is at accurately estimating and predicting the environment force. The predicted master force-feedback profile closely matches the measured slave-environment profile. The non-linearity constant n is able to capture the behaviour of the polyurethane foam, and the master force profile is well contained within the slave profile. Additionally, the position-dependent damping term removes the non-zero force at $x(t) = 0$ present in the Kelvin-Voight model and spring-based adaptor. The force, during retraction, gradually decreases to zero as the tool is removed from the environment. Qualitatively, the Hunt-Crossley model feels remarkably realistic, albeit when compared to the previously examined force-feedback methods.

Figure 5.11 (right) shows how the prediction error remains remarkably low during the experiment, ranging for the most part between ± 0.15 N. There is a major peak at

approximately 20 s, which was the time at which the slave end-effector motion changed from inserting to palpating.

Prediction, estimation, and optimal RMSE for the three trials are given below in Table 5.5. RMS motion speed and maximum environmental force is also included. As with the previous experiments, the values cover the palpation phase of motion.

Table 5.5: Prediction, estimation, and optimal RMSE during palpation using the Hunt-Crossley virtual environment. Asterisks denote presented experimental data.

	Trial 1(*)	Trial 2	Trial 3
	<i>Estimated Parameters</i>		
Prediction RMSE	0.076 N	0.115 N	0.103 N
Estimation RMSE	0.034 N	0.032 N	0.054 N
Mean Speed of Motion	2.3 mm s ⁻¹	2.4 mm s ⁻¹	3.9 mm s ⁻¹
Max. Environmental Force	2.69 N	2.30 N	2.48 N
	<i>Optimal Solution</i>		
Optimal RMSE	0.052 N	0.098 N	0.115 N
R²	0.986	0.939	0.944

Prediction RMSE was notably low and consistent across each trial. Trial 2 had the highest prediction RMSE at 0.115 N, and trial 1 had the lowest at 0.076 N, indicating that the Hunt-Crossley model is capable of predicting the environment to a high degree of accuracy.

Estimation RMSE was also extremely low for each trial, indicating that the EWRLS algorithm performs very well with the linearly approximated Hunt-Crossley force model and given environment. Similar to the Kelvin-Voigt model, the RMSE of the optimal parameters is greater than that of the estimated parameters RMSE, indicating that the variability of parameters within the EWRLS algorithm is an advantage.

Figure 5.12 demonstrates the Hunt-Crossley virtual environment anticipating the feedback force with the kinematics of the master, effectively causing the master feedback force to lead the slave-environment force. Of note is the presence of slight oscillations in the master force, as seen in the highlighted section of Figure 5.12. These

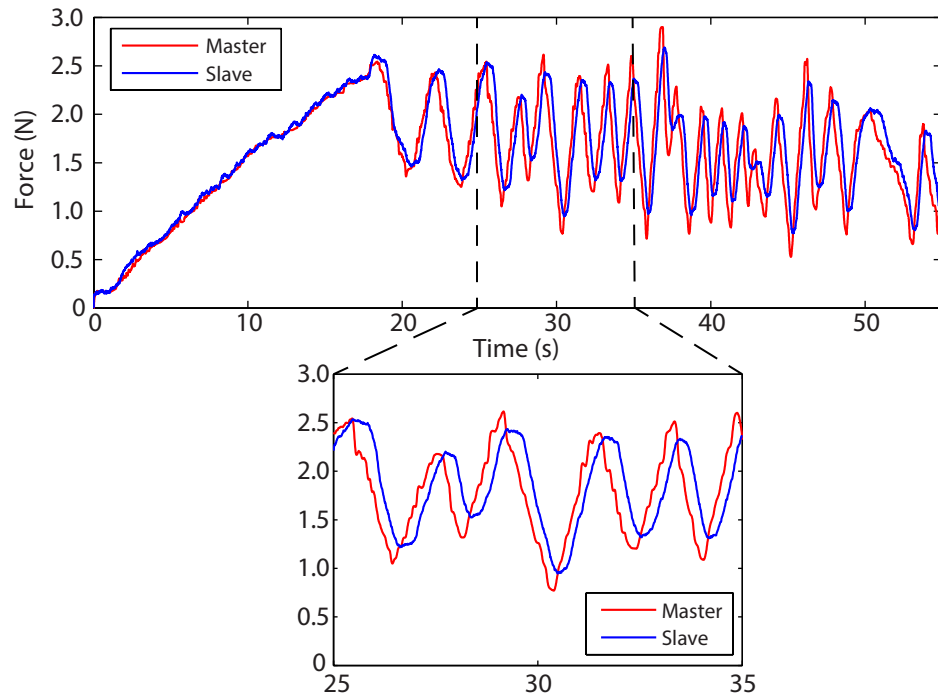


Figure 5.12: Force-time profile using the Hunt-Crossley force model as the virtual environment. The highlighted section demonstrates the Hunt-Crossley model’s ability to accurately pre-empt the feedback force.

oscillations were presented to the user as slightly varying resistive forces in the Phantom Omni as it was moved through the virtual environment. These oscillations are likely caused by the delay induced in the master force signal by the Butterworth filter.

Qualitatively, during this experiment, the force response at the master felt natural and realistic. The high level of transparency allowed for a greater sense of control over the teleoperated system, even with the positional delay between master and slave. The fact that the master’s own kinematics was driving the force-feedback meant that hand movements immediately resulted in a change in force. Maintaining the slave-environment interaction to below 3 N was significantly easier than the previous force-feedback methods, as seen by the relatively consistent maximum force across each trial in Table 5.5.

5.2 Summary

In this chapter, the proposed estimation-predictive bilateral controller was experimentally verified for overall teleoperator performance. Human-in-the-loop experiments

were conducted, where a polyurethane foam was palpated by the slave and force feedback provided to the operator via a variety of methodologies. Teleoperator performance was evaluated by analysing the prediction error, the results of which are presented in Figure 5.13.

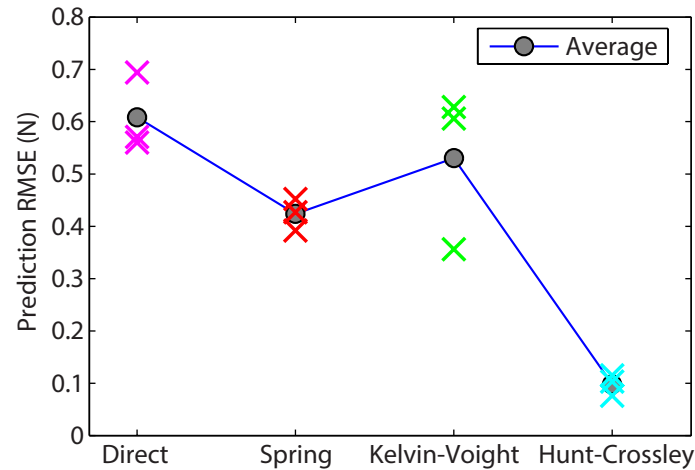


Figure 5.13: Prediction RMSE for each of the force feedback methodologies tested

An on-line EWRLS algorithm recursively estimates the environment parameters of a given force model from the slave position, velocity, and force. The estimated environment parameters are then combined with the master kinematics to deliver a level of force feedback appropriate to the operator. The estimation-prediction methodology compensates for the time-delay present between the slave and master subsystems, and provides increased transparency to the user.

Results presented in Figure 5.13 demonstrated that the Hunt-Crossley force model was able to provide greatly improved transparency when compared to the three other force-feedback methods, having an average prediction RMSE error of 0.10 N. Using the Kelvin-Voight force model exhibited potentially improved performance (trial 1), but also demonstrated notable inconsistency between individual trials. The spring-based adaptor was more consistent, but had a higher prediction RMSE of 0.43 N. Using a direct force feedback methodology resulted in considerable prediction error, with an average RMSE of 0.60 N.

Chapter 6

Estimator Adaptability

This chapter details the development of an adaptive estimator into the estimation - prediction controller, with the goal of increasing the controller's overall adaptability, transparency, and stability, particularly when in contact with changing environments. Contained within the exponentially weighted recursive least squares (EWRLS) algorithm is a forgetting factor, λ , which dictates how quickly the estimation process adapts to a changed environment. Initially, a range of static forgetting factors were investigated for their effect on environment parameter estimation, with input motion is driven by a sinusoidal trajectory. Consequently, the range of acceptable forgetting factors is selected for use in an adaptor. The adaptor moderates the forgetting factor via the estimation error, with the goal of increasing estimation speed during times of high error, and slowing down the estimator when error is low. Experimental validation was conducted across a range of both adaptive and static forgetting factors for Human-in-the-loop teleoperation.

6.1 Development of an Adaptive Forgetting Factor

Static, homogeneous, or consistent environments are rarely encountered in a biological setting. Force feedback, and by extension bilateral controllers, aimed at such environments must be able to maintain teleoperation performance under a wide variety of conditions. For instance, the surgical tool may pass through multiple layers of tissue,

with varying levels of stiffness, tensile strength, and non-linear characteristics. Bone or calcified deposits may be encountered, surrounded by softer muscle or fat. Tissue may need to be palpated to locate and diagnose cancerous lumps or growths. A bilateral controller's ability to accurately adapt to these different environments plays a significant role in the effectiveness of haptic feedback in surgical robotics.

By design, an adaptation mechanism is intrinsically embedded within the EWRLS estimation algorithm via the forgetting factor, labelled as λ in (4.5). Ostensibly, the forgetting factor dictates the relative weight older data has on the estimation process. A forgetting factor of $\lambda = 1$ results in all data points having equal weight, as per the standard RLS algorithm. When $\lambda < 1$, older data points contribute to the updated parameters less. In practicality, the forgetting factor primarily affects the covariance matrix \mathbf{P}_k in (4.5) of the EWRLS update equations by *increasing* the variance and covariance of the environment parameters each time step. Increasing the (co)variance of the environment parameters enables a higher level of variability in each progressive estimation.

This mechanism is useful, particularly if the estimated parameters are inaccurate either due to a lack of persistency of excitation, or because the environment is inconsistent or changing. Reducing λ , and thus increasing \mathbf{P}_k , provides the estimation process with greater capacity to converge to desired parameter values.

However, reducing λ , and increasing variability, can cause significant stability issues if used unsupervised. For example, if the underlying force model is a poor representation of the environment, then the estimated parameters will always be inaccurate, regardless of the variance granted to the estimation process. The EWRLS algorithm will continually try to compensate for the ill fitting model by constantly varying the parameters, obstructing the estimated parameters from converging, and resulting in an unstable virtual environment. Further, if λ is *too* low, then \mathbf{P}_k can grow unbounded and cause significant instabilities from floating point errors. Generally, literature describes a lower limit of $0.98 < \lambda$ for this reason.

6.1.1 Parameter Estimation Behaviour with a Static Forgetting Factor

The range of forgetting factors which are acceptable in terms of stability and convergence is dependent on a number of factors, such as the force model used, and how well the model describes the environment. As seen in Chapter 4, the Hunt-Crossley force model is able to accurately model the environment contact force of a polyurethane foam; a static, non-linear environment.

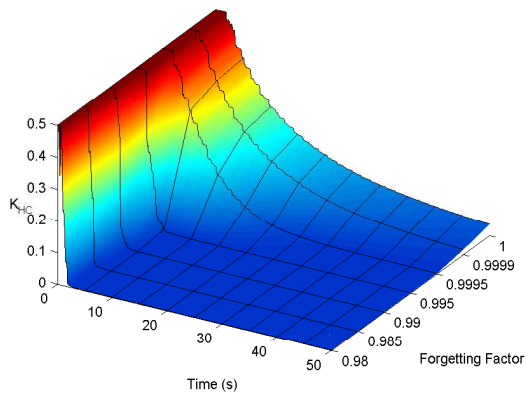
In this section, parameter estimation is investigated for a wide range of forgetting factors, with the goal of identifying an acceptable range of forgetting factors, and under what circumstances this range should apply.

Again, the underlying force models used are the Kelvin-Voight and Hunt-Crossley models. A sinusoidal trajectory (6.1) is used to drive the surgical slave to contact and palpate the polyurethane foam. As in Section 4.3.2, no force feedback is provided, as only parameter estimation (and not force prediction) is under investigation. While palpating the foam, the force, position, and velocity data are recorded, and later passed through an off-line EWRLS algorithm. A variety of forgetting factors, given in Table 6.1, are used.

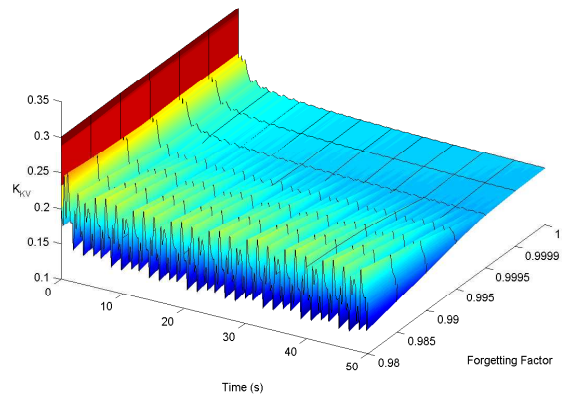
$$x(t) = x_0 + 1.2\sin(2\pi 0.6t) + 2.3\sin(2\pi 1.5t) + 1.6\sin(2\pi 2.4t). \quad (6.1)$$

Table 6.1: Range of forgetting factors, and the relative speed of parameter estimation.

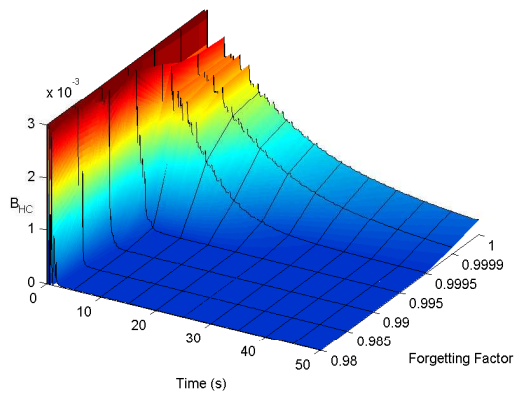
	Fast	←—————→					Slow
Forgetting Factor	0.98	0.985	0.99	0.995	0.9995	0.9999	1.0000



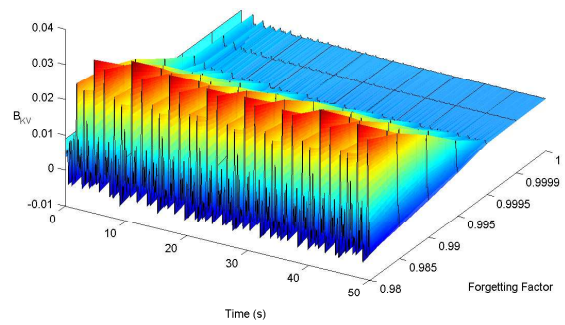
(a) Estimation of K_{HC} .



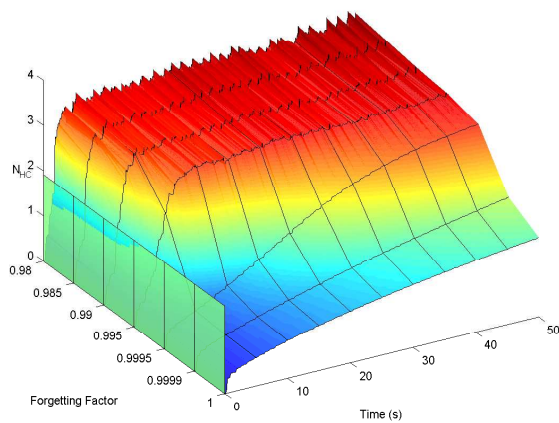
(b) Estimation of K_{KV} .



(c) Estimation of B_{HC} .



(d) Estimation of B_{KV} .



(e) Estimation of N_{HC} .

Figure 6.1: Estimated environment parameters across a range of forgetting factors.

Estimating Parameters with a Static Forgetting Factor

Figure 6.1 shows how the estimated parameters evolve over time for different values of λ . Time is plotted along the x -axis, and forgetting factor (λ) along the y -axis. The estimated environment parameters are shown as height, along the z -axis. The view for each individual surface plot is consistent, except for the non-linearity parameter, n , of the Hunt-Crossley model, shown in Figure 6.1e, where the perspective has been mirrored for clarity. Also, non-linear scaling has been used along the λ (y -axis) to clearly (visually) separate the different forgetting factors.

Along the left-hand side are the three Hunt-Crossley parameters, K_{HC} , B_{HC} and n_{HC} (Figure 6.1a, c, and e, respectively). Along the right-hand side are the two Kelvin-Voight parameters, K_{KV} and B_{KV} (Figure 6.1b, and d, respectively).

Of particular note is the difference in estimation behaviour observed between the two models when under a faster estimation process ($0.980 \leq \lambda \leq 0.995$). The Hunt-Crossley parameters converge quickly, with a sharp transition occurring within seconds of environment contact.

The Kelvin-Voight parameters, on the other hand, fail to converge to a steady state value, instead oscillating in line with the input motion. This parameter non-convergence (Figure 6.1b, and d) for $\lambda < 0.995$ causes significant instabilities when used during teleoperation; the virtual environment, which the haptic master interacts with, is by extension unstable and unpredictable, resulting in extremely poor system stability and transparency.

When the EWRLS algorithm is slower ($\lambda > 0.995$) parameter estimation behaves markedly different between the two force models. The Hunt-Crossley model, with three parameters to estimate, fails to fully converge within the ≈ 1 min time-frame of the experiment. The presence of an additional parameter dramatically slows down the estimation process. In comparison, the Kelvin-Voight model, with only two parameters to estimate, converges within seconds. Additionally, as the available variance of parameters (P_k) is lower (due to the higher λ value), the oscillations in parameters observed previously when $\lambda < 0.995$ are not present, and the parameters are able to stabilise to

a steady state value. In this case, the slower EWRLS algorithm is preferable for the Kelvin-Voigt model.

This leads to two points of interest:

- If the underlying force model is a good representation of the environment, then a lower value of λ can be confidently used to ensure quick and stable convergence. Conversely, if the force model is a poor representation of the environment, then a lower λ can cause significant instabilities in the virtual environment.
- Stability of the virtual environment can be improved for a poor environmental representation by slowing down, and decreasing the variance, of the EWRLS algorithm.

The overall estimation RMSE of each experiment is compared to the optimal solution RMSE in Figure 6.2. For both force models, faster estimation yields lower RMSE. For the Hunt-Crossley model, the estimated parameters only performs better than the optimal solution when $\lambda = 0.980$. As $\lambda \rightarrow 1$, estimation RMSE increases as the parameters require more time to converge.

For the Kelvin-Voigt model, estimation RMSE behaves similarly, except in this case the optimal solution yields the poorest performance. With only two parameters to estimate, convergence occurs significantly faster, as seen in Figure 6.1. The faster estimator allows the linear Kelvin-Voigt parameters enough variation to compensate for the non-linear environment. The optimal solution, being a singular set of parameters for the entire data-set, do not capture this non-linearity, and thus performs poorly. Although estimation RMSE is lower for the faster estimation speed, this benefit is restricted solely to the slave-environment interaction, and does not necessarily translate to the teleoperator-wide operator-master, slave-environment interaction. As mentioned above, too much variability in parameters causes instability when used as a virtual environment.

The above points highlights a certain nuance of parameter estimation, and the care that must be taken when choosing a force model to represent the environment. A faster estimation process is counter-productive if the underlying force model is intrinsically unable to model the environment. However, increasing the complexity of the force

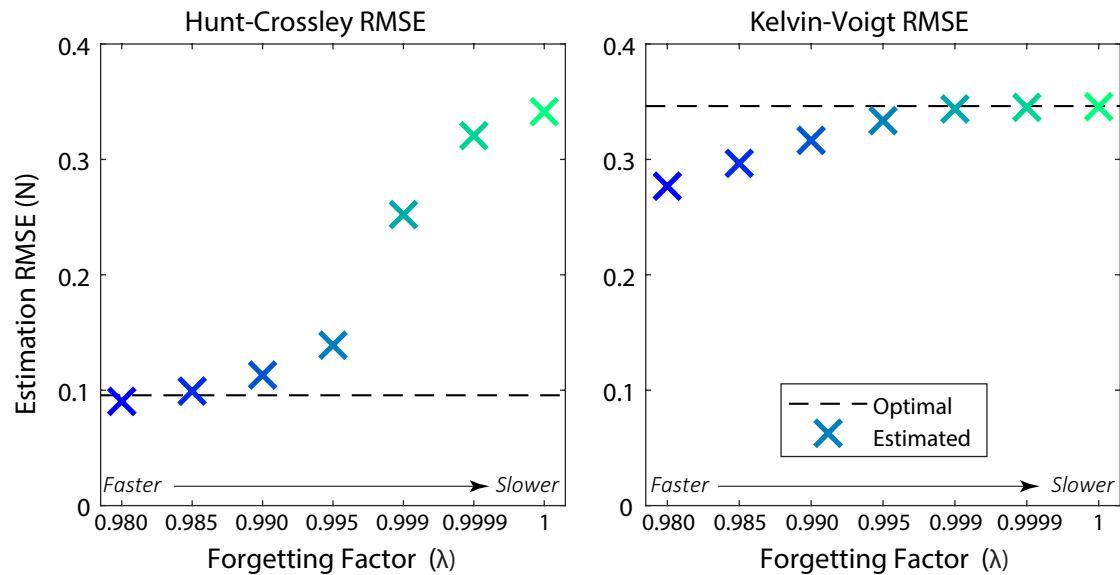


Figure 6.2: Comparison of the estimation RMSE using various forgetting factors with the optimal solution RMSE.

model by adding additional parameters, while potentially improving performance in terms of modelling accuracy, can lead to dramatically increased convergence time.

Thus far, the experimental data has demonstrated that the log-linearised Hunt-Crossley force model is capable of faithfully estimating a non-linear environment, and is able to provide transparent force prediction during teleoperation. The Kelvin-Voigt force model, on the other hand, is unable to accurately capture non-linear effects of the tested environment. An ill-fitting force model can cause significant transparency and stability issues during teleoperation and, as the expected contact environment during surgery is non-linear and non-consistent, the Kelvin-Voigt model is ill suited to the given task. As such, from here onwards, further developments are limited to the Hunt-Crossley force model.

6.1.2 Development of an Adaptive Forgetting Factor

As has been shown in Chapter 4, the Hunt-Crossley force model is capable of accurately representing a non-linear environment; namely a polyurethane foam. In Figure 6.1, parameter convergence was shown to occur sufficiently quickly when $\lambda < 0.995$. When $\lambda > 0.995$, convergence time is sacrificed in favour of decreased variance in parameters (P_k), and subsequent increased parameter estimation stability. From here on, further

developments are concentrated around improving the estimation process for the Hunt-Crossley force model.

Ideally, the environment estimation algorithm should be able to quickly converge and stabilise to the true environment parameters, while maintaining the potential to adapt quickly if the environment changes. From the previous experiments, lowering the forgetting factor to between $0.980 < \lambda < 0.995$ results in quick convergence, while $0.995 < \lambda < 1$ generally results in slow and stable parameter estimation. To be an effective teleoperation technique, the EWRLS algorithm needs to be able to dynamically adapt the estimation speed based on whether or not the estimation-prediction process is accurately representing the environment.

This can be achieved by linking the forgetting factor value to the estimation error. During times when error is high, such as when transitioning between different environments, the forgetting factor should be lowered, thus increasing estimation speed. Once the error has sufficiently decreased, then the forgetting factor can be raised to stabilise the estimated parameters.

A Model for the Forgetting Factor Adaptor

The proposed adaptive methodology uses the arctangent function to adjust the forgetting factor based on estimation error. The arctangent, or $\tan^{-1}(x)$, function is appealing as it features two horizontal asymptotes, and a smooth transition between the upper and lower values.

The full form of the inverse tangent function can be expressed by:

$$\lambda(e)[k] = a_1 \tan^{-1}(a_2(|e_{est}[k]| - a_3)) + a_4. \quad (6.2)$$

In (6.2), $\lambda[k]$ is the forgetting factor at time-step k , and is calculated from the estimation error, $e_{est}[k]$. The coefficients a_1 and a_2 represent scaling factors in the λ and e axes respectively, while a_3 and a_4 shift the function along the e and λ axes, respectively.

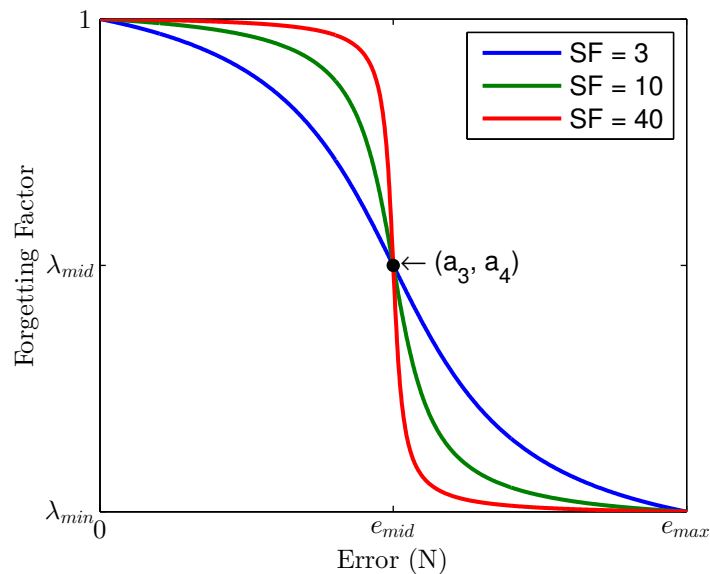


Figure 6.3: Profile of forgetting factor λ adaptor, based on the estimation error e .

By setting a limit on the minimum and maximum values of λ and e , and ensuring that the function is well defined across the entire range, then values for a_3 and a_4 can be expressed as

$$a_3 = \frac{e_{max} + e_{min}}{2} \quad \text{and} \quad a_4 = \frac{\lambda_{max} + \lambda_{min}}{2}. \quad (6.3)$$

From Figure 6.3, obvious choices are $\lambda_{max} = 1$ and $e_{min} = 0$. These values ensure $\lambda(0) = 1$ and $\lambda(e_{max}) = \lambda_{min}$.

The coefficient a_2 is a scaling factor along the e axis, and can be interpreted as the adaptors steepness; that is, increasing a_2 causes a sharper transition between the upper and lower values of λ , separating the forgetting factor into two clear segments.

Substituting (6.3) into (6.2), along with the above values of $\lambda_{max} = 1$, $e_{min} = 0$, and the point $\lambda(0) = 1$, yields

$$1 = a_1 \tan^{-1} \left(-\frac{a_2 e_{max}}{2} \right) + \frac{1 + \lambda_{min}}{2}. \quad (6.4)$$

Rearranging (6.4) for a_1 , and defining SF as the *steepness factor* gives

$$a_2 = \frac{2SF}{e_{max}} \quad (6.5)$$

and

$$a_1 = -\frac{1 - \lambda_{min}}{2 \tan^{-1}(SF)}. \quad (6.6)$$

Equations (6.5) and (6.6) defines the forgetting factor with three user-specified values: λ_{min} , e_{max} and SF . From Figure 6.1.1, $\lambda_{min} = 0.985$ is an acceptable choice for the lower bound of the forgetting factor, as it offers good compromise between estimation speed and covariance boundedness. e_{max} is dependent on the overall performance of the force estimation-prediction process, and is investigated in the following section. SF is similarly an application specific value. All together, the complete function to determine the forgetting factor is written as

$$\lambda(e) = -\frac{1 - \lambda_{min}}{2 \tan^{-1}(SF)} \tan^{-1} \left(\frac{2SF}{e_{max}} \left(|e| - \frac{e_{max}}{2} \right) \right) + \frac{1 + \lambda_{min}}{2}, \quad (6.7)$$

for

$$0.985 \leq \lambda \leq 1. \quad (6.8)$$

The developed bilateral controller, incorporating the forgetting factor adaptor, is shown in Figure 6.4.

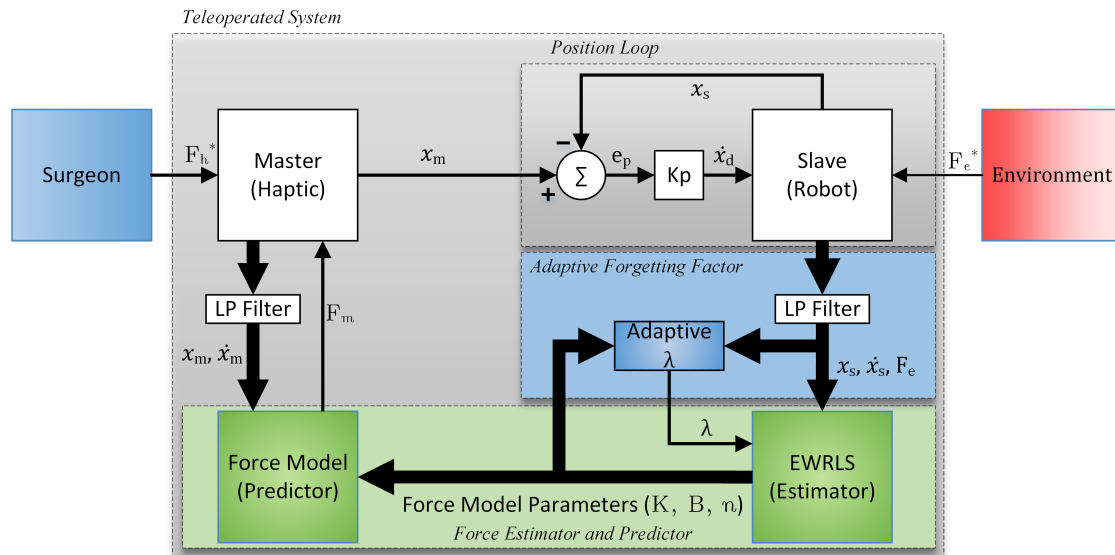


Figure 6.4: The hitherto developed control scheme. In blue is the forgetting factor adaptor, which uses the estimation error to dynamically determine a adjust value of the forgetting factor.

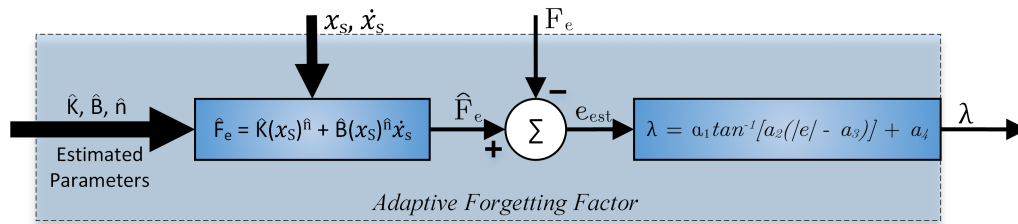


Figure 6.5: The expanded forgetting factor adaptor.

There are several changes between the prior control scheme presented in Figure 4.3 and the developed controller in Figure 6.4. Most notable is the integration of the adaptive forgetting factor, highlighted in blue, which utilises the function given in (6.7) to constantly adapt the EWRLS forgetting factor according to the estimation error. The expanded forgetting factor adaptor is illustrated in Figure 6.5. Estimated values (environment parameters, force) are designated with a circumflex diacritic ($\hat{\cdot}$).

Additionally, the low-pass filter on the master-side has been restricted to only the position and velocity signals (x_m and \dot{x}_m). While conducting the previous experiments, it was found that filtering (and thus delaying) both the input (position, velocity) and output (force) signals to the virtual environment resulted in a noticeable discrepancy between the hand motions and the force response. As the velocity signal contains the most noise, it was chosen as the most appropriate filtered variable, along with position to maintain signal coherence. The following experiments used a cut-off frequency of 3 Hz for master signals x_m and \dot{x}_m . A cut-off frequency of 10 Hz was applied to the slave signals x_s, \dot{x}_s , and F_s as that was found to offer good noise rejection with minimal delay. Finally, to simplify the diagram, the velocity control loop internal to the slave motor controllers have been excluded, and can be assumed to be encompassed by the Slave (Robot) plant.

6.1.3 Environment Boundary Detection

Accurate environment boundary detection is vital to the estimation-prediction algorithm, as the estimator requires precise knowledge of environment penetration (x_s) to

operate effectively. A simple threshold force (0.1 N) had been applied in previous experiments to detect environment boundary. However, as the slave force signal now has increased noise due to the less aggressive filtering applied, it was found that environment contact was often triggered prematurely.

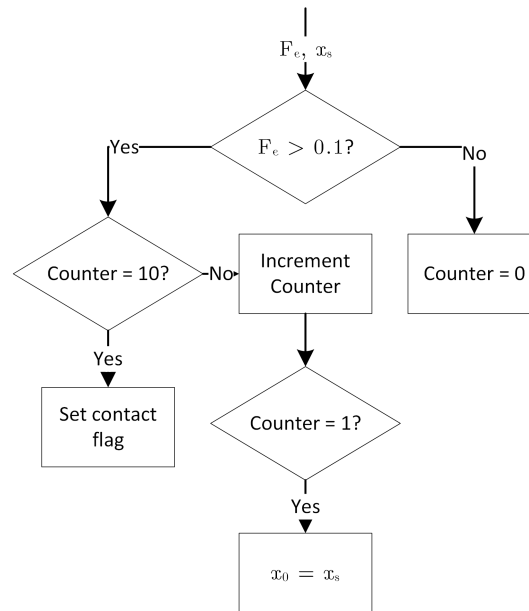


Figure 6.6: Flowchart of the environment boundary detection process, executed every time-step.

For this reason, a threshold counter has been implemented to determine environment boundary more consistently. Contact is now only registered once 10 *consecutive* measurements are above the 0.1 N threshold, with the environment boundary position, x_0 , being assigned to the first instance above the threshold. By including this consecutive counter, individual spurious readings no longer trigger environment contact. The flowchart for this process is illustrated in Figure 6.6.

6.2 Experimental Validation of the Adaptive Forgetting Factor

During a surgical procedure, a surgeon may need to palpate tissue to diagnose and locate potential calcified, tumorous, or anomalous growths. Similarly, making incisions and taking biopsies relies on knowing when the surgical tool has pierced through specific

layers of tissue. If the surgeon is using a haptic-enabled surgical robotic system, then the force feedback methodology needs to be able to distinguish and render this information effectively.

For the developed control system, this involves ensuring the *virtual* environment changes according to, and in line with, the *surgical* environment. The inclusion of an adaptive forgetting factor is aimed at facilitating these changes. To experimentally verify the proposed adaptive controller, a new environment is required.

6.2.1 Experimental Set-up and Procedure

Figure 6.7 is a product designed to simulate soft biological tissues - namely the epidermis, dermis, and subcutaneous tissue. The sample used during this research is the Complex Tissue Model (TSC-10) [81], used by trainee surgeons and medical professionals as a suturing and palpation training aid. The model used in the following experiments is relatively homogeneous across its top layer.

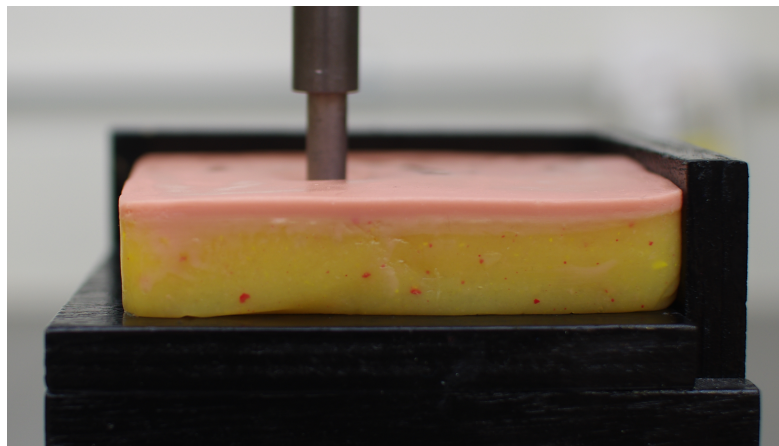


Figure 6.7: Side view of the simulated tissue sample.

The following experiments use the previously discussed polyurethane foam as the initial environment. The surgical slave is inserted slowly into the foam and palpated for several tens of seconds, then fully retracted. The foam is then replaced by the simulated tissue sample, and the process of insertion, palpation, and retraction is repeated. By changing the environment midway through the experiment, the adaptive estimators ability to converge and stabilise to a new environment can be studied.

Initial parameters are given in Table 6.2, and are the same as previous experiments. As the forgetting factor is now adaptive, a static λ is no longer applicable, and instead the range of λ is listed.

Table 6.2: Initial and assigned values for the estimation algorithm.

Parameter	Initial Value	Parameter	Assigned Value
<i>Environment Parameters</i>		<i>Cut-off Frequencies</i>	
K	0.5 N mm^{-1}	$\mathbf{x}_m, \dot{\mathbf{x}}_m$	3 Hz
B	0.01 N s mm^{-1}	F_m	No Filtering
n	2.00	$\mathbf{x}_s, \dot{\mathbf{x}}_s, F_s$	10 Hz
<i>EWRLS Algorithm</i>		<i>Adaptor</i>	
P_0	I	SF	10
λ	$0.985 \leq \lambda \leq 1$		

The steepness factor, SF , has been set to $SF = 10$, as it offers a smooth transition between upper and lower λ values. The adaptive forgetting factor function follows the form of Figure 6.8.

Experiments were conducted with $e_{max} = 0.1, 0.2$ and 0.3 N . A static forgetting factor was also used, with values of $\lambda = 0.985, 0.990$ and $\lambda = 0.995$.

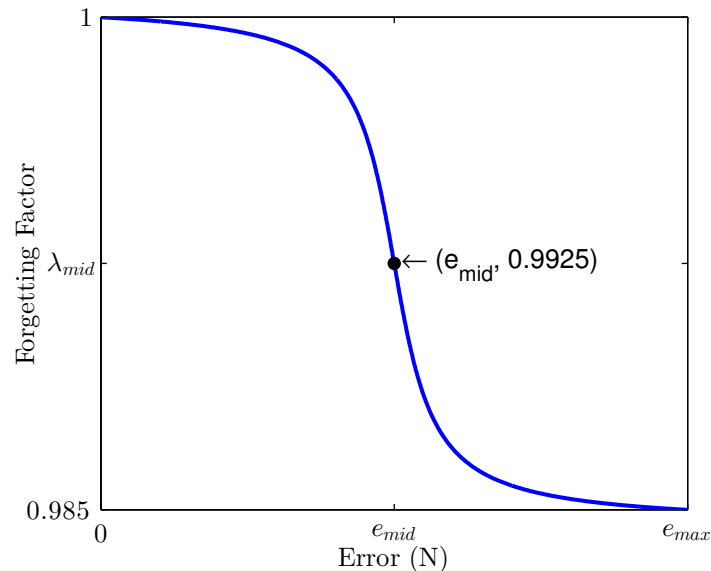


Figure 6.8: Forgetting factor adaptor, where λ is adjusted based on the estimation error $|e|$. The curve has steepness factor $SF = 10$, and $\lambda_{min} = 0.985$. e_{max} is varied for each experiment.

6.2.2 Experimental Results

Adaptive Forgetting Factor

Figure 6.9 shows the force-penetration results for both the polyurethane foam and the simulated tissue, on the left and middle, respectively, with $e_{max} = 0.1$ N and $SF = 10$. On the right are the two profiles superimposed, to better illustrate the difference in force profiles between the two environments. As with similar previous graphs, only the outer envelope of the slave-environment profile is shown for the purpose of visual clarity.

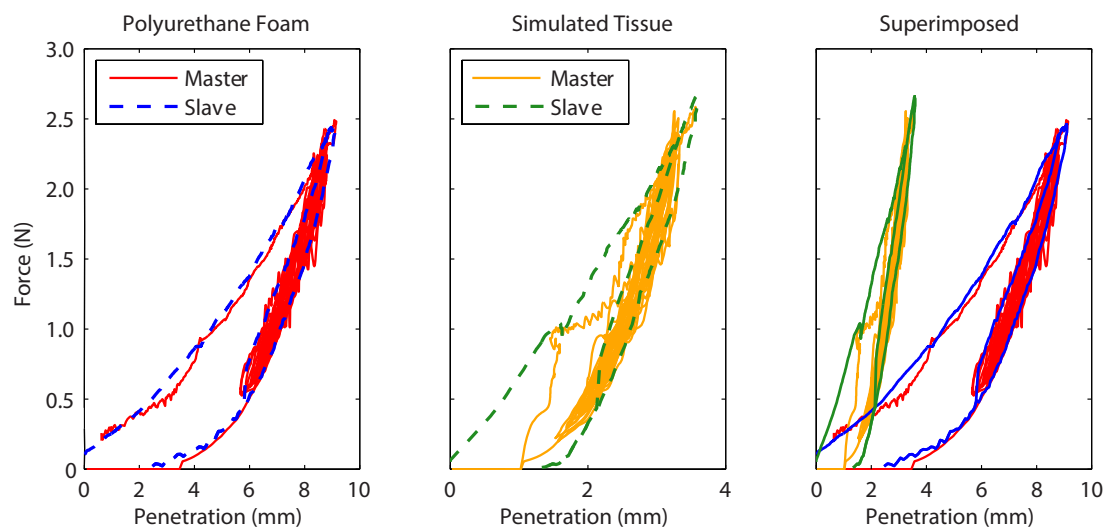


Figure 6.9: The force-penetration profiles for the slave and the master, with $e_{max} = 0.1$ N and $SF = 10$. The contact environments are a polyurethane foam (left), which is then swapped with a simulated tissue (middle) halfway through the experiment. Both force profiles are superimposed (right) to illustrate the difference in environment behaviour.

The profile of the polyurethane foam demonstrates close agreement between the measured and predicted virtual environment. Both the slave and master force profiles fit closely with each other, indicating that the estimated parameters match well with the true parameters. It can be seen that the simulated tissue exhibits a similar trend and agreement between the measured slave and predicted master forces. However, during the initial insertion into the simulated tissue, there was notable variation between the master and slave forces, indicated by the discrepancy between the left outermost paths. This discrepancy is due to the transitional nature of the estimated environment parameters as the new environment is encountered. During the initial contact and insertion,

persistence of excitation is low, and the EWRLS algorithm does not receive enough varied information to faithfully estimate the environment.

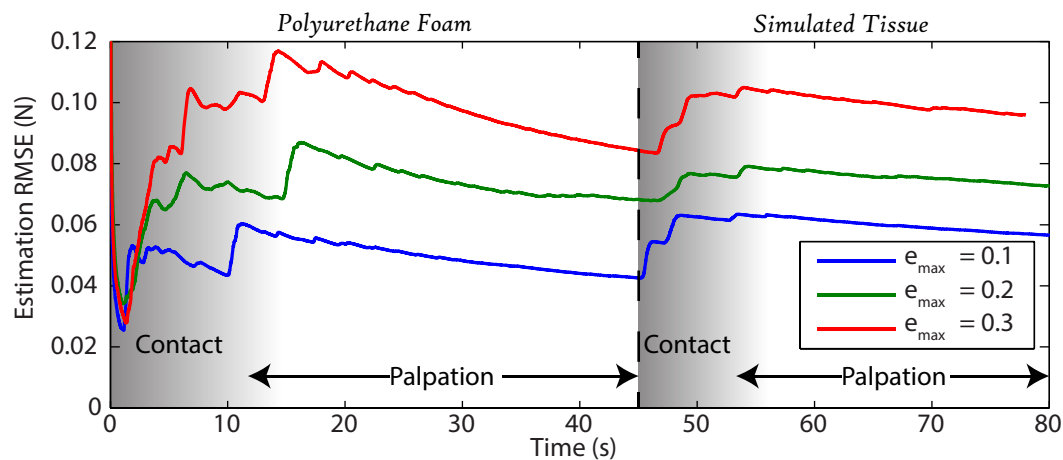


Figure 6.10: Propagation of the environment estimation RMSE as each experiment progressed, using the forgetting factor adaptor. The RMSE for a given time is the calculated RMSE up to that point.

Experiments were conducted for $e_{max} = 0.1, 0.2,$ and 0.3 N. Figure 6.10 shows the evolution of the estimation RMSE as each experiment progressed. It is useful to present the estimation RMSE as a function of time, as it visually demonstrates how well the estimation algorithm evolves over the course of the experiment. In particular, it clearly shows the effect of encountering a new environment, where estimation RMSE rises due to a lack of persistency of excitation. The estimation RMSE lowers once palpation begins, and persistency of excitation increases.

Figure 6.10 shows how placing a tighter limit on e_{max} can greatly improve the estimation performance. By setting e_{max} lower at 0.1 N, the adaptive forgetting factor tends towards faster, more varied estimation during times of higher error. Providing more variance to the estimator allows the parameters to reach more accurate values, quicker, and with eventually less error.

A similar trend can be seen in Figure 6.11, which shows the average estimation RMSE for the preceding 1 s of teleoperation. Figure 6.11 presents a faster snapshot of estimation error, where short-lived trends are more pronounced. Similar to the above, having a lower error range ($e_{max} = 0.1 - 0.2$ N) exhibits lower peak estimation error, and faster settling.

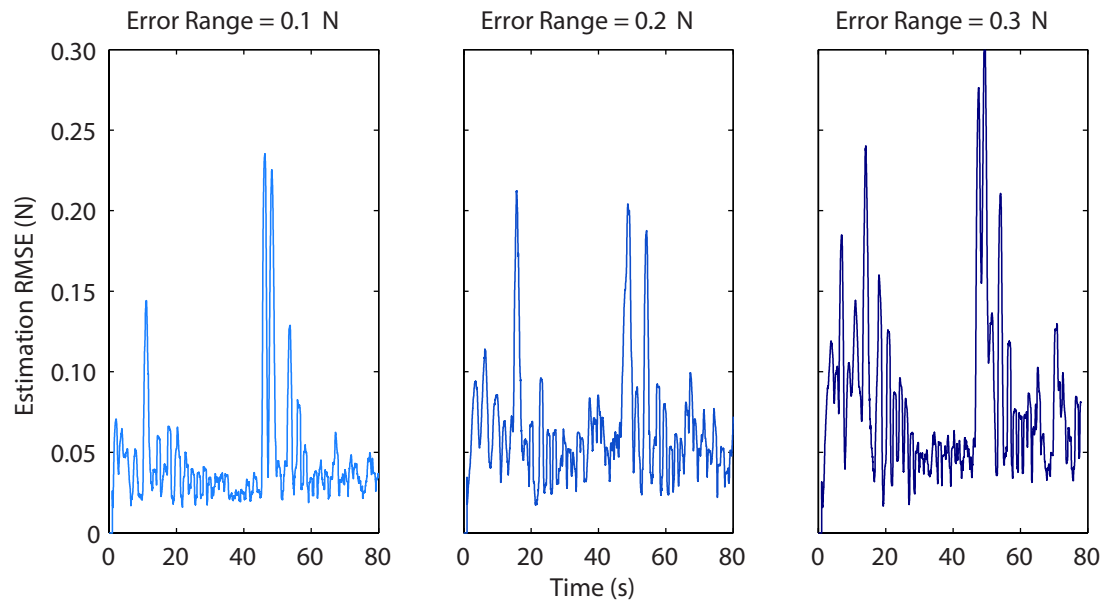


Figure 6.11: Moving window average of the environment estimation RMSE for the previous 1 s, using the forgetting factor adaptor.

With $e_{max} = 0.1$, estimation error reaches lower, and more stable values for both the polyurethane foam ($20\text{ s} < t < 45\text{ s}$) and simulated tissue ($60\text{ s} < t < 80\text{ s}$). The estimation error peaks to 0.23 N when the simulated tissue is introduced, before decreasing substantially.

When $e_{max} = 0.2\text{ N}$, the estimation error peaks slightly lower at 0.20 N when the simulated tissue is introduced. However, estimation error during palpation is higher compared to $e_{max} = 0.1\text{ N}$.

Finally, $e_{max} = 0.3\text{ N}$ has both higher peaks, at 0.31 N , and higher palpation error, as the estimator is essentially unable to vary the parameters sufficiently once $e < 0.15\text{ N}$.

Figure 6.12 restricts the interaction to solely the individual palpation data for each environment, to compare the estimated RMSE with the RMSE of the optimal solution. In each experiment, the estimated parameters outperform the optimal parameters, primarily due to the ability of the estimated parameters to vary with the dynamic effects of the environments. As palpation continues, more air or fluid is expelled out of the palpation region, changing the environment properties. In particular, the optimal parameters for the $e_{max} = 0.2$ experiment in the simulated tissue performs noticeably worse than the estimated parameters. It was found that the palpation region for this experiment

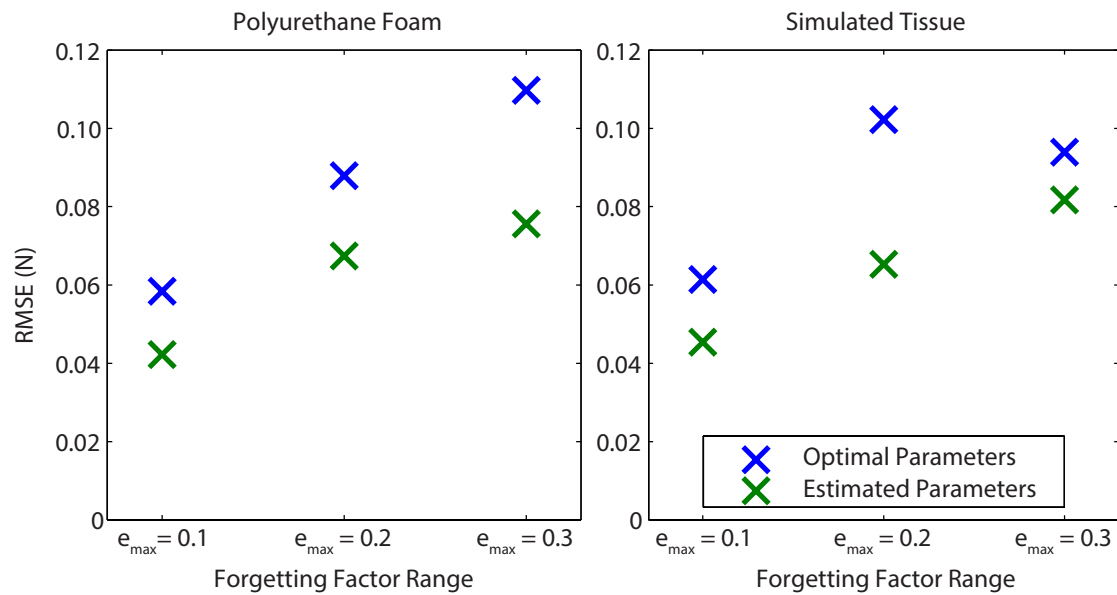


Figure 6.12: Comparison between RMSE of optimal solution and estimated adaptive parameters.

changed gradually from deep to shallow as the experiment progressed. In each other experiment the palpation region was more consistent.

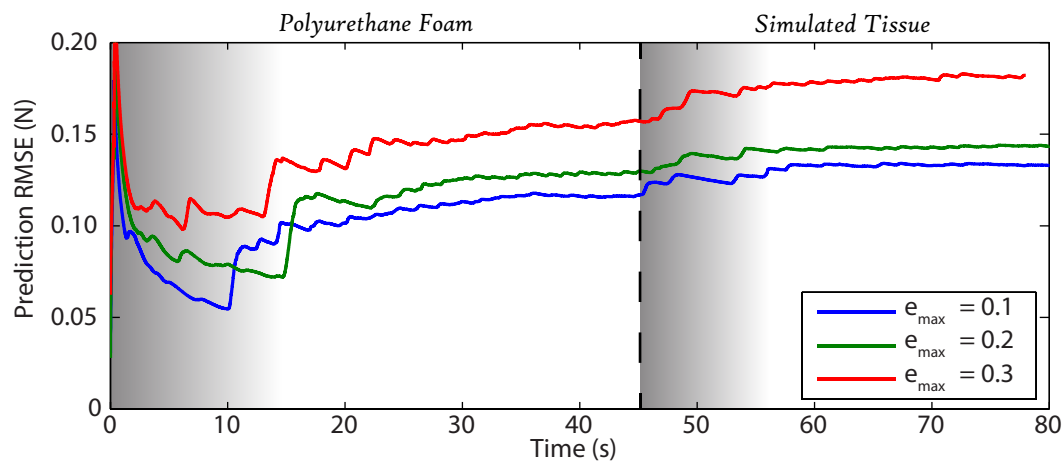


Figure 6.13: Propagation of the prediction RMSE as the experiment progresses, using the forgetting factor adaptor.

Overall teleoperator performance is shown in Figure 6.13, via the prediction RMSE. Similar to Figure 6.10, having a lower error range (e_{max}) translates to improved teleoperator performance. Of note is the tendency of the prediction error to plateau during palpation. Introducing the new environment at approximately 45s causes a small increase in prediction RMSE, similar to, but not as pronounced as, the estimation RMSE.

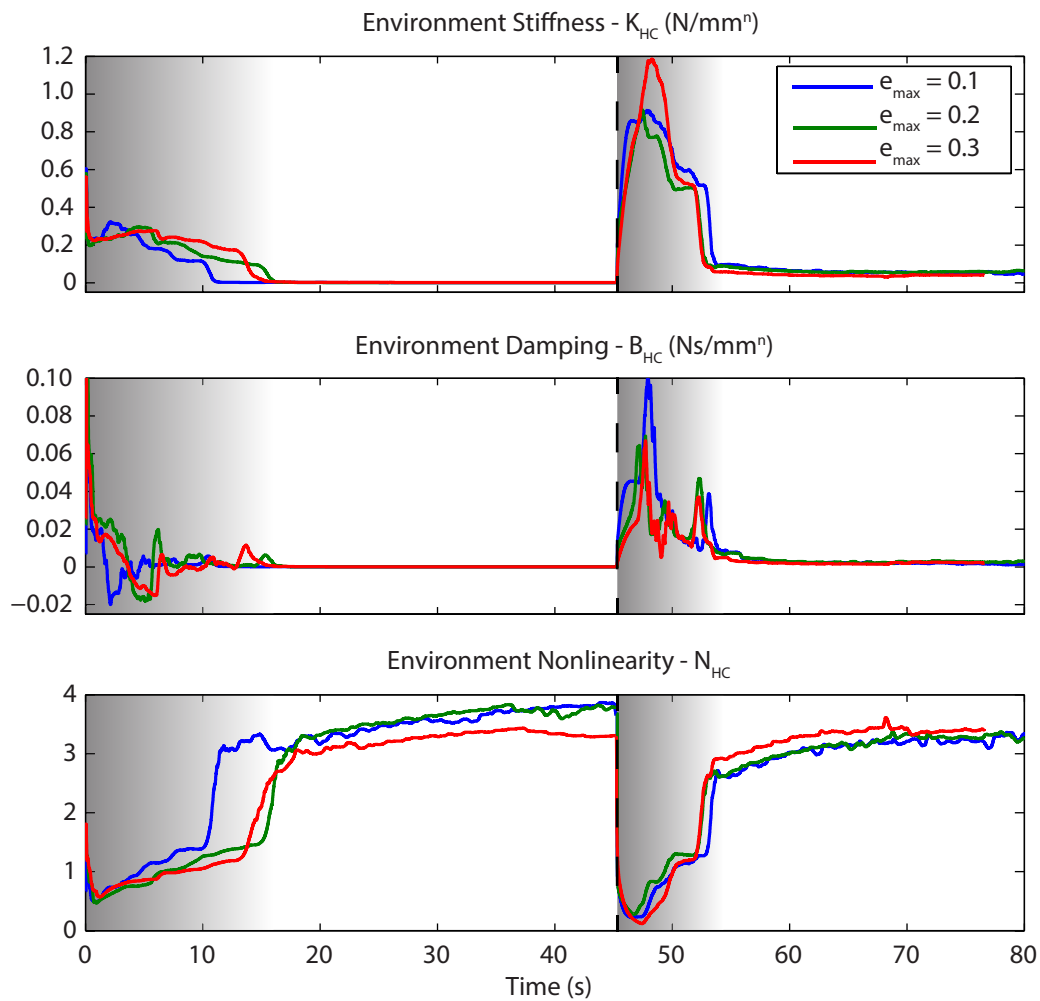


Figure 6.14: Estimated parameters for a polyurethane foam (0 – 45 s) and simulated tissue (45 – 80 s) environment, using the forgetting factor adaptor.

The change of each estimated parameter over time is shown in Figure 6.14. Interestingly, the estimated parameters all appear to converge to similar values at relatively the same rate, regardless of the selected e_{max} . Further, each parameter undergoes significant variation during the initial contact with each environment. This variation is comparatively excessive, and is due primarily to a lack of persistency of excitation while the slave is being inserted in the environment. Although the parameters appear similar across each e width, the above RMSE results indicate that there is a tangible difference in performance between each experiment.

Lastly, Figure 6.15 presents the calculated adaptive forgetting factor as each experiment progressed. As was expected, lowering the transitional error threshold (effectively

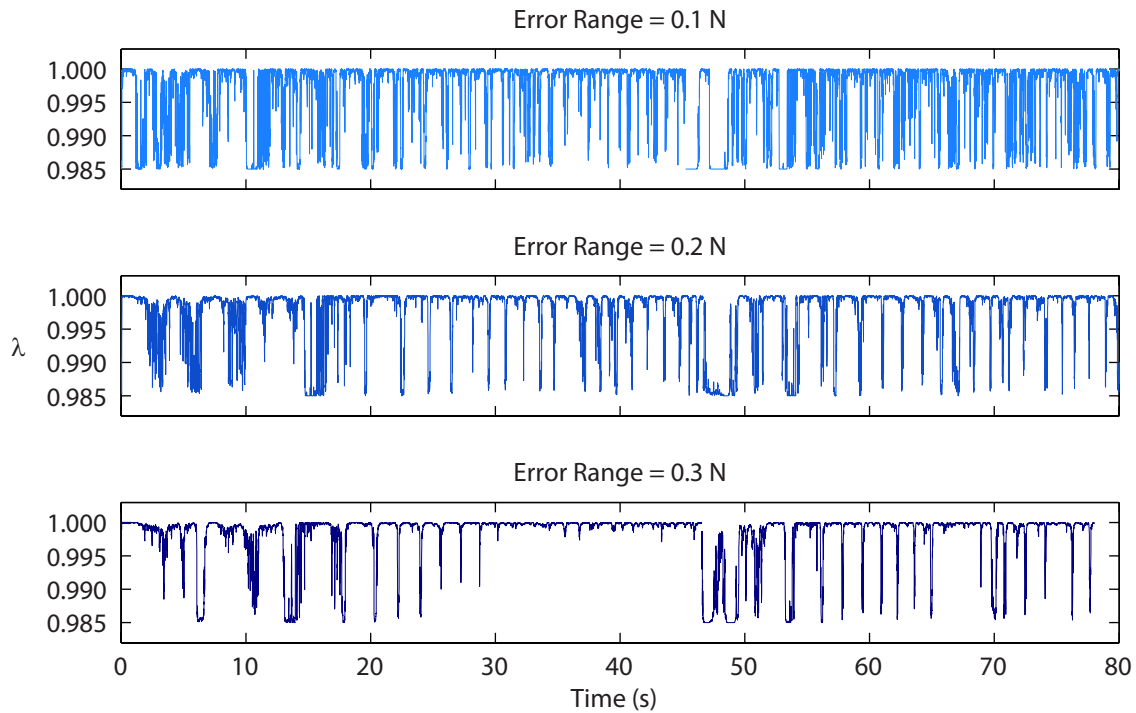


Figure 6.15: Evolution of the forgetting factor (λ) over the three experiments. Increasing the width of the error term (e_{max}) confines the forgetting factor to a higher value, slowing estimation.

$\frac{e_{max}}{2}$) pushes the forgetting factor into the lower, faster region more frequently. Raising the error range confines the forgetting factor to $\lambda \approx 1$ more often.

Static Forgetting Factor

Section 6.2.2 focused on the use of an adaptive forgetting factor, which altered the EWRLS algorithm estimation speed based on the estimation error. As estimation error increased, the λ was lowered, providing more variance to the estimated parameters, which thus allowed the EWRLS algorithm more opportunity to reach potentially better parameter values. Similarly, as the estimated parameters improved, λ was raised to stabilise the estimated parameters, ensuring that the virtual environment (and thus force feedback) remain steady and stable.

A comparative study now needs to be conducted between the above adaptive forgetting factor methodology and the use of a static forgetting factor. Three values of forgetting factor were investigated for comparison; $\lambda = 0.985$ for fast estimation, $\lambda = 0.990$ for medium estimation, and $\lambda = 0.995$ for slower estimation. From Figure 6.1, these

values cover the range of forgetting factors that demonstrated reasonably fast parameter convergence, without additional unwanted parameter variation.

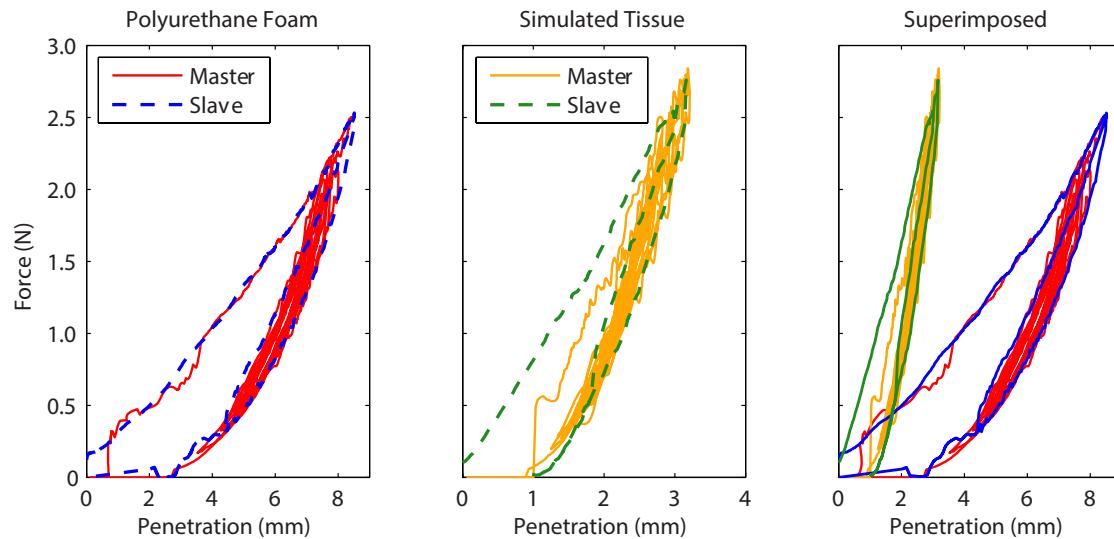


Figure 6.16: Force-penetration profiles for the predicted master, and measured slave force, with $\lambda = 0.990$. The contact environment was changed from the polyurethane foam (left) to a simulated tissue sample (middle) halfway through the experiment. Both force profiles are shown on the right to illustrate the difference in environment behaviour.

Figure 6.16 shows the force-penetration profiles for both the polyurethane foam (left) and simulated tissue (middle), as well as the superimposed profiles (right), using a static forgetting factor of $\lambda = 0.990$. As with Figure 6.9, the polyurethane foam is well represented by the virtual environment. The simulated tissue sample encountered slight under-prediction during the initial insertion phase, as persistency of excitation at this point is low, and the estimated parameters have not adapted fully to the new environment. Although difficult to see, the predicted force in the simulated tissue experiences slight oscillation during palpation. This is a consequence of the static forgetting factor enabling increased parameter variation during palpation, and is explored further below.

The propagation of the estimation RMSE is shown in Figure 6.17. The polyurethane foam is well estimated for both $\lambda = 0.985$ and $\lambda = 0.990$, plateauing to approximately 0.026 N in both cases. $\lambda = 0.995$ performs slightly worse, at 0.045 N.

Once the simulated tissue sample is introduced, all three forgetting factors increase in estimation RMSE, before recovering and decreasing as palpation progresses. $\lambda = 0.985$ recovers relatively quickly, with a final estimation RMSE of 0.04 N. $\lambda = 0.990$

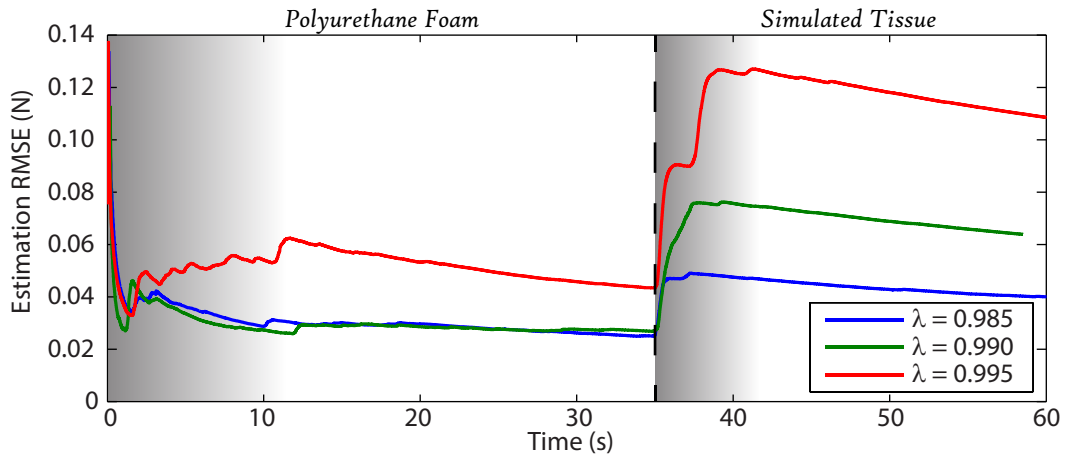


Figure 6.17: Propagation of the environment estimation RMSE as each experiment progressed, using a static forgetting factor.

recovers less effectively, with a final 0.065 N, and $\lambda = 0.995$ is even worse at 0.11 N. All estimation RMSE values are on a downward trend, indicating that the estimator improves with prolonged palpation.

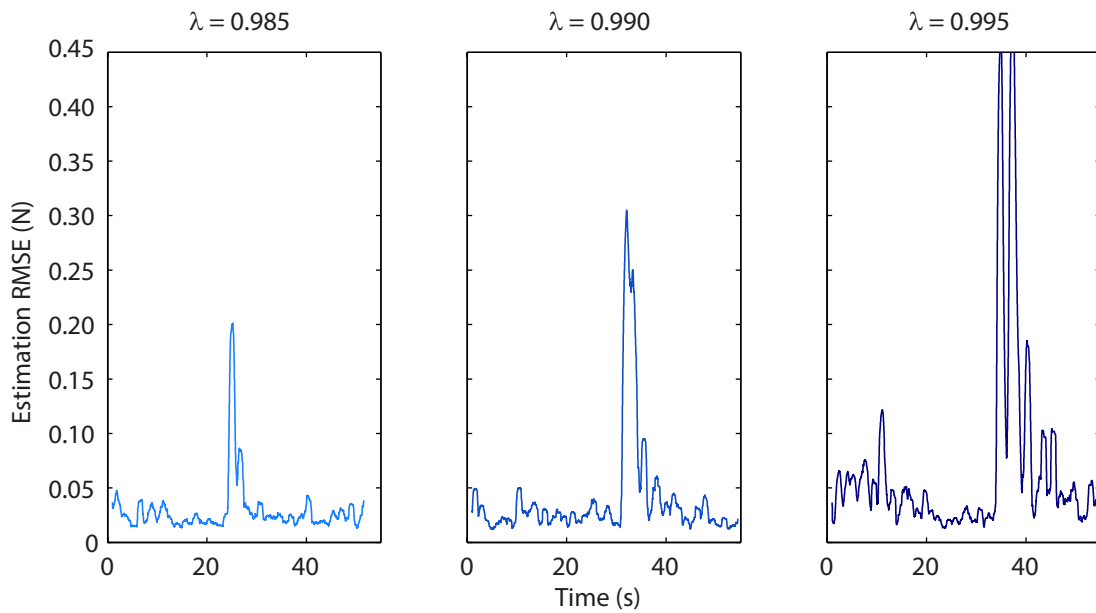


Figure 6.18: Moving window average of the environment estimation RMSE for the previous 1 s, using a static forgetting factor.

A similar trend can be seen in Figure 6.18, which provides a more localised snapshot of the estimation RMSE during each experiment. $\lambda = 0.985$ has remarkably low estimation error during palpation, and is seen to adapt to the new environment quickly,

with a peak error of 0.2 N, which subsides quickly. $\lambda = 0.990$ and $\lambda = 0.995$ experiences higher and greater variation in palpation errors. Similarly, peak estimation error at the introduction of the new environment is higher, at 0.3 N and 0.5 N for $\lambda = 0.990$ and $\lambda = 0.995$, respectively.

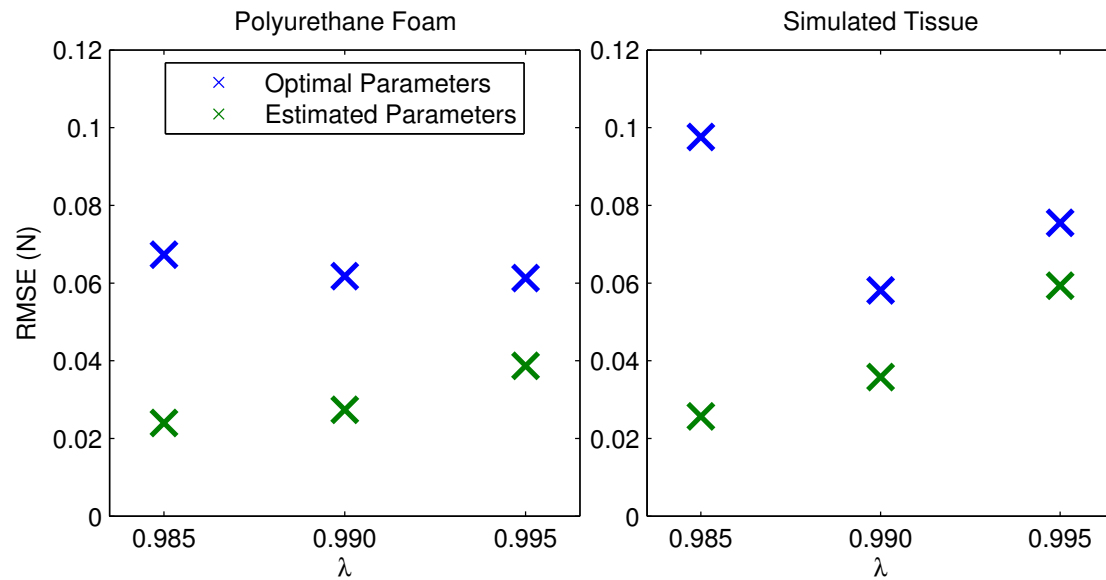


Figure 6.19: Comparison between RMSE of optimal solution and estimated parameters.

In Figure 6.19, the interaction is confined to the palpation data of each experiment, where a comparison can be made between RMSE of the optimal solution and the estimated solution. As seen previously, the estimated parameters performs better than the optimal solution in each experiment. The lowest palpation RMSE is observed with the lowest forgetting factor, due to the greater variability available to the parameters. This adds further evidence to the observation that the environment's behaviour is not constant during palpation. Furthermore, the palpation RMSE of the estimated parameters is lower than those seen in Figure 6.12, again due to the additional variation offered when $0.985 < \lambda < 0.99$. However, lower estimation RMSE, or in this case greater parameter variation, does not necessarily translate to improved transparency, as is explored further below.

The prediction RMSE follows a slightly different trend than the estimation RMSE. Figure 6.20 tracks the prediction RMSE for each forgetting factor, across each experiment. For the polyurethane foam, prediction RMSE is lowest for $\lambda = 0.990$ at 0.1 N,

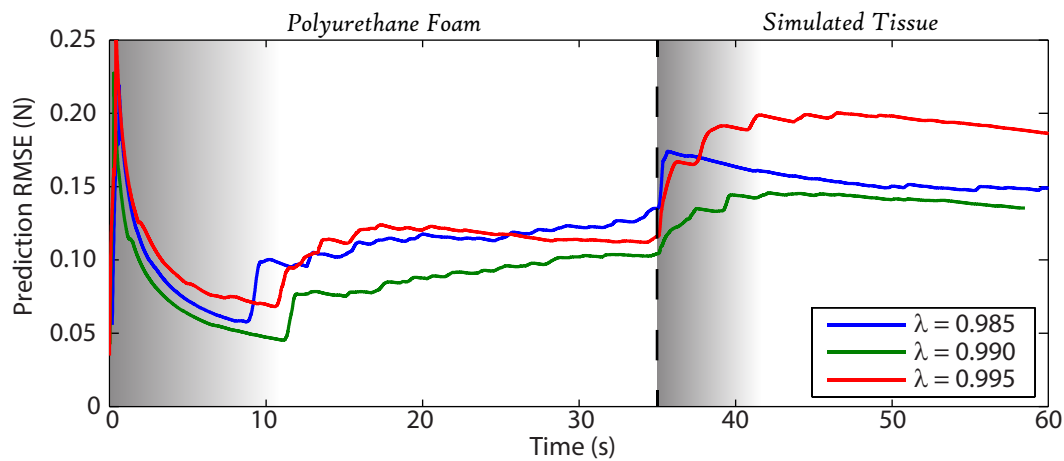


Figure 6.20: Propagation of prediction RMSE as each experiment progressed, using a static forgetting factor.

then $\lambda = 0.995$ at 0.115 N, and finally $\lambda = 0.985$ with 0.135 N. Additionally, both $\lambda = 0.985$ and $\lambda = 0.990$ are trending *upwards* during palpation of the polyurethane foam, indicating that the estimated parameters are not translating well to the virtual environment.

When the simulated tissue sample is introduced at 35 s, prediction errors for all three forgetting factors increases, as expected. As with the polyurethane foam, $\lambda = 0.990$ maintains the lowest prediction error, and becomes steady at approximately 0.135 N. When $\lambda = 0.985$, prediction error experiences a sharp increase but is able to recover quickly due to the increased parameter variation available to the EWRLS algorithm, gradually levelling to 0.15 N. Finally, $\lambda = 0.995$ suffers more from the decreased parameter variation, and ends with a prediction RMSE of 0.185 N, although it is still trending downwards.

The estimated parameters for the static forgetting factors are presented in Figure 6.21. The introduction of the simulated tissue at 24 s causes significant change in parameters, similar to what was observed in Figure 6.14. It should be noted that palpation begins at different times for each forgetting factor – a consequence of human teleoperation. Instead, attention should be drawn to the individual rate of change once palpation begins, indicated by the sudden change in estimated parameter just after the simulated tissue is introduced. Once palpation begins, all parameters begin to converge to more steady values. The rate at which parameters change from their respective maximum or minimum

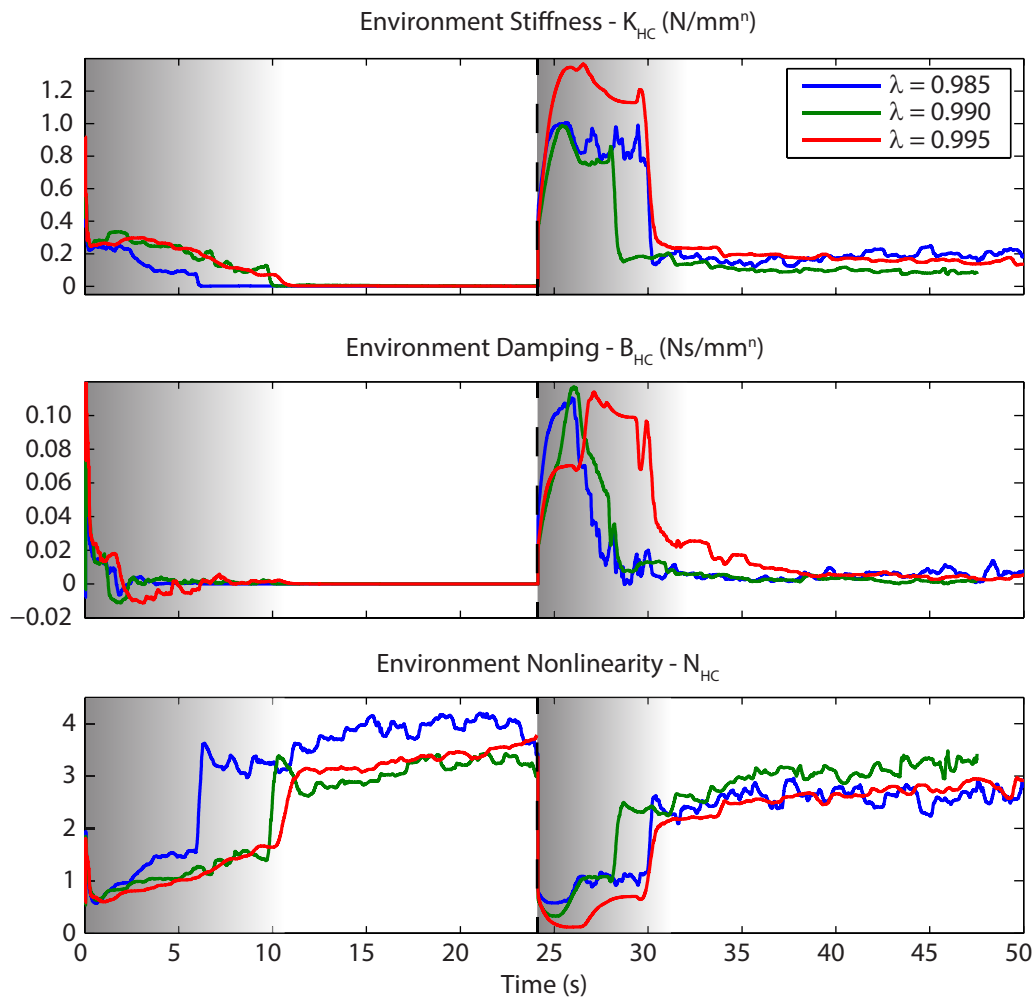


Figure 6.21: Estimated parameters for a polyurethane foam (0 – 24 s) and simulated tissue sample (24 – 50 s), using a static forgetting factor.

is similar between $\lambda = 0.985$ and $\lambda = 0.990$. $\lambda = 0.995$ has a slightly slower rate of change, particularly noticeable for the damping coefficient.

Parameter Stability

Up to now, the difference in estimation and prediction errors between the adaptive and static forgetting factor methodologies have been minor. The eventual estimation and prediction RMS errors for both environments are summarised in Table 6.3. As can be seen, the lowest estimation error is observed with a static forgetting factor of $\lambda = 0.985$. This is due to a number of reasons, but primarily stems from $\lambda = 0.985$ having the fastest estimation time.

Table 6.3: Summary of the final estimation and prediction RMS errors for both the static and adaptive forgetting factor methodologies.

Material	Adaptive λ (e_{max})			Static λ		
	0.1	0.2	0.3	0.985	0.990	0.995
<i>Estimation RMSE (N)</i>						
Polyurethane Foam	0.043	0.068	0.083	0.026	0.026	0.045
Transition (Peak)	0.230	0.200	0.310	0.200	0.300	0.500
Simulated Tissue	0.055	0.072	0.095	0.040	0.065	0.110
<i>Prediction RMSE (N)</i>						
Polyurethane Foam	0.117	0.131	0.158	0.135	0.100	0.115
Transition (Peak)	0.300	0.320	0.420	0.580	0.380	0.700
Simulated Tissue	0.135	0.145	0.182	0.150	0.135	0.185

However, using a static forgetting factor essentially locks the estimator speed into an uncompromising state. For $\lambda = 0.985$, this results in very quick parameter convergence, but by extension also accentuates dynamic environment properties such as hysteresis and restitution. Here, the faster, static, estimator will attempt to capture these effects with each insertion or retraction of the surgical tool, which can potentially improve *estimator* performance.

The caveat is that the haptic master, and operator, perceive a warped image of this hysteresis. As has been mentioned, the slave and master kinematics are rarely aligned during contact with a soft environment. Hysteresis incorporated by the estimated parameters is only valid from the reference point of the *slave kinematics*. Extending this hysteresis immediately to the *master kinematics* results in the hysteresis being distorted.

To illustrate this point, the final 10 s of the estimated parameters for each experiment is presented in Figure 6.22

As can be seen, there is considerably more variation in parameters when using a static forgetting factor compared to the developed forgetting factor adaptor. This variation is the estimator attempting to account for fast-acting hysteresis and material restitution. When these varying parameters are used by the virtual environment, the hysteresis is distorted, as the upwards and downward motions of the master often do not correspond immediately to the upward/down motions of the slave. As such, this variation is

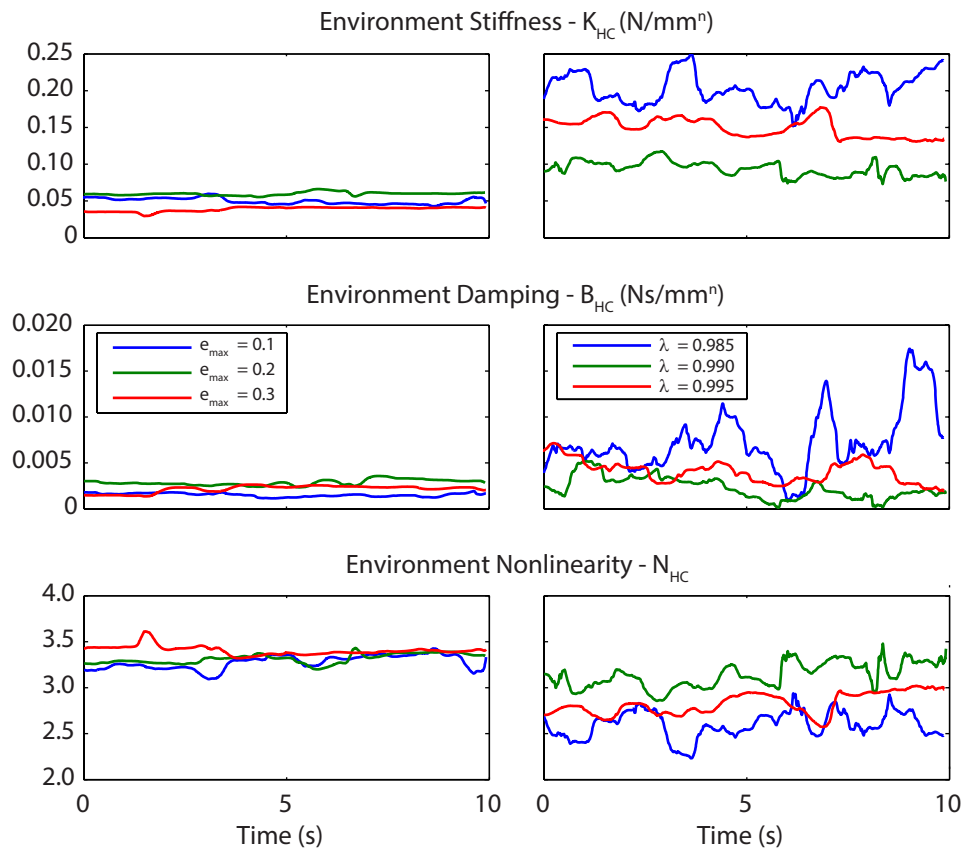


Figure 6.22: Final 10s of each estimated parameter for the adaptive forgetting factors (left), and the static forgetting factors (right).

undesirable as it can create regions of non-homogeneity and inconsistency within the force feedback profile.

Taking both estimation and prediction error, as well as parameter stability, into consideration suggests that an adaptive forgetting factor offers potential improved performance over a static forgetting factor. By using an adaptor based on estimation error, the EWRLS algorithm is able to increase estimation speed during times of high uncertainty, but similarly slow down estimation speed once the estimation error has fallen below an acceptable threshold. This enables quick convergence of parameters, while also ensuring that parameters remain steady once acceptable values have been reached. However, further experiments with a wider variety of environments are required before more concrete conclusions can be drawn.

Ultimately, the goal of any bilateral controller aimed at teleoperated surgical robotics is to provide the surgeon with a faithful representation of the remote environment -

specifically biological tissues. The challenge presented by this task cannot be understated, as the environment may be inconsistent, non-linear, and dynamic. While preliminary, the results presented in this chapter demonstrate that using an environment estimation – force prediction methodology shows promise in satisfying the ultimate goal of this research. Faithful representation of the given environments is evident by the low prediction error observed between measured slave and force feedback profiles. The use of an adaptive estimation speed furthers this goal by minimising the fast-acting hysteresis and restitution effects of the material. Qualitatively, using the adaptive forgetting factor felt more natural and realistic during teleoperation, and a greater sense of connectedness with the remote environment was perceived.

6.3 Summary

In this chapter, an adaptive forgetting factor methodology was proposed to enable fast initial parameter estimation, yielding to slower estimation once the parameters are have been well established. Parameter estimation for both the Kelvin-Voight and Hunt-Crossley force models was first investigated over a number of static forgetting factors, with the slave motion controlled via a sinusoidal trajectory. From this, an acceptable range of forgetting factors was proposed as $0.985 \leq \lambda \leq 1$, where $\lambda = 0.985$ represents fast estimation, and $\lambda = 1$ represents slow estimation. Additionally, at this point the Kelvin-Voight force model was dismissed as a non-viable force model for non-linear environments.

An arctangent function, with estimation error as the independent variable, was then proposed as the underlying form of an adaptive forgetting factor. The arctangent function features a smooth transition between upper and lower λ values, which enables an easily defined transition point (e_{mid}), or threshold error. Additionally, a steepness factor can be used to separate the upper and lower λ values more sharply. The estimation error, used to calculate the resultant forgetting factor, was included along with the arctangent function into the control structure of the teleoperation system.

The performance of the adaptive forgetting factor was investigated via experimentation with an initial polyurethane foam environment, which was replaced with a simulated tissue sample mid-way through each experiment. Three threshold errors were investigated, via the e_{max} value, along with three static forgetting factors, representing slower, medium, and faster estimation. Performance of each experiment was determined through the estimation error, prediction error, and parameter convergence and stability. While the fast static forgetting factor ($\lambda = 0.985$) exhibited the lowest *estimation* errors, further analysis demonstrated that parameter stability suffered from the increased variability in parameters.

An adaptive forgetting factor, with $e_{max} = 0.1$ N, was suggested as the best overall teleoperator performance, as it was able to quickly converge the estimated parameters to acceptable values, while minimising parameter variation once these values have been reached.

Chapter 7

Conclusions and Recommendations

7.1 Summary

In this research an environment estimation - force prediction methodology was developed for a haptic-enabled robotic minimally invasive surgical system. The research topics, relevant theory, and literature review was introduced in Chapter 1 and Chapter 2. The utilised teleoperated robotic surgical system was outlined in Chapter 3, highlighting its design features and performance characteristics. In Chapter 4 the proposed estimation - prediction controller was developed, whereby an estimate of the contact environment is used to predict the force feedback response. Experimental validation for the estimator was also conducted in Chapter 4, and for the full teleoperated system in Chapter 5. Further improvements to the controller were made in Chapter 6, where a forgetting factor adaptor was developed and experimentally verified.

7.1.1 Developed Estimation - Prediction Controller

The developed estimation - prediction controller compensates for the intrinsic time-delay between the slave and the master subsystems by replacing the force feedback channel with a virtual estimate of the environment. The estimator – an exponentially weighted recursive least squares (EWRLS) algorithm – provides recursive estimations

for selected environment parameters via the slave position, velocity, and force information. The environment parameters, representing qualities such as stiffness, damping, and environment non-linearity, are subsequently used by the controller to simulate a virtual environment for the master to interact with. The force models chosen for experimentation were the Kelvin-Voight and Hunt-Crossley force models.

The EWRLS estimator was initially tested for robustness by investigating parameter convergence with the slave in contact with a polyurethane foam, following a generated sinusoidal trajectory input. Palpation experiments revealed that the estimator was particularly sensitive to the relative phase of each of the input signals. Inconsistently delaying the input position, velocity, or force via a low-pass filter resulted in incompatible parameter estimation values, such as a highly unstable negative damping coefficient. As such, the estimator inputs were required to be filtered with an all or nothing approach, regardless of the relative noise in each signal, to ensure the filter induced delay is consistent across each input.

Human-in-the-loop palpation experiments with a polyurethane foam demonstrated that the Hunt-Crossley force model provided improved teleoperation transparency when compared to direct feedback, spring-based adaptor, and Kelvin-Voight force model approaches. The non-linear characteristics of the polyurethane foam were well modelled by the non-linear Hunt-Crossley model. Prediction error for the palpation experiments was consistently lower with the Hunt-Crossley model, and demonstrated significant improvements in teleoperation transparency.

7.1.2 Forgetting Factor Adaptor

Further improvements on the estimation - prediction methodology were made in the context of the estimator's adaptability. A consistent and homogeneous environment is unlikely to occur in a surgical setting, and as such it is required that the estimator quickly and accurately adjust the environment parameters accordingly when a new environment is encountered.

Intrinsic to the EWRLS estimator is the forgetting factor, which assigns the relative weight newer measurements have over older measurements, and in effect dictates the speed of estimation. An adaptor was included into the estimator which varied the forgetting factor based on the accuracy of the estimated parameters. Faster estimation was specified when estimation error was high, and slower estimation for when error was low.

The adaptor was derived from the arctangent function, which related the forgetting factor to the estimation error. Experimental analysis showed that the adaptor was able to quickly adjust the estimated parameters when the slave transitioned from a polyurethane foam to simulated tissue environment. Further, the adaptor demonstrated improved stability of parameters once an acceptable level of accuracy in parameters was reached.

7.2 Recommendations for Future Work

The environment estimation - force prediction bilateral controller achieved desired improvements to teleoperator transparency, and demonstrated promising results as a force feedback methodology. Recommendations for future research and improvements are presented here, and concentrate on two key areas:

- Design improvements to the Surgical Slave Mechanism
- Additional avenues of research, with an emphasis on improvements to the estimation - prediction controller.

7.2.1 Experimental Platform

Improvements to the Surgical Slave Mechanism

- The slave mechanism's lowest resonant frequency is currently 14 Hz along about x-axis. Such a low resonant frequency restricts the motion bandwidth to approximately 1 Hz, as the lowest resonant frequency should be roughly 10 times the motion bandwidth to reduce mechanical vibrations [82]. Increasing the resonant frequency will allow for a higher bandwidth, and an increase in system position

and velocity gains, resulting in tighter position tracking. It is recommended that the lowest resonant frequency be increased to approximately 20 Hz, and bandwidth subsequently increased to approximately 2 Hz.

- Additionally, by increasing the mechanism's stiffness and motion bandwidth, a faster motor control loop speed of 1 kHz can be realised by replacing the CAN-bus EPOS2 motor controllers with EtherCAT networked controllers.
- It is recommended that the linear stage of the slave mechanism be redesigned to add compliance to the z-axis. Adding compliance would bound the maximum expected environment stiffness, and increase stability when in contact with stiff environments [80].
- The force/torque sensor located at the distal-tip of the end-effector currently uses an accelerometer to compensate for gravitational forces during operation. Inertial forces, however, are still present. An inertial measurement unit (IMU), utilising gyroscopic measurements, is recommended to complement the accelerometer to provide inertial force compensation.
- Finally, the current slave end-effector is a flat surface with no additional degrees of freedom or actuation. Surgical procedures require additional degrees of freedom and manipulators at the surgical tool to facilitate complex tasks. An actuated end-effector, such as the multi-DoF EndoWrist[®] instruments in Figure 7.1 utilised by Intuitive Surgery's da Vinci surgical system [83], would provide the additional manipulation capabilities required in surgical procedures.



Figure 7.1: Intuitive Surgical's *EndoWrist*[®] instruments [83].

7.2.2 Future Research

Controller Design

- The developed estimation - prediction controller uses an entirely virtual environment to derive the master feedback force. The virtual environment is fully dependant on the accuracy and stability of the estimated parameters. Poorly estimated parameters, such as during initial contact or when persistency of excitation is low, translates directly to a poorly realised virtual environment, and compromised tele-operator transparency. Introducing a sliding scale between direct and virtual feedback during such times would enable more consistent and robust force feedback. A time-based transition from measured to virtual environments, or a more robust method utilising a metric for persistency of excitation, is recommended.
- Alternatively, a self-perturbing mechanism can be incorporated which increases persistency of excitation when necessary. However, this involves developing a metric for persistency of excitation. Further, due to the nature of a self-perturbing excitation mechanism, such a system may induce unwanted or unexpected slave movements which are undesirable during a surgical procedure. Applications which are not as strict with slave-environment interactions may possibly utilise such a mechanism.
- For this research, it has been assumed that the estimated parameters are stable and passive, provided they are a good representation of the environment, and that the environment itself is stable. However, a robust stability analysis of the estimated parameters is required before stability can be assured, and this technique can be applied to surgical robotics. It is recommended that a stability analysis be conducted before any further developments are made to the estimation - prediction controller.

- The contact environments used during this research was limited to palpation of soft-body materials. Further investigation with a wider variety of materials, exhibiting a range of properties, is recommended for future research. Experiments involving lesion location and identification, as well as multi-layered environments, are similarly suggested as future avenues of experimental verification.

Estimator

- The first order low-pass Butterworth filter is currently used to smooth the system position, velocity, and force variables. This filter induces a frequency-dependant delay into the smoothed signal. The EWRLS estimator was shown to be sensitive to the phase coherence of the input signals. A finite impulse response (FIR) filter has no such frequency-dependant delay, and it is expected that the estimator is not as sensitive to this category of filters. It is recommended that the Butterworth filter be replaced by an FIR filter to allow for a greater level of signal filtering. However, any such filter will need to be examined for any unintended consequences, as FIR filters do not have a flat pass-band or steep roll-off.
- The developed adaptive forgetting factor relies on the appropriate choice in e_{range} and λ_{range} to produce favourable results. An alternative avenue of adapting λ is to calculate the optimal value for λ by using a type-II maximum likelihood estimation process [84], and is recommended for investigation in future research.
- The EWRLS estimator uses to some extent or another all prior measurements to calculate the estimated parameters are each time-step. This is counter-productive if the slave comes into contact with a wide variety of environments, as previous environments may still influence the estimation of the current environment. Proposed sliding-window estimators, specifically the variable length sliding rectangular window blockwise least squares (VLSRWBLS) estimator has shown promise in [85] as a fast and stable parameter estimation technique. It is recommended that a wider variety of estimators, including the VLSRWBLS is investigated in future research.

Bibliography

- [1] Robert Arnott et al. *Trepanation*. CRC Press, 2003.
- [2] Daniel C Snell. *A Companion to the Ancient Near East*. John Wiley & Sons, 2008.
- [3] William Osler. *Evolution of modern medicine*. DevCom, 1921.
- [4] Andreas Vesalius. *De humani corporis fabrica*. 4. Norman Publishing, 1998.
- [5] Wendy Moore. *The Knife Man: The Extraordinary Life and Times of John Hunter, Father of Modern Surgery*. Random House, 2010.
- [6] Stavros A Antoniou et al. “Past, present, and future of minimally invasive Abdominal surgery”. In: *JSLs: Journal of the Society of Laparoendoscopic Surgeons* 19.3 (2015).
- [7] Wolfgang Schwenk et al. “Short term benefits for laparoscopic colorectal resection”. In: *The Cochrane Library* (2005).
- [8] Colon Cancer Laparoscopic or Open Resection Study Group et al. “Laparoscopic surgery versus open surgery for colon cancer: short-term outcomes of a randomised trial”. In: *The lancet oncology* 6.7 (2005), pp. 477–484.
- [9] Jens Rassweiler et al. “Laparoscopic versus open radical prostatectomy: a comparative study at a single institution”. In: *The Journal of urology* 169.5 (2003), pp. 1689–1693.
- [10] Hua-yin Yu et al. “Use, costs and comparative effectiveness of robotic assisted, laparoscopic and open urological surgery”. In: *The Journal of urology* 187.4 (2012), pp. 1392–1399.

- [11] Paula Gomes. “Surgical robotics: Reviewing the past, analysing the present, imagining the future”. In: *Robotics and Computer-Integrated Manufacturing* 27.2 (2011), pp. 261–266.
- [12] Robert D Howe and Yoky Matsuoka. “Robotics for surgery”. In: *Annual Review of Biomedical Engineering* 1.1 (1999), pp. 211–240.
- [13] Anthony R Lanfranco et al. “Robotic surgery: a current perspective”. In: *Annals of surgery* 239.1 (2004), pp. 14–21.
- [14] Alexei Wedmid, Elton Llukani, and David I Lee. “Future perspectives in robotic surgery”. In: *BJU international* 108.6b (2011), pp. 1028–1036.
- [15] Prokar Dasgupta and Roger S Kirby. “The current status of robot-assisted radical prostatectomy”. In: *Asian J Androl* 11.1 (2009), pp. 90–93.
- [16] *da-Vinci Robotic Surgical System*. <http://www.urolassoc.com/images/pic-davinci-robotic.jpg>. Accessed: 20/10/2016.
- [17] *Intuitive Surgical Frequently Asked Questions*. <https://www.intuitivesurgical.com/company/faqs.html>. Accessed: 7th July, 2018.
- [18] Chang Moo Kang et al. “Conventional laparoscopic and robot-assisted spleen-preserving pancreatectomy: does da Vinci have clinical advantages?” In: *Surgical endoscopy* 25.6 (2011), pp. 2004–2009.
- [19] Rebecca Voelker. “Eye Tracking in Surgical Robotics”. In: *Jama* 318.19 (2017), pp. 1858–1858.
- [20] Antonino Spinelli et al. “First experience in colorectal surgery with a new robotic platform with haptic feedback”. In: *Colorectal Disease* 20.3 (2018), pp. 228–235.
- [21] Pradeep P Rao. “Robotic surgery: new robots and finally some real competition!” In: *World journal of urology* 36.4 (2018), pp. 537–541.
- [22] Vincent De Sars, Sinan Haliyo, and Jerome Szewczyk. “A practical approach to the design and control of active endoscopes”. In: *Mechatronics* 20.2 (2010), pp. 251–264.

- [23] MC Montesi et al. “An SMA-based flexible active endoscope for minimal invasive surgery”. In: *Journal of micromechanics and microengineering* 5.2 (1995), p. 180.
- [24] Takeyoshi Ota et al. “A highly articulated robotic surgical system for minimally invasive surgery”. In: *The Annals of thoracic surgery* 87.4 (2009), pp. 1253–1256.
- [25] Seth M Brown et al. “Three-dimensional endoscopic sinus surgery: feasibility and technical aspects”. In: *Otolaryngology: Head and Neck Surgery* 138.3 (2008), pp. 400–402.
- [26] Pirmin Storz et al. “3D HD versus 2D HD: surgical task efficiency in standardised phantom tasks”. In: *Surgical endoscopy* 26.5 (2012), pp. 1454–1460.
- [27] Stefano Bordignon et al. “Endoscopic ablation systems”. In: *Expert review of medical devices* 10.2 (2013), pp. 177–183.
- [28] Brian T Bethea et al. “Application of haptic feedback to robotic surgery”. In: *Journal of Laparoendoscopic & Advanced Surgical Techniques* 14.3 (2004), pp. 191–195.
- [29] DM Herron and M Marohn. “A consensus document on robotic surgery”. In: *Surgical endoscopy* 22.2 (2008), pp. 313–325.
- [30] Allison M Okamura. “Haptic feedback in robot-assisted minimally invasive surgery”. In: *Current opinion in urology* 19.1 (2009), p. 102.
- [31] Allison M Okamura. “Methods for haptic feedback in teleoperated robot-assisted surgery”. In: *Industrial Robot: An International Journal* 31.6 (2004), pp. 499–508.
- [32] Carol E Reiley et al. “Effects of visual force feedback on robot-assisted surgical task performance”. In: *The Journal of thoracic and cardiovascular surgery* 135.1 (2008), pp. 196–202.
- [33] Dale A Lawrence. “Stability and transparency in bilateral teleoperation”. In: *IEEE transactions on robotics and automation* 9.5 (1993), pp. 624–637.

- [34] Lucian Panait et al. "The role of haptic feedback in laparoscopic simulation training". In: *Journal of Surgical Research* 156.2 (2009), pp. 312–316.
- [35] OAJ Van der Meijden and MP Schijven. "The value of haptic feedback in conventional and robot-assisted minimal invasive surgery and virtual reality training: a current review". In: *Surgical endoscopy* 23.6 (2009), pp. 1180–1190.
- [36] Jake J Abbott, Panadda Marayong, and Allison M Okamura. "Haptic virtual fixtures for robot-assisted manipulation". In: *Robotics research*. Springer, 2007, pp. 49–64.
- [37] Amir Haddadi and Keyvan Hashtrudi-Zaad. "A new method for online parameter estimation of hunt-crossley environment dynamic models". In: *Intelligent Robots and Systems, 2008. IROS 2008. IEEE/RSJ International Conference on*. IEEE, 2008, pp. 981–986.
- [38] Amir Haddadi and Keyvan Hashtrudi-Zaad. "Real-time identification of Hunt–Crossley dynamic models of contact environments". In: *IEEE transactions on robotics* 28.3 (2012), pp. 555–566.
- [39] Robert J Anderson and Mark W Spong. "Bilateral control of teleoperators with time delay". In: *IEEE Transactions on Automatic control* 34.5 (1989), pp. 494–501.
- [40] Neville Hogan. "Controlling impedance at the man/machine interface". In: *Robotics and automation, 1989. Proceedings., 1989 IEEE international conference on*. IEEE, 1989, pp. 1626–1631.
- [41] FB Llewellyn. "Some fundamental properties of transmission systems". In: *Proceedings of the IRE* 40.3 (1952), pp. 271–283.
- [42] Richard J Adams and Blake Hannaford. "A two-port framework for the design of unconditionally stable haptic interfaces". In: *Intelligent Robots and Systems, 1998. Proceedings., 1998 IEEE/RSJ International Conference on*. Vol. 2. IEEE, 1998, pp. 1254–1259.

- [43] Richard J Adams and Blake Hannaford. “Stable haptic interaction with virtual environments”. In: *Robotics and Automation, IEEE Transactions on* 15.3 (1999), pp. 465–474.
- [44] Keyvan Hashtrudi-Zaad and Septimiu E Salcudean. “Analysis of control architectures for teleoperation systems with impedance/admittance master and slave manipulators”. In: *The International Journal of Robotics Research* 20.6 (2001), pp. 419–445.
- [45] J Edward Colgate. “Robust impedance shaping telemanipulation”. In: *Robotics and Automation, IEEE Transactions on* 9.4 (1993), pp. 374–384.
- [46] John Doyle. “Analysis of feedback systems with structured uncertainties”. In: *IEE Proceedings D-Control Theory and Applications*. Vol. 129. 6. IET. 1982, pp. 242–250.
- [47] Yasuyoshi Yokokohji, Norio Hosotani, and Tsuneo Yoshikawa. “Analysis of maneuverability and stability of micro-teleoperation systems”. In: *Robotics and Automation, 1994. Proceedings., 1994 IEEE International Conference on*. IEEE. 1994, pp. 237–243.
- [48] Emmanuel B Vander Poorten, Yasuyoshi Yokokohji, and Tsuneo Yoshikawa. “Stability analysis and robust control for fixed-scale teleoperation”. In: *Advanced Robotics* 20.6 (2006), pp. 681–706.
- [49] K Hashtrudi-Zaad and SE Salcudean. “On the use of local force feedback for transparent teleoperation”. In: *Robotics and Automation, 1999. Proceedings. 1999 IEEE International Conference on*. Vol. 3. IEEE. 1999, pp. 1863–1869.
- [50] Keyvan Hashtrudi-Zaad and Septimiu E Salcudean. “Transparency in time-delayed systems and the effect of local force feedback for transparent teleoperation”. In: *IEEE Transactions on Robotics and Automation* 18.1 (2002), pp. 108–114.
- [51] Peter F Hokayem and Mark W Spong. “Bilateral teleoperation: An historical survey”. In: *Automatica* 42.12 (2006), pp. 2035–2057.

- [52] Kevin B Fite, John E Speich, and Michael Goldfarb. “Transparency and stability robustness in two-channel bilateral telemanipulation”. In: *Journal of Dynamic Systems, Measurement, and Control* 123.3 (2001), pp. 400–407.
- [53] Richard Moreau et al. “Sliding-mode bilateral teleoperation control design for master–slave pneumatic servo systems”. In: *Control Engineering Practice* 20.6 (2012), pp. 584–597.
- [54] Aleš Hace and Marko Franc. “FPGA implementation of sliding-mode-control algorithm for scaled bilateral teleoperation”. In: *IEEE Transactions on Industrial Informatics* 9.3 (2013), pp. 1291–1300.
- [55] Bert Willaert et al. “Bilateral teleoperation: quantifying the requirements for and restrictions of ideal transparency”. In: *IEEE transactions on control systems technology* 22.1 (2014), pp. 387–395.
- [56] Jonghyun Kim, Pyung Hun Chang, and Hyung-Soon Park. “Two-channel transparency-optimized control architectures in bilateral teleoperation with time delay”. In: *IEEE Transactions on Control Systems Technology* 21.1 (2013), pp. 40–51.
- [57] Jee-Hwan Ryu, Dong-Soo Kwon, and Blake Hannaford. “Stable teleoperation with time-domain passivity control”. In: *IEEE Transactions on robotics and automation* 20.2 (2004), pp. 365–373.
- [58] Günter Niemeyer and J-JE Slotine. “Stable adaptive teleoperation”. In: *IEEE Journal of oceanic engineering* 16.1 (1991), pp. 152–162.
- [59] A Aziminejad et al. “Stability and performance in delayed bilateral teleoperation: Theory and experiments”. In: *Control Engineering Practice* 16.11 (2008), pp. 1329–1343.
- [60] Min Zheng et al. “Bilateral teleoperation with reducing wave-based reflections”. In: *Advances in Manufacturing* 1.3 (2013), pp. 288–292.
- [61] Günter Niemeyer and Jean-Jacques E Slotine. “Telemanipulation with time delays”. In: *The International Journal of Robotics Research* 23.9 (2004), pp. 873–890.

- [62] Emmanuel Nuno, Luis Basanez, and Romeo Ortega. "Passive bilateral teleoperation framework for assisted robotic tasks". In: *Proceedings 2007 IEEE International Conference on Robotics and Automation*. IEEE. 2007, pp. 1645–1650.
- [63] Nikhil Chopra et al. "On tracking performance in bilateral teleoperation". In: *IEEE Transactions on Robotics* 22.4 (2006), pp. 861–866.
- [64] Neal A Tanner and Günter Niemeyer. "Improving perception in time-delayed telerobotics". In: *The International Journal of Robotics Research* 24.8 (2005), pp. 631–644.
- [65] Carolina Passenberg, Angelika Peer, and Martin Buss. "A survey of environment-, operator-, and task-adapted controllers for teleoperation systems". In: *Mechatronics* 20.7 (2010), pp. 787–801.
- [66] K Hashtrudi-Zaad and Septimiu E Salcudean. "Adaptive transparent impedance reflecting teleoperation". In: *Robotics and Automation, 1996. Proceedings., 1996 IEEE International Conference on*. Vol. 2. IEEE. 1996, pp. 1369–1374.
- [67] Hyung-Kyi Lee, Myoung Ho Shin, and Myung Jin Chung. "Adaptive controller of master-slave systems for transparent teleoperation". In: *Advanced Robotics, 1997. ICAR'97. Proceedings., 8th International Conference on*. IEEE. 1997, pp. 1021–1026.
- [68] Lonnie J Love and Wayne J Book. "Force reflecting teleoperation with adaptive impedance control". In: *IEEE Transactions on Systems, Man, and Cybernetics, Part B (Cybernetics)* 34.1 (2004), pp. 159–165.
- [69] Jean-Jacques E Slotine and Weiping Li. "On the adaptive control of robot manipulators". In: *The international journal of robotics research* 6.3 (1987), pp. 49–59.
- [70] Hichem Arioui, Said Mammar, and Tarek Hamel. "A Smith-prediction based Haptic Feedback Controller for Time Delayed Virtual Environments Systems". In: *American Control Conference*. 2002, pp. 4303–4309.

- [71] KB Fite, M Goldfarb, and A Rubio. “Transparent telemanipulation in the presence of time delay”. In: *Advanced Intelligent Mechatronics, 2003. AIM 2003. Proceedings. 2003 IEEE/ASME International Conference on*. Vol. 1. IEEE. 2003, pp. 254–259.
- [72] Andrew C Smith and Keyvan Hashtrudi-Zaad. “Smith predictor type control architectures for time delayed teleoperation”. In: *The International Journal of Robotics Research* 25.8 (2006), pp. 797–818.
- [73] Andrew C Smith and K Van Hashtrudi-Zaad. “Neural network-based teleoperation using Smith predictors”. In: *IEEE International Conference Mechatronics and Automation, 2005*. Vol. 3. IEEE. 2005, pp. 1654–1659.
- [74] Andrew C Smith and Keyvan Hashtrudi-Zaad. “Adaptive teleoperation using neural network-based predictive control”. In: *Proceedings of 2005 IEEE Conference on Control Applications, 2005. CCA 2005*. IEEE. 2005, pp. 1269–1274.
- [75] Jin-Quan Huang and Frank L Lewis. “Neural-network predictive control for non-linear dynamic systems with time-delay”. In: *IEEE Transactions on Neural Networks* 14.2 (2003), pp. 377–389.
- [76] Yuan-cheng Fung. *Biomechanics: mechanical properties of living tissues*. Springer Science & Business Media, 2013.
- [77] Nicola Diolaiti, Claudio Melchiorri, and Stefano Stramigioli. “Contact impedance estimation for robotic systems”. In: *IEEE Transactions on Robotics* 21.5 (2005), pp. 925–935.
- [78] Mohsen Mahvash and Vincent Hayward. “Haptic rendering of cutting: A fracture mechanics approach”. In: (2001).
- [79] KH Hunt and FRE Crossley. “Coefficient of restitution interpreted as damping in vibroimpact”. In: *Journal of applied mechanics* 42.2 (1975), pp. 440–445.

- [80] Willem Heinrich Schwalb. “Design and analysis of an experimental force-feedback enabled surgical robot for minimally invasive surgery”. PhD thesis. Monash University. Faculty of Engineering. Department of Mechanical and Aerospace Engineering, 2016.
- [81] Abacus-ALS. *Complex Tissue Model TSC-10*. <https://http://www.abacus-als.com/product/complex-tissue-model-tsc-10-2/>. Accessed: 20/9/2017.
- [82] Stefan Brock and Dominik Łuczak. “Speed control in direct drive with non-stiff load”. In: *Industrial Electronics (ISIE), 2011 IEEE International Symposium on*. IEEE. 2011, pp. 1937–1942.
- [83] Intuitive Surgical. *EndoWrist Instruments*. <https://www.intuitivesurgical.com/products/instruments/>. Accessed: 20/9/2017.
- [84] Steven Van Vaerenbergh, Ignacio Santamara, and Miguel Lzaro-Gredilla. “Estimation of the forgetting factor in kernel recursive least squares”. In: *Machine Learning for Signal Processing (MLSP), 2012 IEEE International Workshop on*. IEEE. 2012, pp. 1–6.
- [85] Jin Jiang and Youmin Zhang. “A revisit to block and recursive least squares for parameter estimation”. In: *Computers & Electrical Engineering* 30.5 (2004), pp. 403–416.